Ultrafast Processes in High-Temperature Superconductors

Pierre Gay

Lincoln College, Oxford

Thesis submitted for the Degree of Doctor of Philosophy

Department of Physics
University of Oxford

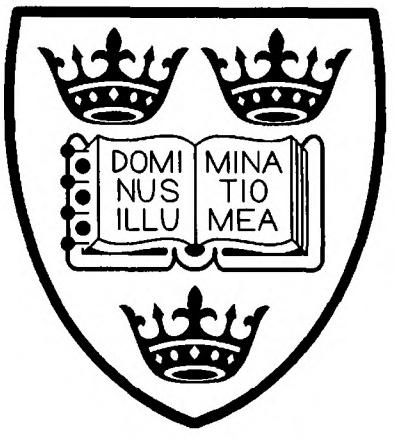

Michaelmas 2000

Ultrafast Processes in High-Temperature Superconductors

Pierre Gay,
Lincoln College, Oxford

Thesis submitted for the Degree of Doctor of Philosophy
Trinity Term 2000

Abstract

Using time-resolved photo-induced reflectivity, we reported for the first time a systematic work on the ultrafast response of $Bi_2Sr_2CaCu_2O_{8+\delta}$ (BSCCO-2212) and $Tl_2Ba_2CuO_{6+\delta}$ (TBCO-2201), measurements of detwinned $YBa_2Cu_3O_{7-\delta}$ (YBCO-123) single crystal with the electric field $\underline{E}$ parallel to the a and b-axis and high-resolution measurements of the rising edge dynamics of YBCO-123 thin films.

We identified similar photo-induced responses for BSCCO, TBCO and for YBCO with $\underline{E} \perp \underline{b}$, which indicates that we observed a universal response of HTSC coming from the CuO_2 superconducting planes. This latter dynamics is composed of three different components corresponding to the superconducting, pseudogap and normal state. A bi-molecular model has been put forward to explain the linear temperature dependence of the decay rate; the model implies that the re-formation of the condensate is limited by the rate at which quasiparticle interact. Moreover, we observed superconducting fluctuations up to 13K above T_c and a divergence of the long-lived component magnitude at very low temperature, which is explained by a cw heating model.

In the pseudogap state, we have several indications that the negative peak observed between T_c and T^* has a different origin from that of the superconducting signal below T_c. We argued that the probe mechanism of the pseudogap signal is electronic excitations of the pseudogap correlations. In the normal state, the observed dynamics is similar to that of simple metals.

In the second part of this thesis, the rising edge dynamics of YBCO has been resolved in time. The model developed to interpret the results implies that the hot quasiparticles relaxation time down to the Fermi energy is 55fs. In this context, we proved that the Mazin model cannot explain both the oscillatory and the non-oscillatory part of the dynamics in YBCO.

Finally, in YBCO-123, a new response has been observed with $\underline{E} \parallel \underline{b}$. We argued that the origin of this component is intraband transitions. This dynamics is solely responsive to the pseudogap, coming from the difference in scattering rate between pre-formed pairs and quasiparticles in the Drude reflectivity. The response with $\underline{E} \perp \underline{b}$ exhibits a strong a-b plane anisotropy in its long-lived component, which can be interpreted as a d-wave gap symmetry using the thermally-activated model.

List of Publications

- Smith D.C., Gay P., Stevens C.J., Wang D.Z., Wang J.H., Ren Z.F., Ryan J.F., *Ultrafast Optical Response of* $Tl_2Ba_2CuO_{6+\delta}$, J. of Low Temp. Phys. **117**, p. 1059 (1999).

- Gay P., Smith D.C., Stevens C.J., Chen C., Yang G., Abell S.J., Wang D.Z., Wang J.H., Ren Z.F., Ryan J.F., *Femtosecond Dynamics of BSCCO-2212,* J. of Low Temp. Phys. **117**, p. 1025 (1999).

- Stevens C.J., Gay P., Smith D.C., Chen C., Ryan J.F., *Anisotropy of the non-equilibrium quasiparticle dynamics in single crystals of* $YBa_2Cu_3O_{7-\delta}$, J. of Low Temp. Phys. **117**, p. 1031 (1999).

- Smith D.C., Gay P., Stevens C.J., Chen C., Yang G., Abell S.J., Wang D.Z., Wang J.H., Ren Z.F., Ryan J.F., *Femtosecond dynamics of BSCCO-2212 in both the weak and strong perturbation limits,* Accepted for Publication in Physica C.

- Smith D.C., Gay P., Wang D.Z., Wang J.H., Ren Z.F., Ryan J.F., *Ultrafast quasi-particle dynamics of* $Tl_2Ba_2CuO_{6+\delta}$, Accepted for publication in Physica C.

- Chen C., Smith D.C., Gay P., Wondre F., Ryan J.F., *Flux growth of superconducting* La_2CuO_4, Accepted for publication in Physica C.

- Gay P., Stevens C.J., Smith D.C., Chen C., Ryan J.F., *Anisotropy of the non-equilibrium quasiparticle dynamics in single-crystal* $YBa_2Cu_3O_{7-\delta}$, Accepted for publication in Physica C.

Acknowledgements

I would like to gratefully acknowledge the following people:

- Prof. J.F. Ryan for supervising this work and for suggesting interesting problems to work on.
- The SNSF for funding my research.
- Dr. C. Stevens and Dr. D. Smith for endless practical advice, encouragement and for teaching me so much physics over the last three years.
- Dr. R. Taylor and Dr. A. Maciel for helpful discussions in physics.
- Dr. J.W. Hodby and Dr. C. Chen for providing YBCO and BSCCO single crystals; Dr. J.S. Abell for BSCCO single crystals and Prof. Z.F. Ren for TBCO and BSCCO thin films.
- The technical support staff of the Clarendon Laboratory, especially R. Makin and G. Matthews.
- The ultrafast spectroscopy group for its enthusiasms and humour.

to Françoise and Carole

Contents

Chapter 1

Introduction

High-temperature superconductors (HTSC) have been extensively studied for both fundamental and applied purposes since their discovery by Bednorz and Müller [1] in 1986. Up to this date, the highest critical temperature achieved with low-temperature superconductors was 23K for Nb_3Ge, which has been increased above the boiling point of liquid nitrogen (77K) with the high-temperature superconductors up to the current record of 134K for $Hg_2Ba_2Ca_2Cu_3O_{10-\delta}$ at ambient pressure. Considerable effort has been put into the comprehension of the HTSC. However, fundamental issues such as the mechanism which binds the carriers into superconducting Cooper pairs, the nature of the superconducting ground state and how it leads to high transition temperatures still have to be resolved. HTSC are different in many ways from previously known superconductors, which suggests that a new theory has to be developed to explain their properties.

Experimentally, the understanding of HTSC can be pursued by either measuring properties of the ground state itself, such as experiments on the pair symmetry, or more commonly by investigating the excitations from the ground state, as explored in heat capacity, inelastic neutron scattering and optical conductivity experiments. The presence of a quasiparticle intraband optical response clearly indicates the possibility of single

particle excitations of the ground state. Excitations of the phase of the condensate are also expected to be important. Experimental evidence for the importance of phase excitations comes from comparison of pairing and coherence energies determined from single particle and Andreev tunnelling experiments [2].

The question of which excitations are responsible for driving the superconducting phase transition can be addressed by studies of critical fluctuations as observed in heat capacity and thermal experiments [3]. These experiments suggest a changeover in the relative importance of single particle and phase excitations with doping from the over- to the underdoped regime. A related question concerns the pseudogap, which is defined as a reduction in the density of states near the Fermi energy at temperatures above T_c [4]. The pseudogap is considered either as a precursor of superconductivity, as it would be expected if the phase transition is driven by phase excitations [2], or as an independent suppression of the density of states [5].

Ultrafast femtosecond studies of the cuprate superconductors offer the chance to directly probe the nature of the low-energy electronic excitations and their interactions with other fundamental excitations of the system. They allow the investigation of non-equilibrium excited states and the determination of scattering rates not accessible by time-integrated spectral measurements. Understanding the interaction of the electronic excitations with other fundamental excitations of the HTSC is a necessary step towards explaining the high-transition temperatures in these materials. Measurements of the ultrafast optical response, in which the time development of a non-equilibrium state is followed, allow these interactions to be probed in real time [6, 7].

Nearly all the experimental studies to date have focused on $YBa_2Cu_3O_{7-\delta}$ (YBCO-123) and its analogues. The ultrafast optical response of YBCO-123 has been interpreted as following the dynamics of the re-formation of Cooper pairs from non-equilibrium quasiparticles. One previous low-temperature study has been performed on $Bi_2Sr_2CaCu_2O_{8+\delta}$

(BSCCO-2212), but at an extremely high-excitation density [8]. One previous study has been performed on $Tl_2Ba_2Ca_2Cu_3O_{10}$ (TBCO-2223) [9] over a restricted temperature range higher than T_c - 20K and on a sample with a 20K wide superconducting transition.

Many properties of HTSC depend on the number of copper oxide (CuO_2) planes present in the unit cell and most HTSC do not contain copper oxide (CuO) chains as in YBCO-123. The important question of the generality of the observed ultrafast dynamics is therefore open, in particular for materials without CuO chains, and we will present here measurement of BSCCO-2212 with two CuO_2 planes and of TBCO-2201 with one CuO_2 plane.

1.1 Scope of this Thesis

We report in this thesis measurements of photo-induced reflectivity on a femtosecond timescale. We present the first systematic measurements of the ultrafast optical response of the chainless bi-layer cuprate BSCCO-2212 [10] and the chainless mono-layer cuprate $Tl_2Ba_2CuO_{6+\delta}$ (TBCO-2201) [11]. BSCCO-2212 is the best characterized compound of the Bi-layer materials, as it is easy to cleave and therefore it is the most often used HTSC for angle-resolved photoemission spectroscopy and tunneling experiments. TBCO-2201 is in many ways an ideal mono-layer cuprate due to its extremely low interplane coupling, as shown by c-axis optical conductivity and penetration depth measurements.

The dynamics observed in BSCCO-2212 and TBCO-2201 are remarkably similar and quite different from that observed in YBCO-123. The main new observations are: (i) a new component with a response due to the existence of the pseudogap, (ii) a linear temperature dependence of the decay rate corresponding to the re-condensation of the Cooper pairs, and (iii) evidence of superconducting correlations in TBCO-2201 for temperatures above T_c. From these observations we obtained new information about the

superconducting state symmetry, the nature of the pseudogap state and the universality of the ultrafast response in HTSC.

We report for the first time the time-resolved initial dynamics in YBCO-123, corresponding to the breaking of the Cooper pairs, with a time resolution $\leq$35fs, and present a model which explains the new dynamics. Finally, we present measurements of the ultrafast response of detwinned YBCO-123 single crystals, in which the responses along the a- and b-axis are separately identified [12]. A new signal is observed for the probe electric field parallel to the a-axis, which has been obscured in all previous thin film experiments and which exhibits close similarities with the BSCCO-2212 and TBCO-2201 response. We also measured the dependence of the induced reflectance on the electric field polarization in the a-b plane, which provides information about the symmetry of the order parameter.

1.2 Structure of the Thesis

The dissertation is organized as follows:

Chapter 2 contains a review of the current models used to interpret the measurements of the ultrafast carrier dynamics of HTSC. The chapter starts with a basic description of superconductivity and the successful BCS theory for low-temperature superconductors. The next section discusses some of the important aspects of the physics of cuprate superconductors, including the anisotropy, the pairing symmetry and the pairing interaction. We also introduce the structural, electronic and optical properties of YBCO-123, BSCCO-2212 and TBCO-2201 that are relevant to the experiments.

Chapter 3 provides an overview of the experimental techniques used in this study. This chapter includes a discussion of the three different time-resolved experiments. We briefly introduce mode-locked lasers, together with considerations on their characterization. There is a brief discussion of the cryostats and the thermometry used to perform experiments in the temperature range of 4 to 300K. Finally, the preparation and the characterization of the different types of samples are described.

Chapter 4 contains a review of previous ultrafast optical experiments on simple metals and on cuprate superconductors in order to introduce the theoretical interpretation of the results presented in the subsequent chapters. Almost all the previous ultrafast studies have focused on YBCO-123.

Chapter 5 presents the results of a series of pump-probe reflection experiments on single crystals and thin films of BSCCO-2212 and thin films of TBCO-2201. We present the detailed dynamics of the superconducting, pseudogap and normal states, measurements at high-excitation density, where the superconducting condensate is completely depleted, and evidence is obtained of superconducting correlation effects for temperatures above T_c. This chapter also contains brief sections on the dispersion of the induced reflectance and on measurements of the long-lived component (>12ns).

Chapter 6 presents time-resolved experiments on the early stage dynamics ($\leq$100fs) of YBCO-123 corresponding to the breaking of Cooper pairs, together with a model which accounts for this new observation. We report evidence of coherent phonon oscillations in YBCO-123 and a criticism of the Mazin model [13] concerning the origin of both the oscillatory and the non-oscillatory part of the dynamics.

Chapter 7 reports measurements of the ultrafast response of detwinned YBCO-123 single crystals. We have distinguished two different responses in the a-b plane, one with the probe electric field parallel to the a-axis, which is similar to that in BSCCO-2212 and TBCO-2201, and one with the electric field parallel to the b-axis, which is similar to the YBCO-123 thin film dynamics. The second part of this chapter concerns measurements of the superconducting state symmetry from a polarization dependence of the long-lived component (>12ns).

Chapter 8 summaries the new measurements of this thesis and their interpretations. We identified similar photo-induced responses for BSCCO, TBCO and for YBCO with $\underline{E} \perp \underline{b}$, which indicates that we observed a universal response of HTSC coming from the CuO_2 superconducting planes. This response is composed of three different components corresponding to the superconducting, pseudogap and normal state. We also present future experiments which would be interesting with respect to the interpretation of the ultrafast response of HTSC.

Chapter 2

High-Temperature Superconductors

Superconductors undergo a phase transition at a critical temperature T_c characterized by two fundamental properties: (i) the electrical resistivity becomes unmeasurably small, and (ii) the magnetic field inside the superconductor is expelled i.e. the superconductor becomes a perfect diamagnet except for a very thin skin layer (Meissner-Ochensfeld effect). This second effect occurs only when the magnetic field is less than a critical value. The critical temperature T_c of the superconductor depends on the nature of the material and the applied magnetic field.

In addition to the Maxwell equations, superconductors are described in a good approximation by the two relations:

$$\mathbf{E} = \frac{m}{nq^2}\frac{d\mathbf{J}}{dt} \tag{2.1}$$

$$\mathbf{J} = -\frac{nq^2}{m}\mathbf{A} \tag{2.2}$$

where n, q and m are the density, charge and mass of the superconducting charge carriers and **E**, **A**, **J** are the electric field, vector potential and current density vectors. Equation (2.1) describes a material with no resistivity and is derived from a Drude-like model of

free carriers by assuming that the superconducting carriers are not scattered. Equation (2.2) is necessary to lead to the Meissner effect.

2.1 BCS Theory

In 1957 Bardeen, Cooper and Schrieffer developed a microscopic theory, which is the basis for understanding the behaviour of low-temperature superconductors. They demonstrated that there is a phonon-mediated attraction between electrons: the energy of one electron is lowered by interacting with the distortion of the lattice produced by another electron. They showed that in a metal at $T \leq T_c$, pairs of electrons with opposite spin excited just above the Fermi energy can experience an effective attraction due to phonon exchange that is greater than the Coulomb repulsion; in this case they form a bound state with zero angular momentum i.e. an s-wave state. The pairs are called Cooper pairs and they constitute the superconducting charge carriers.

As the Cooper pairs are formed from two electrons, the pairs obey bosonic statistics. The bosonic nature of the Cooper pairs means that they can Bose condense into a singlet state: the superconducting condensate. If β^+ is the creation operator for a single Cooper pair and N the average number of pairs in the condensate, then the wavefunction of the condensate can be written in the form $\Psi = N^{1/2} \exp^{i\theta} \beta^+ \Psi_0$, where Ψ_0 is the ground state in the absence of superconductivity. The expression is identical to the quantum mechanical description of a coherent light wave in terms of photons. In the condensate, all the Cooper pairs are in identical states and have a fixed phase relationship with respect to each other. A simple picture which can explain the absence of electrical resistivity is the following. If a Cooper pair is scattered by a phonon for instance, it leaves the condensate, however another pair will form and join the condensate in order to maintain the equilibrium population of pairs. The new pair has to join with exactly the same momentum as all the other pairs in the condensate. The new momentum is the same

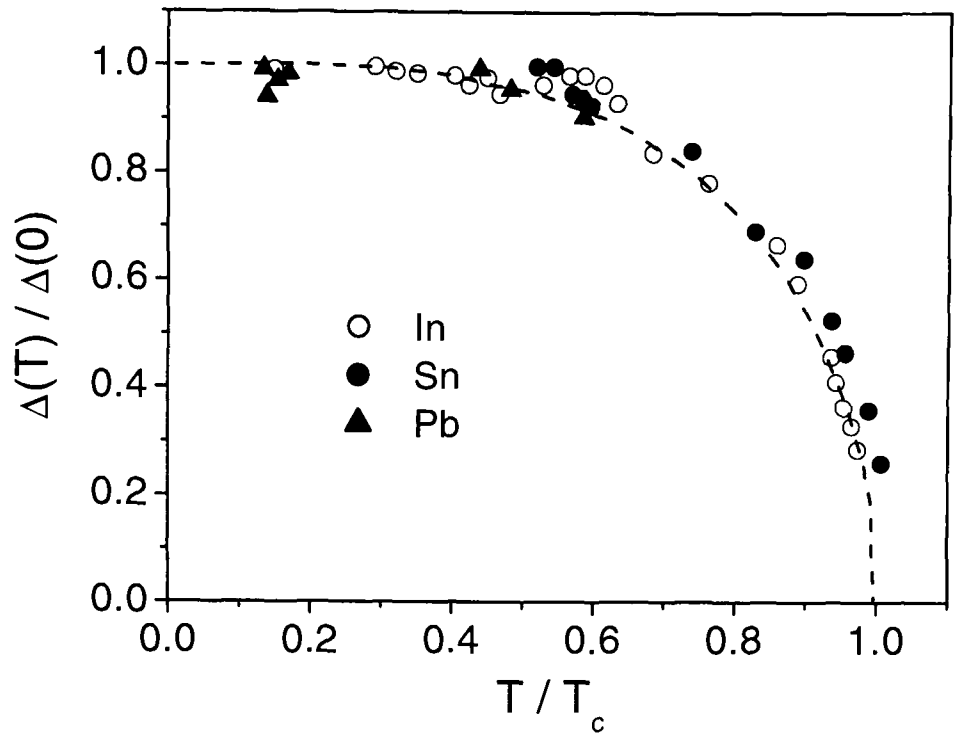

Figure 2.1: Temperature dependence of the superconducting gap energy Δ(T) from the weak-coupling BCS model, compared with tunneling experiments for Indium, Tin and Lead [14].

as the one lost by the condensate when the first pair was scattered out of it. Thus, unless almost all the condensate scatter at the same time, the total momentum of the condensate and the current associated with the condensate must remain constant.

The condensate wavefunction contains a phase θ which, in absence of a magnetic field, is constant over a distance called the coherence length ξ. This coherence length is related to the spatial extent of the Cooper pair wavefunction and, in pure metallic superconductors, is on the order of 1μm. In the presence of a slowly varying magnetic field given by the potential vector $\mathbf{A}$, θ follows the equation $\nabla\theta = q/\hbar\mathbf{A}$, where q is the charge of a Cooper pair. From this, the magnetic flux passing through a superconducting loop is quantized in units of h/q due to the need for θ to be single valued modulo 2π at any point in the ring. The fact that the magnetic flux through a small superconducting loop is quantized in units of h/2e is one of the main pieces of evidence supporting the theory that the superconducting charge carriers are indeed pairs of electrons.

So far, we have only discussed the BCS theory in terms of the superconducting condensate and at absolute zero temperature. If the temperature of the superconductor is above absolute zero, there is a finite probability that some Cooper pairs will gain enough energy to be thermally-dissociated into unpaired electrons. These thermal excitations are called quasiparticles and their density of states is often discussed in terms of the "semiconductor" model [15]. In this model, at low temperatures the population of quasiparticles can be approximated as being proportional to $exp^{-\Delta/k_BT}$ for T $< \frac{1}{2}T_c$. As the temperature increases, more pairs will dissociate and, as the superconducting pairing energy is proportional to the number of pairs, the energy barrier to thermal dissociation decreases with increasing temperature and eventually all the pairs will be dissociated at T_c. The temperature dependence of the superconducting gap energy can be calculated from the BCS model and is given in Fig 2.1.

2.2 High-Temperature Cuprate Superconductors

The BCS model and its extensions such as the Eliashberg [16] model were remarkably successful in explaining the properties of all known superconductors for many years. However, the properties of cuprate superconductors such as $YBa_2Cu_30_{7-\delta}$, which were discovered in the 1980s, cannot be explained in terms of the BCS theory.

In 1986 Müller and Bednorz [1] discovered superconductivity in $La_{2-x}Ba_xCuO_4$ which has a $T_c = 35K$, much higher than the previous maximum $T_c = 23K$ (Nb_3Ge). Within the next few years, a series of related compounds were discovered showing superconducting properties with T_c up to 132K. These superconductors with high critical temperatures are called high-temperature superconductors (HTSC). They are characterized by at least one plane of copper and oxygen atoms in their unit cell (CuO_2 planes) and are thus called the cuprate superconductors. The different compounds differ mainly by the number of CuO_2 planes and also by the other ions present in the unit cell.

The high critical temperatures of these compounds are very difficult to explain in terms of the BCS theory. In the BCS theory, the critical temperature is related to the strength of the attraction between the carriers in the Cooper pairs and the density of single particle states at the Fermi energy. The cuprates have a low density of states at the Fermi energy and hence a high critical temperature requires a strong phonon attraction between carriers. Such a strong carrier-phonon interaction should make large differences in the normal state properties of the materials and might be expected to make the compounds unstable to phase transitions. However, no evidence of such strong interactions has been observed and thus a new theory is required to explain superconductivity in these materials.

Since their discovery, a huge amount of research has been performed on these materials and many theories have been put forward, however, no theory is successful in explaining all HTSC properties yet. In this thesis, we will look at a few selected themes of general interest and then concentrate on the properties of HTSC relevant for understanding the experiments presented in the subsequent chapters.

Although the BCS theory has trouble explaining the high critical temperatures, the cuprate superconductors still have some properties in common with the BCS superconductors. Experiments on flux quantization show that the superconducting carriers have a charge of 2e indicating that the concept of Cooper pairs is still valid even if the BCS pairing mechanism is not. However, most of the cuprate superconductors, except $Nd_{2-y}Ce_yCuO_4$, are hole-conductors and therefore the paired carriers are in most cases holes rather than electrons as in the BCS theory. Tunneling and photoemission experiments also show a gap in the single particle density of states at the Fermi energy, although, as discussed later, there are differences in the nature of the gap between the cuprates and the low T_c superconductors. Tunneling experiments also show that phonons are involved in the pairing mechanism even if they do not provide the complete answer.

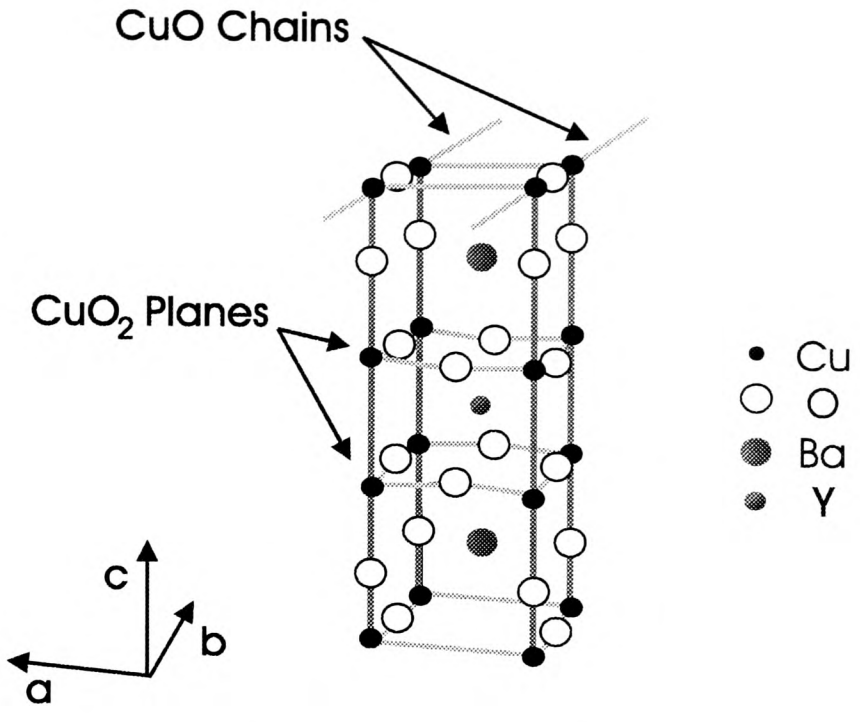

Figure 2.2: Unit cell of $YBa_2Cu_3O_7$. The diagram shows the two CuO_2 planes and the CuO chains. The structure is orthorhombic with the lattice parameters a = 3.86Å, b = 3.92Å and c = 11.84Å.

2.3 Crystal Structure of YBCO, BSCCO and TBCO

We present here the crystal structure of the HTSC studied in this thesis. $YBa_2Cu_3O_{7-\delta}$ (YBCO-123) shows two different crystallographic phases, orthorhombic and tetragonal. The crystal structure depends on the doping δ and the temperature. $YBa_2Cu_3O_{7-\delta}$ is orthorhombic for $0 \leq \delta \leq 0.6$ with a maximum T_c of 92K obtained for $\delta \cong 0.07$. The unit cell of $YBa_2Cu_3O_7$ is shown in Fig 2.2; it shows two CuO_2 planes, common to all cuprate superconductors, and CuO chains along the b-axis, which constitute the reservoir layers in YBCO. The lattice parameters are a = 3.86Å, b = 3.92Å and c = 11.84Å. The structure is modified for $\delta \geq 0$ by the removal of oxygen atoms from the CuO chains leading to defects in the chains and small modifications to the lattice parameters [17].

The large anisotropy of YBCO due to the chains is not present in $Bi_2Sr_2Ca_{1-\delta}Y_\delta Cu_2O_8$ (BSCCO-2212), whose body-centered-tetragonal unit cell is represented in Fig 2.3. The lattice parameters are a = b = 3.817Å and c = 30.5Å. This material is an insulator for

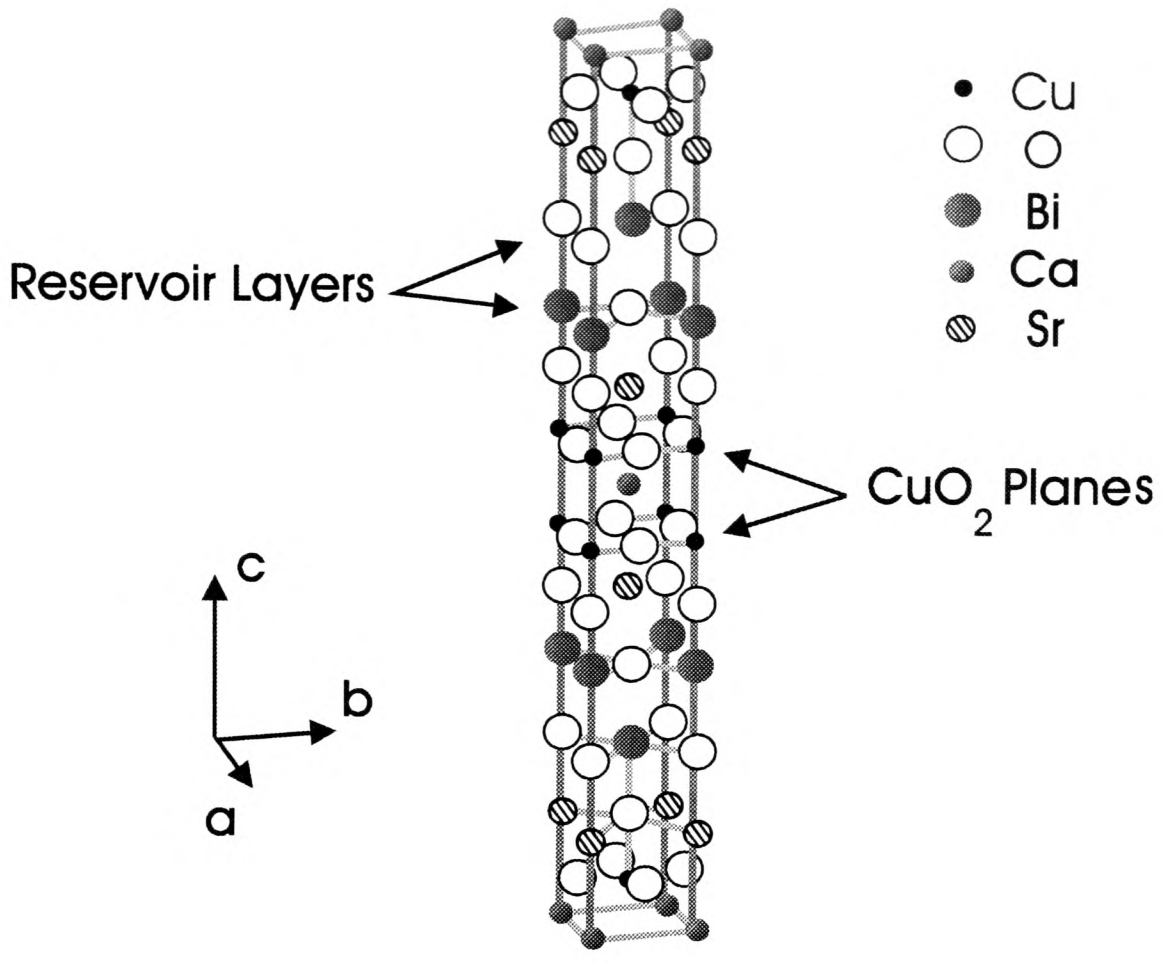

Figure 2.3: Unit cell of $Bi_2Sr_2Ca_{1-\delta}Y_\delta Cu_2O_8$. The diagram shows two reservoir layers and the two CuO_2 planes. The structure is tetragonal with the lattice parameters a = b = 3.817Å and c = 30.5Å.

$0.43 < \delta < 1$, whilst $0 < \delta < 0.43$ provides a superconducting phase. There are two superconducting CuO_2 layers and two reservoirs layers formed by BiO layers. A maximum $T_c = 85K$ is obtained for $\delta = 0$[1].

The structure of $Tl_2Ba_2CuO_{6+\delta}$ (TBCO-2201), shown in Fig 2.4, is also tetragonal with only one copper oxide plane. The maximum $T_c = 85K$. Ren et al. [18] demonstrated the possibility to obtain the full doping dependence from highly overdoped samples with $T_c = 11K$ to highly underdoped with $T_c = 36K$ only by varying the annealing time and temperature in a flowing argon atmosphere.

[1] BSCCO-2223 with three CuO_2 layers has a $T_c = 110$ K.

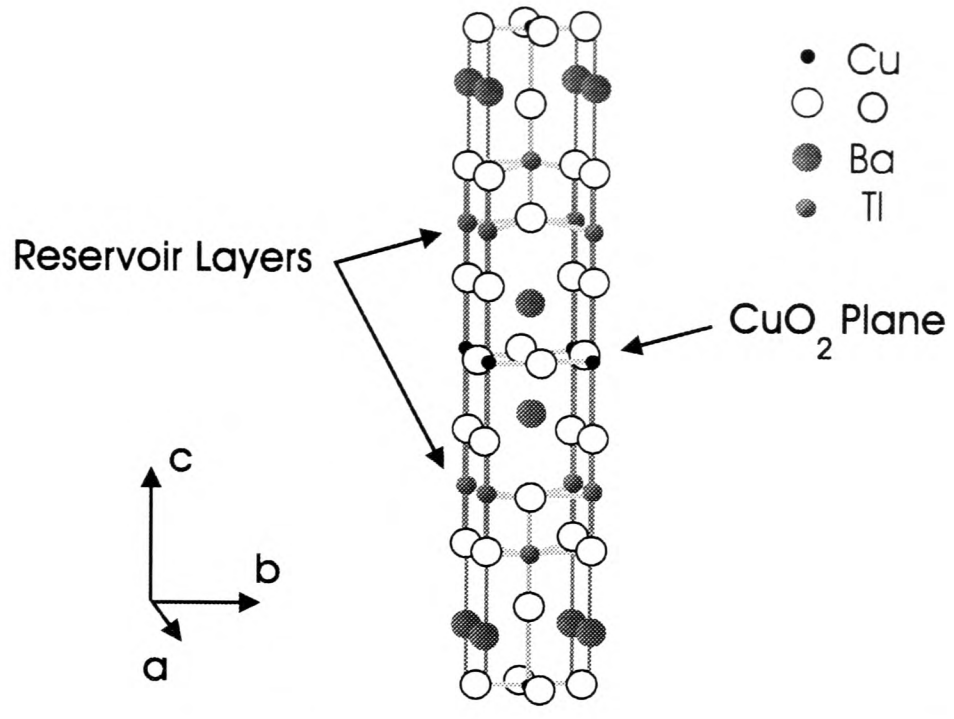

Figure 2.4: Unit cell of $Tl_2Ba_2CuO_{6+\delta}$. The diagram shows the two reservoir layers and the CuO_2 plane. The structure is tetragonal with the lattice parameters a = b = 3.817Å and c = 23.2Å.

2.4 Anisotropy

As already stated, the cuprate superconductors have in common a structure of copper oxide planes separated by other ions. This structure leads to highly anisotropic properties both in their normal and superconducting states.

At room temperature, the dc resistivity of $La_{1.85}Sr_{0.15}CuO_4$ for a current parallel to the plane is roughly 200 times smaller than for a current perpendicular to the planes. Similar high anisotropies in resistivity are seen for all the cuprate superconductors and an anisotropy is also clearly seen in optical conductivity, thermal conductivity and optical reflectivity [19]. The in-plane coherence length ξ in $YBa_2Cu_30_{7-\delta}$ is approximately 7nm (18.4 unit cells) and 1.5nm perpendicular to the planes (1.3 unit cells) [20], which is much smaller than the coherence length in pure elemental superconductors such as aluminium ($\xi = 1.6\mu$m). Finally, in $Bi_2Sr_2CaCu_20_8$, c-axis electrical conductivity experiments suggest quasi-2D superconducting pairs [21].

In the case of YBCO-123 which has CuO chains as well as CuO_2 planes, the normal state properties show a strong in-plane anisotropy of many properties in addition to the in- and out-of-plane anisotropies discussed above [19]. The in-plane anisotropy is discussed in detail in chapter 7.

2.5 Electronic Properties

The cuprates contain one or more copper oxide planes, as illustrated in Fig 2.2 - 2.4. Charge reservoir layers above and below the CuO_2 planes can accept or donate electrons to the planes. In the case of YBCO, the charge reservoirs are CuO chains, however in most HTSC, the reservoirs have a plane structure[2]. The electron interaction between the reservoirs and the planes are achieved by chemical substitution of ions of different valence, as in $La_{2-x}Sr_xCuO_4$; by changing the oxygen stoichiometry in charge reservoir layers, as in $YBa_2Cu_30_{7-\delta}$; or by substitution with isovalent ions of different radius. High-temperature superconductivity has been observed in both electron- and hole-doped materials; the majority of the materials are hole-type conductors and we focus here on hole-doped materials.

A schematic phase diagram of HTSC as a function of doping is given in Fig 2.5. Below the Néel temperature T_N, HTSC materials are antiferromagnetic insulators at low hole concentration. As the hole concentration p increases[3], T_N decreases and at approximately $p = 0.05$, the long-range antiferromagnetic order ceases. In the doping range $0.05 \lesssim p \lesssim 0.25$, the materials exhibit superconductivity at low temperatures. The maximum critical temperature depends on the compound and particularly on the number of CuO_2 planes per unit cell. The maximum is achieved at $p \cong 0.15$, called the optimally-doped level. Below and above this doping level, the material is underdoped

[2]The reservoir layers are TlO planes for TBCO-2201 and BiO planes for BSCCO-2212.
[3]The hole concentration p is measured in holes per Cu ion in CuO_2 plane [22].

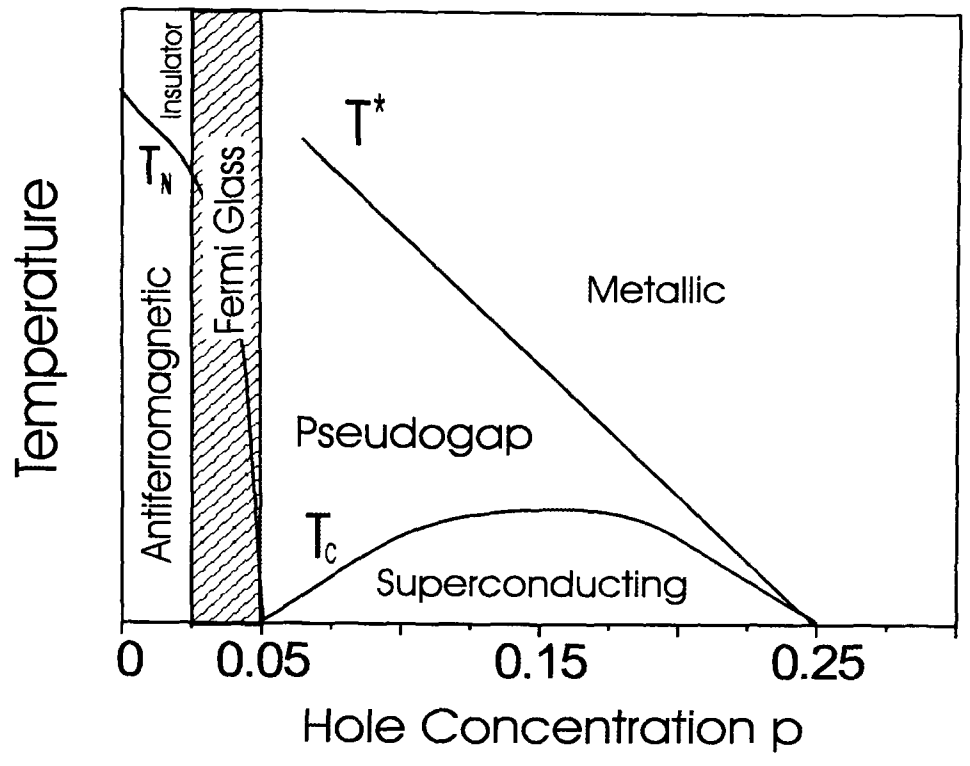

Figure 2.5: Schematic phase diagram of HTSC with the critical temperature T_c, the Néel temperature T_N and the pseudogap temperature T*.

and overdoped respectively. When the hole concentration is further increased, above $p = 0.25$, superconductivity vanishes and the material behaves as an ordinary metal according to transport properties [23].

2.5.1 Undoped Regime

Both band structure calculations and chemical valency considerations indicate that undoped materials should be metallic. However, due to a strong Coulomb repulsion on Cu $d_{x^2-y^2}$ orbitals, they are believed to be Mott-Hubbard insulators [24]. The electronic structure of CuO_2 plane can be described by models generalizing the Hubbard Hamiltonian, where the bands originate from Cu $d_{x^2-y^2}$ and O p_x, p_y orbitals [25]. The Hubbard mechanism splits the Cu d-band into two, the upper and lower Hubbard bands, with a large correlation gap of about 8eV.

Below the Néel temperature T_N, the unpaired holes of the Cu^{2+} ions are antiferro-

magnetically coupled to the oxygen O^{2-}. The maximum value of T_N is on the order of several hundred Kelvins, being approximately 420K in $YBa_2Cu_30_6$. With increasing hole doping p, T_N decreases rapidly. As the doping is further increased, photoconductivity data [26] indicate that the states at E_F are localized: this ground state is termed a Fermi glass [27]. Localized holes in this state move via thermally-activated hopping with a hopping barrier of approximately 0.1eV. The localization has been argued to be due to disorder caused by Anderson localization [28]. However, polaron formation can also give rise to the observed effects [29].

2.5.2 Superconducting State

The presence of Cooper pairs with zero net momentum was inferred from ac Josephson [30] and flux quantization [31] measurements. Moreover, Knight shift measurements [32] imply that pairs are most likely singlet. It was also shown that HTSC have a very short coherence length ξ, on the order of a unit cell. Therefore, if one calculates the number of Cooper pairs that exist within the radius of one pair, one obtains 1 to 10 pairs, in contrast to 10^6 in conventional superconductors. As a consequence of the short coherence length, large thermodynamical fluctuations are expected in HTSC [2].

One of the most interesting properties of HTSC is the temperature dependence of the electronic specific heat [3]. Unlike in conventional superconductors, where there is a step-like increase in the electronic specific heat c_p as the temperature is lowered through T_c [15], c_p shows strongly anomalous behaviour in the cuprates. In optimally-doped $YBa_2Cu_3O_{7-\delta}$, c_p shows a similar behaviour at T_c as the λ-transition of ^4He [33]. In other cuprates, the peak is symmetrical with no jump at T_c. Moreover, the magnetic field dependence of the electronic specific heat shows that the peak does not shift in temperature with increasing the magnetic field [3]. This behaviour is expected for a weakly interacting Bose gas [33], but not for a BCS-like superconductor.

Other properties of HTSC which will be of importance for this thesis include the phonon and thermal conductivity properties. A good discussion of the phonons can be found in reference [34]. Information on many properties of HTSC, including the thermal conductivity, can be found in references [17, 19].

2.5.3 Pseudogap State

Various physical properties that are determined by low-energy excitations show anomalies corresponding to a reduction in the density of states near the Fermi energy at temperatures above T_c. This decrease in the density of states is referred to as the pseudogap [4]. A pseudogap has been consistently observed by numerous experimental techniques in HTSC. It was first observed in underdoped $YBa_2Cu_3O_{7-\delta}$ by NMR measurements [35], where a decrease in the Knight shift was observed instead of a temperature-independent Pauli susceptibility. Since NMR probes the spin channel, the pseudogap was assumed to be a spin gap. Further experiments probing the charge channel revealed that the pseudogap exists for both spins and charges, including heat capacity [5], transport [36], infrared [37], angle-resolved photoemission spectroscopy (ARPES) [38, 39], Raman [40] and scanning tunnelling spectroscopy [41].

The onset temperature T^* of the pseudogap state is a crossover where the anomalies are observed, but not a phase transition since no singularities in thermodynamic quantities are observed. Consequently, T^* strongly depends on the experimental technique and also on the model used to interpret the data. Therefore, different phase diagrams have been proposed on the basis of the available experimental data. In all experiments, the pseudogap temperature T^* increases linearly as the doping is decreased from the optimally-doped level [41], whereas in the overdoped regime, T^* follows the doping dependence of T_c as illustrated in Fig 2.5. The pseudogap appears to have a $d_{x^2-y^2}$ symmetry [38, 39] and the thermal data indicate that it has equal spin and charge density

character [5].

Various mechanisms have been proposed to explain the origin of this gap in the normal state. Emery and Kivelson [42] consider the formation of paired states below the critical temperature T*, which become phase coherent at T_c. Lee and Wen [43] have suggested that the thermal excitation of low-energy excitations is sufficient to destroy a small superfluid particle density while the relatively large gap remains intact. More recently, Schmalian et al. [44] have argued that the nearly antiferromagnetic Fermi liquid model can account for the pseudogap behaviour.

2.5.4 Normal State

As for the superconducting properties, there is still no consensus on the theoretical understanding of the normal state properties of HTSC. The most controversial issue is whether the ground state is Fermi liquid-like or not. Angle-resolved photoemission spectroscopy (ARPES) data on optimally-doped $Bi_2Sr_2CaCu_2O_{8+\delta}$ [39], $YBa_2Cu_3O_7$ [45], $Nd_{1-x}Ce_xCuO_4$ [46], as well as on underdoped $Bi_2Sr_2CaCu_2O_{8+\delta}$ [39] show a large Fermi surface consistent with the Luttinger theory and the Fermi liquid picture. On the other hand, transport measurements [47] show that the conductivity is proportional to the doping, implying that HTSC behave more like doped semiconductors.

2.6 Pair symmetry

The Cooper pairs in a BCS superconductor have zero angular momentum i.e. they have an s-wave symmetry. Consequently, their wavefunction is isotropic in k-space from which it follows that the superconducting gap is also isotropic. Evidence has grown that this is not the case in cuprate superconductors. Instead, experiments suggest that the pair wavefunction has a predominantly d-wave symmetry and that the gap in the quasiparticle

dispersion has nodes. We will first discuss some of the evidence for predominantly d-wave Cooper pairing in cuprate superconductors and then discuss what effect a d-wave gap might have on the carrier dynamics probed by ultrafast laser experiments.

The experiments on pairing symmetry fall into two main categories depending on whether they probe the k-dependence of the magnitude of the gap or the phase of the pair wavefunction. The most direct method for probing the k-dependence of the gap energy is angle-resolved photoemission spectroscopy (ARPES), as performed on $Bi_2Sr_2CaCu_2O_8$ by Ding et al. [48, 49]. These experiments measure the energy of the highest occupied electron state for different directions in k-space relative to the Fermi energy, and an anisotropic gap with maxima along the (100) directions has been observed. However, it must be noted that photoemission is a complex process which only probes the surface of the sample and thus some doubts remain concerning the interpretation of the data.

A range of different experiments have been performed to probe the angle dependence of the phase of the pair wavefunction. One class of such experiments, the tricrystal experiment, is based on scanning SQUID microscope measurements of flux quantization in thin film superconducting rings grown on specially designed substrates [50]. The $SrTiO_3$ substrates consist of three crystals fused together with non-parallel crystal axes, as illustrated in Fig 2.6. The superconductor grows epitaxially on the crystals with the same crystal orientations as the substrates. The angle between the crystal axis at the junctions are chosen so that Cooper pairs passing around a loop of superconductor containing the junction of the three substrates would experience a π phase change in a predominantly d-wave superconductor, but not in an s-wave superconductor. This extra π phase shift leads to the magnetic flux trapped in such a ring being given by $(n + \frac{1}{2})h/2e$, where n is an integer, rather than $nh/2e$ which would be the case for a s-wave superconducting rings. An $(n + \frac{1}{2})$ quantization condition observed by Tsuei et al. [50] for YBCO-123, ring 3 in Fig 2.6, but not in other rings away from the junction,

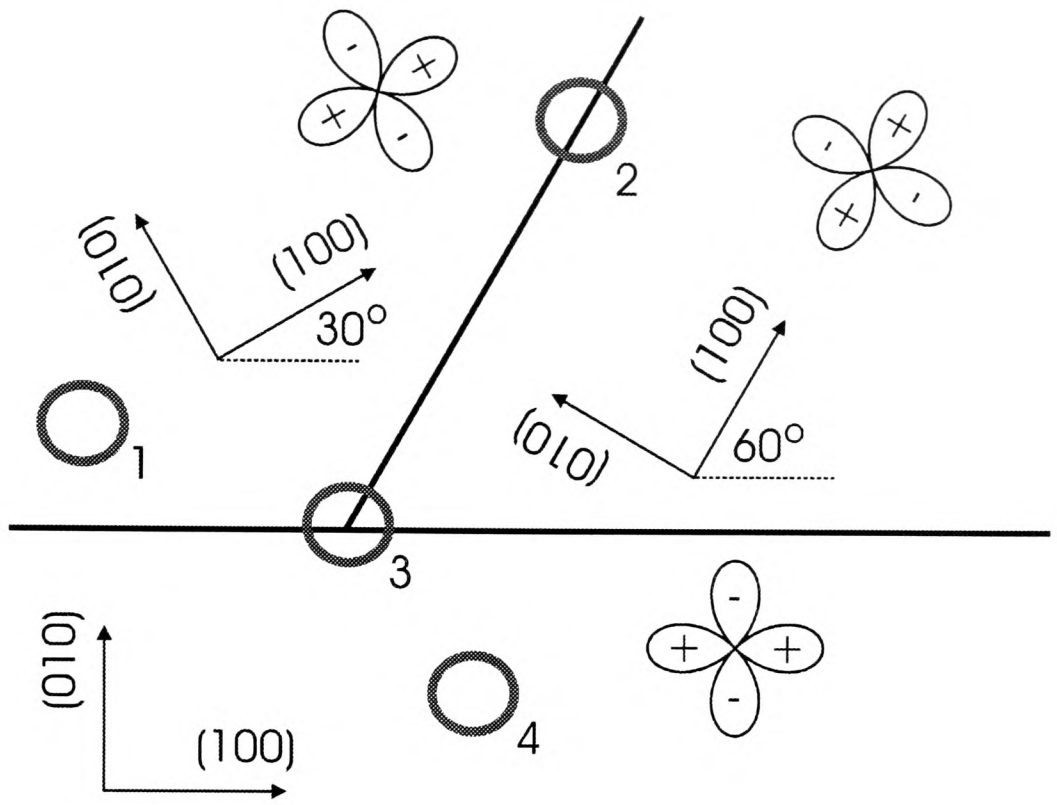

Figure 2.6: Illustration of four YBCO-123 superconducting rings on a tricrystal substrate with a π-ring geometry. The solid lines indicate the positions of the grain boundaries. The four-leaf clovers indicate the orientations of the assumed d-wave symmetry gaps aligned with the crystalline axes.

rings 1,2 and 4, indicates d-wave gap symmetry. However, as the full angle dependence is not measured, some doubt remains about the interpretation of the tricrystal experiment.

The presence of nodes in the quasiparticle dispersion has many implications for the properties of the superconductor and there is considerable indirect evidence for them. The lack of a gap in the quasiparticle density of states, as illustrated in Fig 2.7, has important consequences on the temperature dependence of any property which depends on the number of thermally-excited unpaired carriers. For instance, the low-temperature electronic heat capacity follows a temperature power law T^{α} with $0 \leq \alpha \leq 2$ [17], rather than the activated temperature dependence $e^{-\frac{bT_c}{T}}$ with b $\cong$ 1.5 [15] of the BCS superconductors. The lack of a gap in the single particle density of states also affects the

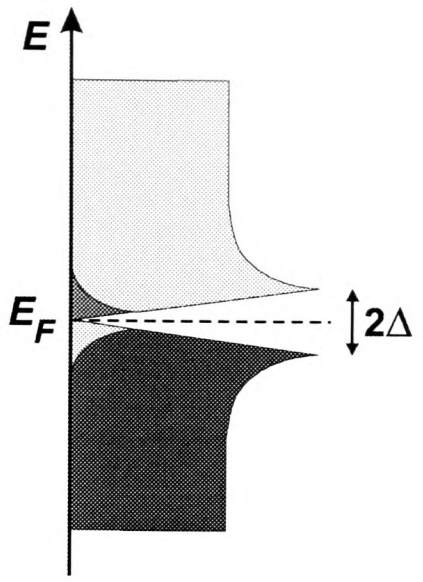

Figure 2.7: Quasiparticle density of state for a d-wave superconducting gap at a temperature above absolute zero but below T_c. The unpaired occupied states are in dark grey and the unpaired unoccupied states in light grey.

temperature dependence of the number of Cooper pairs which can be measured by the penetration depth of microwave radiation [51].

The evidence of these experiments amongst others means that the concept of d-wave pairing or at the very least a superconducting gap with nodes is widely accepted to be the case in all the cuprate superconductors with the possible exception of $Nd_{2-y}Ce_yCuO_4$.

A predominantly d-wave gap will also effect the dynamics of the non-equilibrium carriers excited by an ultrafast laser pulse. In s-wave superconductors, there is a minimum energy for scattering carriers across the gap, however, in a d-wave superconductor, the minimum scattering energy will be dependent on the scattering wavevector. The dynamics of carriers near the superconducting gap will be modified by the k-dependence of the density of available final states. The condensation of quasiparticles into Cooper pairs will be strongly affected by the anisotropic carrier distribution as the states near the nodes have by definition the least overlap with the superconducting state [52]. Much theoretical and experimental work still needs to be done on this subject in order to elucidate all the modifications of the dynamics of non-equilibrium carriers due to a d-wave pairing

symmetry.

It has to be noted that the work of Kabanov et al. on ultrafast dynamics in $YBa_2Cu_30_{7-\delta}$ [53] concludes to an s-wave symmetry. Their interpretation will be discussed in detail in section 4.6.

2.7 Pairing Interaction

The determination of the pairing interaction responsible for the high-superconducting transition temperatures in the cuprate superconductors is the central aim of nearly all fundamental research on these materials. There are many competing theories and we present here only a brief review of some of the most important models. The BCS theory relies on the assumption that the normal state can be described by a Fermi liquid. However, the differences between the non-superconducting state in the cuprate and a Fermi liquid have led to the formulation of non-Fermi liquid theories. We review here first the three main non-Fermi liquid theories.

The Interlayer Coupling Model (ICM) of Anderson and co-workers [54] is based on the hypothesis that the normal state carriers are localized in the CuO_2 planes, with only incoherent transport between planes, but that superconducting pairs are able to tunnel coherently between planes. The decrease in energy due to carrier confinement leads to the strong pairing interaction and high critical temperatures. This model is a variation to the idea proposed by Anderson already in 1987 of having a resonating valence bond (RVB) state as the alternative to the Fermi liquid [55]. The excitations are considered to be spinons and holons originating from a 2D extension of the Luttinger liquid theory. The separation of spin and charge degrees of freedom within the CuO_2 layers causes the transport in the c-axis direction to be incoherent. However, if the holons form pairs, tunneling becomes coherent, thereby lowering the energy of the ground state and giving rise to the formation of a superconducting state. The symmetry of the ground state is

predicted to be highly anisotropic s-wave, with suppression of the gap occurring along (110) directions. The ICM has been successful in explaining the c-axis transport properties [56] and the c-axis plasma frequency in the superconducting state [57]. However, the correlation between the c-axis plasma frequency and T_c predicted by the theory is not confirmed experimentally [58]. The theory is supported by measurements of far infrared conductivity normal to the CuO_2 planes which show incoherent transport for normal carriers and coherent transport for superconducting carriers [57].

The polaronic and bipolaronic theories [27] hypothesize that the carriers forming the superconducting pairs are polarons or bipolarons. The electron-phonon interaction required to produce polarons is stronger than in the BCS theory and high critical temperatures are possible. In the bipolaronic form of this theory, polarons form bound pairs at a temperature above T_c and undergo the Bose condensation at the superconducting transition. These preformed pairs have been used to explain the pseudogap reported in cuprate superconductors (cf. section 2.5.3 for details). In the superconducting state, the isotope effect and the thermoelectric power data can be described using bipolarons, while in the normal state, the linear resistivity and the Hall effect are also explained using this theory.

The present leading non-Fermi theory of HTSC is the dynamical stripe theory. Mook et al. [59] and Sharma et al. [60] present data from neutron scattering and ion channelling, probing the spin and ion-lattice fluctuations, which are difficult to explain with the previous theories. A high degree of cooperativity is needed to explain these observations and the best interpretation is found in the new stripe theory developed by Emery and co-workers [42]. The stripes consist of antiferromagnetic, and presumably insulating, domains about a nanometer in width, separated by domain walls on which the charge carriers reside. The current consensus is that they arise from the competition between quantum kinetic energy and electron-electron interactions on the microscopic scale. The

stripes were first observed in the structural studies of $La_{1-x}Sr_xCuO_4$ using extended X-ray absorption fine structure spectroscopy [61]. The phase separation was found to be dynamic [62]. The dynamical stripes are disordered by long wavelength quantum fluctuations and hence the superconducting states are seen as localized carriers in 1D "rivers" whose path is constantly fluctuating.

In the nearly antiferromagnetic Fermi liquid theory of Scalapino and co-workers [64, 65, 66], and Pines and co-workers [67], the normal state is modeled as a Fermi liquid. The basis of the theory is that antiferromagnetic spin fluctuations are the most important scattering mechanism in the normal and superconducting states. The superconducting state is treated in a BCS-like manner, with the phonons being replaced by short range antiferromagnetic spin fluctuations which provide a strong enough electron-electron attraction to give high critical temperatures. This model has been successful in explaining NMR [65], optical conductivity [66] and d-wave gap symmetry [64].

In addition to the theories of Scalapino and Pines, there are a range of other theories which can be characterized as being BCS-Fermi liquid models but with bosons other than phonons. Candidates include excitons and plasmons [17]. The large energy of these hypothesized bosons means that only a weak coupling is required between them and the superconducting carriers to give high critical temperatures. These theories are the motivation of the experimental work by Holcomb et al. [68] in which the existence of high-energy coupling bosons was inferred from changes in optical reflectivity from 1 to 2eV at the superconducting transition (cf. section 2.10 for detail). However, apart from this work, experimental support for these theories is scant.

2.8 Superconducting Fluctuations

Corson et al. [69] have developed a coherent time-domain spectroscopy technique that probes the conductivity in the frequency range between 100 and 600 GHz. They measured the frequency-dependent conductivity, which relates the alternating current flowing in the superconductor to an applied alternating electric field. This technique measures the phase stiffness ρ_s, which is the strength of the long-range phase coherence of the Cooper pairs. The current carried by the Cooper pairs is proportional to the spatial gradient of the Cooper pair phase and hence the phase stiffness can be extracted from the conductivity measurements. In $Bi_2Sr_2CaCu_2O_{8+\delta}$, they observed that for $T \ll T_c$ the phase stiffness ρ_s is large and frequency independent; for $T \simeq T_c$, ρ_s is non-vanishing at high-frequency (short length scales) but vanishing at low-frequency (long length scales); and for $T \gg T_c$, ρ_s vanishes at all length scales. Corson et al. could extract from the frequency-dependent phase stiffness, the temperature dependence of the phase correlation time τ of BSCCO-2212.

The dynamical phase stiffness dependence was interpreted by Corson et al. [69] as the signature of a Kosterlitz-Thouless-Berezinskii (KTB) transition [70, 71]. In this two dimensional melting theory, the phase coherence is controlled by thermally-generated vortices[4]. The phase change around a vortex is 2π. Below T_c, any vortices present are tightly bound in pairs of opposite circulation, at temperatures close to T_c a few unbound vortices are present and finally, at temperature well above T_c there is a proliferation of unbound vortices. In other words, in the ordered state vortices bind into pairs of opposite vorticity and the transition to the disordered state occurs when the first unbound vortices appear. Corson et al. [69] interpreted their experiments as a signature of a KTB transition because of the dynamical phase stiffness and of the finite, frequency-dependent phase correlation time.

[4] A vortex is a thermally-generated topological defect in the macroscopic superconducting phase.

2.9 Band Structure

The electronic band structure of YBCO-123 is exceedingly complicated [24]. Local Density Approximation (LDA) calculations of $YBa_2Cu_3O_6$ failed to predict that it is an insulator. However, the LDA calculations for $YBa_2Cu_3O_7$ have been checked against ARPES and inverse photoemission measurements and show reasonable agreement except that they fail to predict a strong van Hove singularity observed near the Fermi energy [72]. Consequently, the LDA band structure can be taken as a reasonable guide to the real band structure but is not quantitatively reliable. The calculations predict that the CuO_2 plane bands at the Fermi energy in which the superconducting carriers reside are derived from the Cu-d and O-p states.

Linear Augmented Plane-Wave band structure calculations of $Bi_2Sr_2CaCu_2O_8$ have been reported [73] and are presented in Fig 2.8a. The occupied states consist primarily of bands evolving from the Cu($3d$)-O($2p$) hybridization and the unoccupied bands have predominant Bi($6p$) character. The bands are strongly two-dimensional, the c-axis dispersion being only 0.1eV. The Fermi energy intersects the antibonding Cu($3d$)-O($2p$) bands (solid squares) and antibonding Bi($6p$)-O($2p$) bands (solid triangles). The total carrier density, $8.8{\cdot}10^{21}cm^{-3}$, is relatively low with about $4{\cdot}10^{21}$ carriers/cm^3 in each of the CuO_2 planes. From the same calculations, it is possible to obtain the total density of states, presented in Fig 2.8b, showing that the density of states at E_F is relatively low with 3.0 states/eV cell. Possible pump (3eV) and probe (1.5eV) transitions in ultrafast experiments are also illustrated in Fig 2.8b.

2.10 Optical Properties of $YBa_2Cu_3O_{7-\delta}$

In this section, we focus on the optical properties of YBCO-123 in the energy range of 0.5 to 3.5eV, for a probe electric field lying in the a-b plane. The transmission spectra

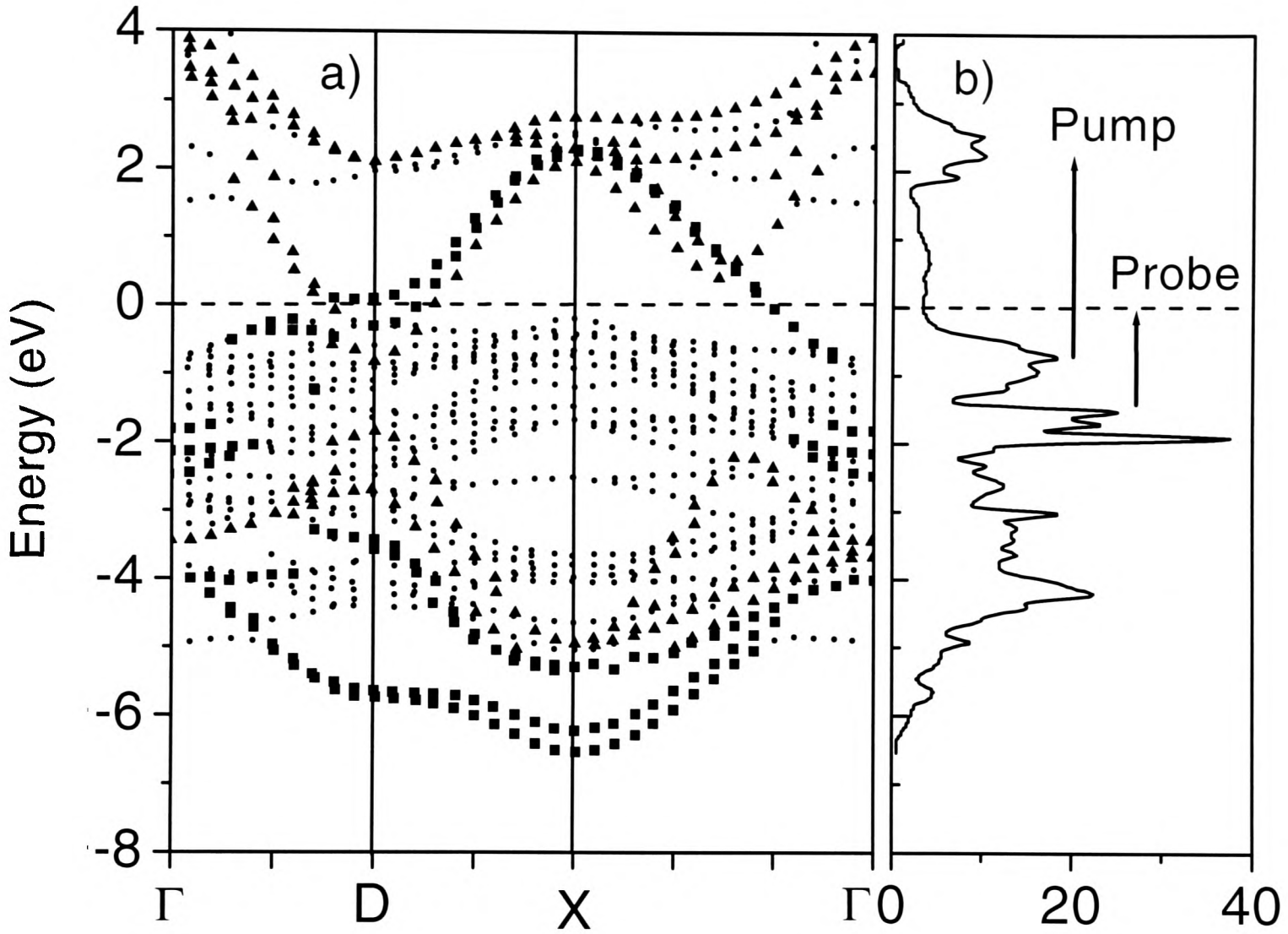

Figure 2.8: (a) BSCCO-2212 band structure by Linear Augmented Plane-Wave calculations [73] with antibonding Cu-O bands (solid squares) and antibonding Bi-O bands (solid triangles). (b) Total density of states with the possible pump (3eV) and probe (1.5eV) transitions.

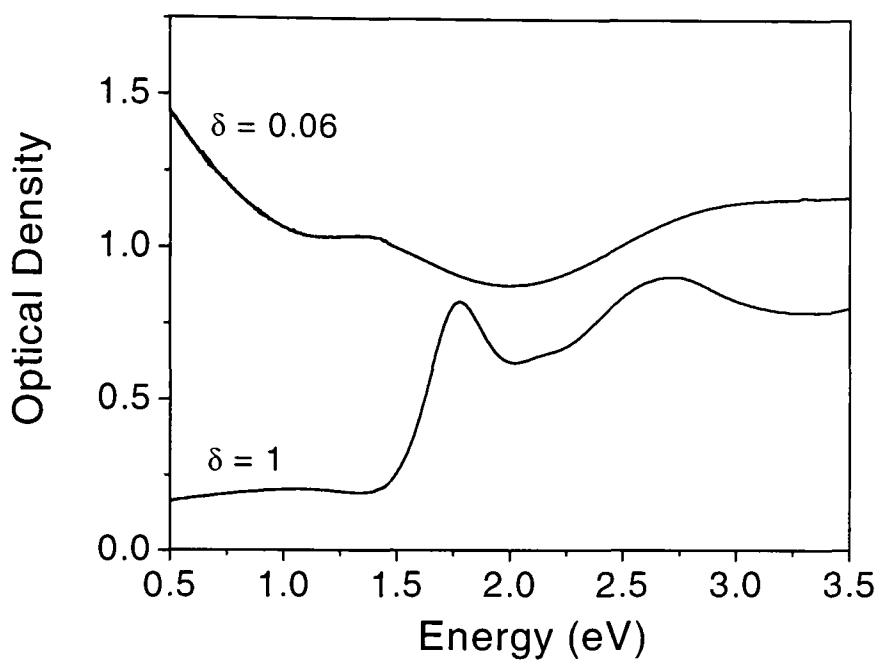

Figure 2.9: Optical absorption spectrum of $YBa_2Cu_3O_{7-\delta}$ at 4K in the insulating ($\delta = 1$) and the superconducting ($\delta = 0.06$) phase.

measured at 4K for an optimally-doped and an insulating ($\delta = 1$) sample are shown in Fig 2.9. These spectra are in agreement with published data [23, 74].

The insulating sample shows an absorption gap below 1.5eV, a peak at 1.7eV and another peak at 2.7eV. Resonant Raman scattering measurements indicate that these transitions are due to charge transfer excitations where an electron transfers from oxygen to copper within the CuO_2 planes [75]. As the oxygen content of YBCO is increased, the transmission spectra show an increasing absorption at energies below 1.5eV and a decrease in the strength of the peak at 1.7eV.

The transmission spectra of the optimally-doped material shows a decrease of the signal with energy at low energies and broad features at approximately 1.4eV and 2.7eV. The 2.7eV peak is seen over the entire range of doping and is associated with the peak at the same energy in the insulating material. The feature at 1.4eV does not seem to be related to the features observed in the insulating phase of YBCO. Several transitions might possibly explain this peak in terms of an interband transition, including plane-to-chain transitions. The low-energy decrease in transmission observed in optimally-

doped material is observed in reflectivity measurements as an increasing reflectivity with decreasing energy. The origin of this feature in the optical response of YBCO has been explained in two different ways. First, the feature was assigned to the sum of a Drude response due to the normal carriers and at least one mid-infrared absorption band [23]. The mid-infrared absorption is hypothesized to be due to localized carriers, which are in a broad band with a small semiconducting gap. Secondly, it has been suggested that the feature is the Drude response of the normal carriers modified by a scattering rate which increases strongly with frequency (extended Drude model[5]). Both models give reasonable fits to the reflectivity spectra.

In this thesis, we are interested in any part of the optical response of HTSC which can be used to probe the carrier dynamics associated with superconductivity. One obvious approach is to look for changes in the optical response with temperature which correlate with the superconducting transition. Holcomb et al. [68] found such changes by measuring the thermal differential reflectance (TDR) of HTSC around T_c, as shown in Fig 2.10 for YBCO-123. The TDR signal at T_c is the ratio of the reflectivity just below T_c with the reflectivity just above T_c. They explained the spectrum in terms of the Eliashberg theory [16], an extension of the BCS theory assuming that bosons of energy around 1.7eV are involved in the pairing interaction. The predicted TDR spectra, observed for HTSC other than YBCO, have a differential-like shape and not a square shape as in Fig 2.10. However, as the TDR experiment was performed on a twinned crystal, two plasma frequencies are present [76], one for the planes and one for the chains, explaining the particular shape of the YBCO spectrum.

Another possible explanation of the spectra observed by Holcomb et al. is that the feature is due to changes in interband transitions, involving initial or final states near the Fermi energy, which are modified by the opening of the superconducting gap.

[5] The extended or modified Drude model is the Drude model with the scattering rate linearly dependent on frequency ($\Gamma \propto \omega$).

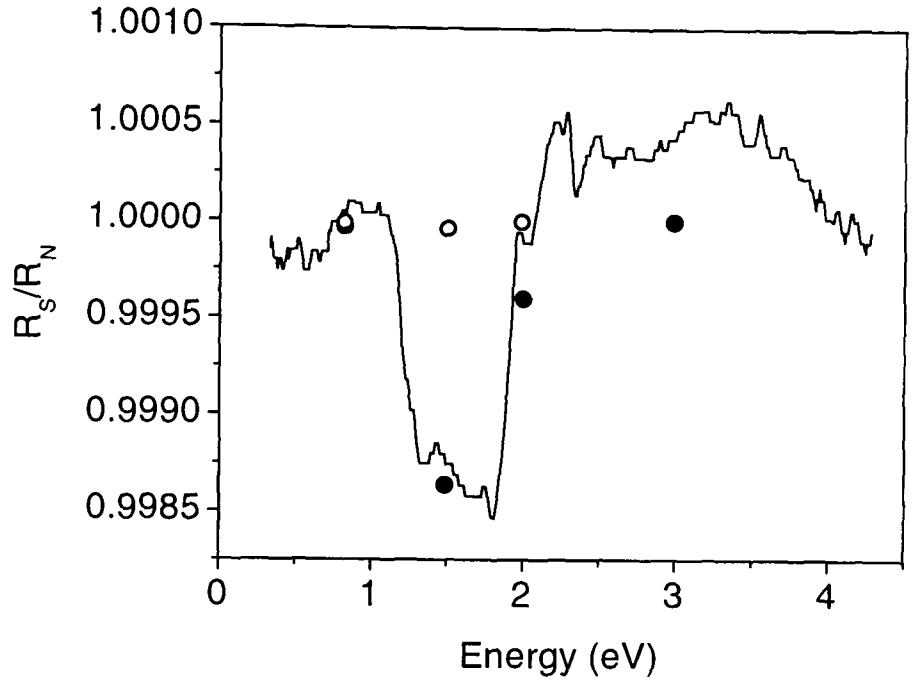

Figure 2.10: Thermal differential reflectance (TDR) of $YBa_2Cu_3O_{7-\delta}$ measured by Holcomb et al. at T_c [68]. Photo-induced reflectivity measurements as a function of the probe photon energy indicate that the induced signal is proportional to the TDR signal. The solid circles are the signal magnitude at 4K, whilst the open circle are above T_c.

The TDR peak centered around 1.5eV for YBCO is related to superconductivity and justifies the choice of 1.5eV for the probe photon energy in time-resolved experiments presented here. Preliminary photo-induced reflectivity measurements, also shown in Fig 2.10, indicate that the induced reflectivity signal is proportional to the TDR signal. Unfortunately, TDR data are not available for BSCCO-2212 and TBCO-2201 studied in this thesis.

Chapter 3

Ultrafast Time-Resolved Spectroscopy

3.1 Introduction

The development of picosecond and sub-picosecond pulsed lasers over the last two decades has allowed the dynamics of excitations to be measured directly in the time domain. In time-resolved spectroscopy, the temporal evolution of an optical signal is monitored, the signal being for example the luminescence spectrum, the change of reflection or transmission or Raman scattering. Since the characteristic time constants can be as short as a few tens of femtoseconds, this field of research is know as ultrafast spectroscopy. A lot of work has been devoted to this topic by various groups [77] mainly for semiconductors. In this chapter, we will discuss the ultrafast time-resolved reflection and transmission techniques used in this thesis, that allow measurements of non-equilibrium dynamics to be made on a femtosecond timescale.

The first section of this chapter introduces the general set-up of the pump-probe experiment. Three different types of experiment have been used in this thesis, a pump-

probe experiment with a time resolution of 140fs for most results presented in chapters 5 and 7, a 35fs resolution experiment for chapter 6 and a white light probe experiment for measuring the wavelength dependence of the dynamics. The next section of this chapter deals with the mode-locked lasers related to our experiments and the techniques used to characterize them. The cryogenic techniques used to enable measurements in the temperature range of 4 to 300K are briefly introduced. Finally, the preparation and characterization of the different samples used in this thesis are presented in the last section.

3.2 Pump-Probe Reflection and Transmission Experiments

In pump-probe experiments intense laser pulses excite the sample to a non-equilibrium state and its relaxation to equilibrium is probed by measuring the changes in reflection or transmission of a second, weaker pulse. The time dependence is given by the time delay between the pump pulse and the probe pulse. The quantity measured in this experiment is the photo-induced reflection $\mathcal{R} = \Delta R/R(t)$ or the photo-induced transmission $\mathcal{T} = \Delta T/T(t)$. In the case of the reflection, $\mathcal{R}(t) = (R(t) - R_{cw})/R_{cw}$, where R_{cw} is the dc reflectivity without the excitation of the pump pulse.

In semiconductor experiments usually only the transmission of the probe pulse is measured and the variations are interpreted as being due to changes in the absorption coefficient i.e. in the imaginary part of the refractive index. In order to measure the photo-induced changes in both the real and imaginary parts of the refractive index, it is necessary to record both the reflection and transmission signals at the same time. However, most of our measurements are only on photo-induced reflectivity, as it is not possible to measure the transmission of single crystals and opaque thin films.

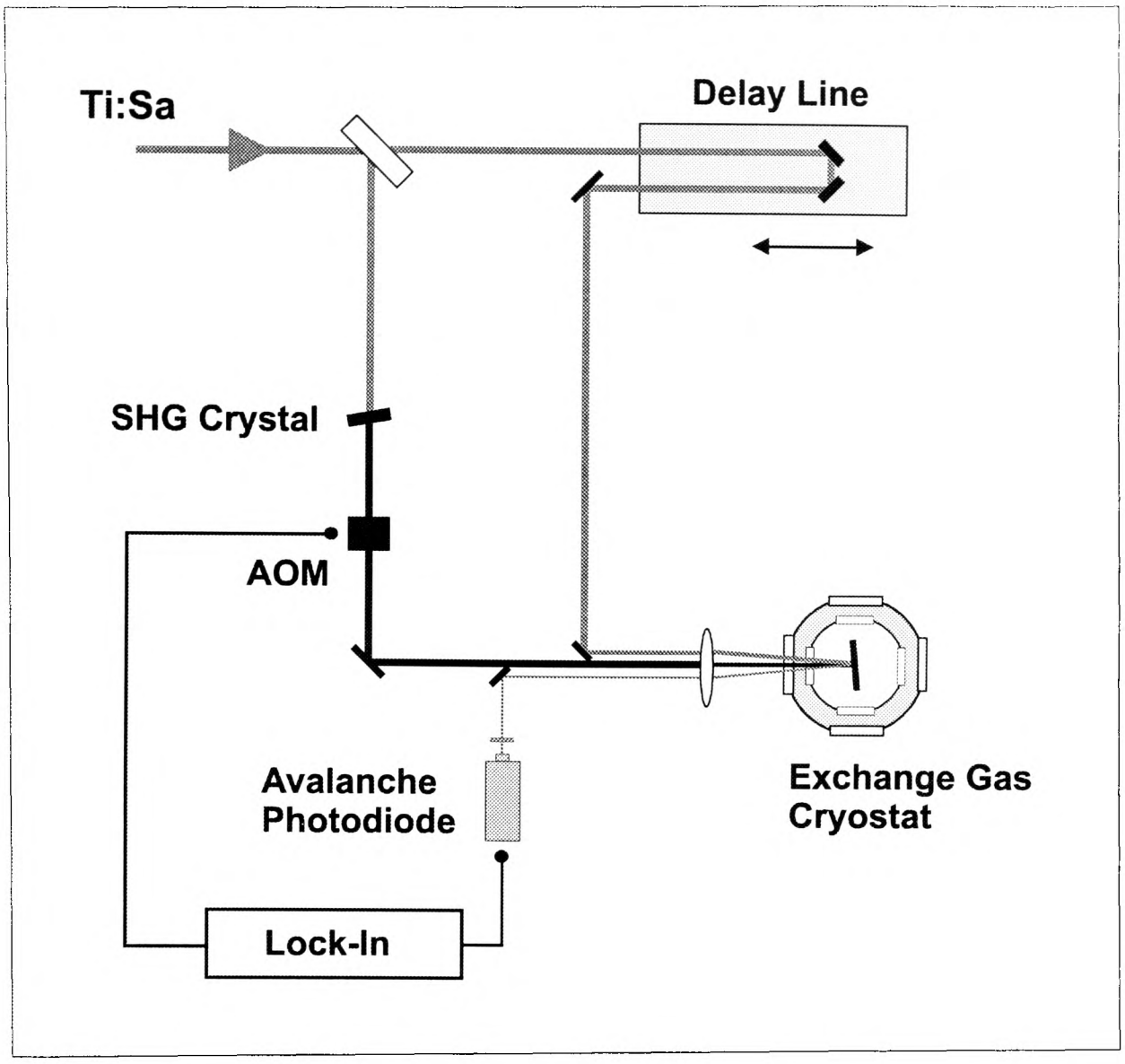

Figure 3.1: A schematic of the pump-probe time-resolved experimental set-up used for the 140fs resolution experiment.

The time resolution of the experiment is given by the autocorrelation of the pump and probe pulses measured in the cryostat at the sample, as explained in detail in section 3.3.3.

3.2.1 140fs Resolution Experiment

In this experiment, the laser provides ~70fs pulses at 800nm. A schematic diagram of the set-up is shown in Fig 3.1. Each ultrafast pulse from a Titanium Sapphire laser is split into two paths by a beamsplitter to provide the pump and probe pulses. The probe beam is then reflected from a retroreflector mounted on a translation stage in order that

its path length and thus its time of arrival at the sample can be modified with respect to the pump. The probe path length can be controlled to within 2μm i.e. 6.7fs and thus, the time resolution of the experiment is limited by the temporal length of the pulse and not by the precision of the translation stage.

In this experiment, a non-degenerate configuration is used, meaning that the pump photon energy is different from the probe energy. The pump pulses are frequency-doubled from 1.5eV (800nm) to give blue light at 3eV, with any residual red component being filtered out. The second harmonic generation [78, 79] is achieved with a non-linear BBO crystal, allowing the generation of 100fs pulses of blue light, with an average power of 100mW. The pump beam is modulated by an acousto-optic modulator (AOM) at 1MHz, which is part of the high-frequency lock-in detection system, discussed later in section 3.3.4.

The pump and probe beams are then focused onto the sample using the same lens for both beams. Focusing and overlapping the beams were achieved using a CCD video camera to image the sample. The spot overlap was optimized by maximizing the pump-probe signal at the time delay corresponding to the signal peak value. The probe spot has to be smaller than the pump spot, so that the probed area is uniformly excited. We measured a diameter of 50μm for the probe spot and of 70μm for the pump spot in most experiments.

The intensity ratio of the two beams at the sample is chosen so that the probe intensity is less than a tenth of the pump intensity. In this case, the probe pulse can be treated as a linear probe of the samples properties.

The transmitted or reflected probe intensities are recorded using a linear photodiode which is connected to a lock-in detection system. As the experiment is performed using a phase sensitive detection with single-frequency modulation, the scattered pump beam produces a time independent signal on the lock-in amplifier. This signal is reduced by

the use of a filter in front of the photodiode that absorbs the blue pump radiation. The small remaining scattered pump light is determined by blocking the probe beam before each scan.

The delay line is computer-controlled and the photo-induced changes $\Delta R(t)$ or $\Delta T(t)$, along with the dc reflectivity R, or respectively the dc transmission T, are recorded for each time delay to enable the normalization. A computer-controlled half-wave plate was introduced in to the layout in the probe beam after the delay line in order to modify the polarization for the anisotropy experiment presented in chapter 6.

The time resolution of this experiment is 140fs, measured by autocorrelation at the sample with an InGaP diode.

3.2.2 35fs Resolution Experiment

In the high-resolution experiment, we used a sub-20fs Ti:Sa laser. Special care has to be taken concerning the pulse group-velocity dispersion, and an extra-cavity chirp compensation system has to be set-up in order to maintain the original pulse duration. All the mirrors used in this experimental set-up are special broadband 45^o dielectric mirrors and the material used for optical components such as the lens, beamsplitter and window is thin fused silica.

The AOM cannot be used in this set-up, as the modulator induces too much dispersion in the pump beam. Instead, we used a mechanical chopper with a much lower frequency, 400Hz instead of 1MHz, and therefore we had to average many scans in order to get a similar signal-to-noise level.

Also, the non-degenerate configuration cannot be used, as the doubling crystal with the focusing and collimating lenses introduce too much dispersion. Therefore, in this experiment, the pump and the probe pulses have the same photon energy. In order to reduce the pump scatter, instead of using an absorbing filter in front of the detector, we

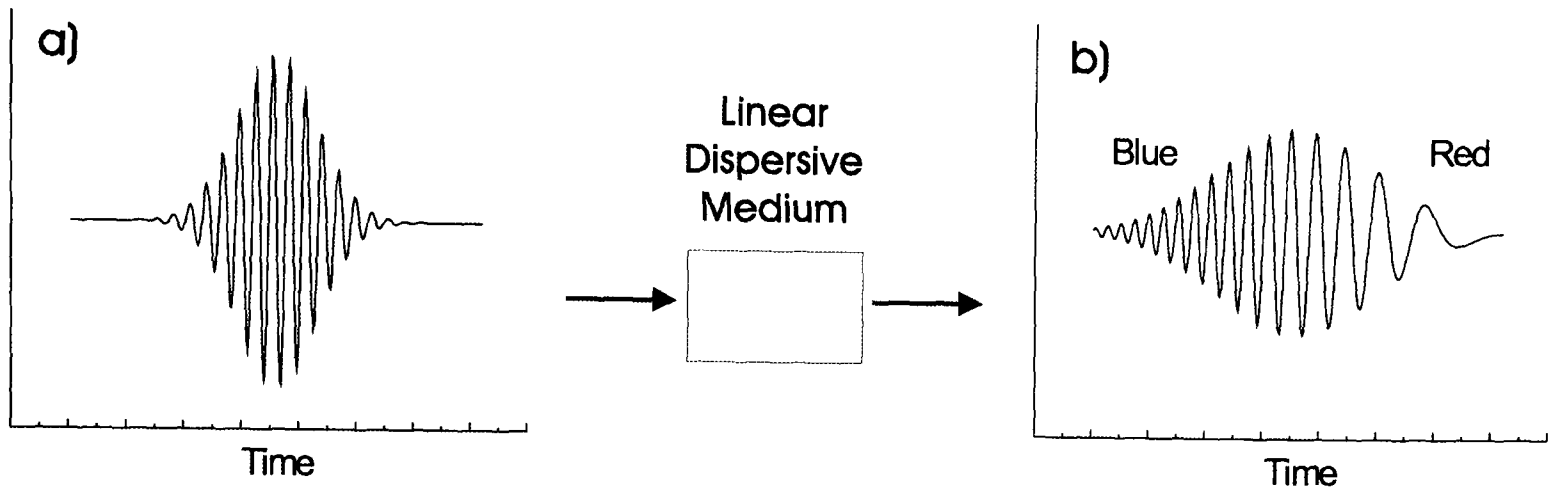

Figure 3.2: (a) Femtosecond unchirped pulse. (b) Pulse chirped by a linear medium with dispersion. The shorter wavelengths (Blue) have a larger group-velocity and therefore travels faster than the longer wavelengths (Red).

used crossed-polarized pump and probe beams and a polarizer selecting only the probe light is introduced in front of the diode.

The delay line with a resolution of 6.7fs would not be enough in this experiment and hence we replaced it for another delay line with a resolution of 0.23fs.

In spite of these precautions, the pulses at the sample are slightly chirped, i.e. the shorter wavelengths are separated from the longer wavelengths as the short wavelengths have a larger group velocity and therefore travels faster, as illustrated in Fig 3.2. It is therefore necessary to introduce an extra-cavity chirp compensation system composed of a pair of high-dispersive chirped mirrors giving a negative dispersion (cf. Fig 3.3). Usually 8 reflections from each mirror are enough to obtain unchirped pulses at the sample. The overall resolution of this experiment was measured to be 35fs.

3.2.3 White Light Probe Experiment

A high-energy pulsed laser and a white light source for the probe beam were needed for some measurements described in chapter 5. For this purpose, we used facilities at the Ultrafast Spectroscopy Laboratory of the Rutherford Appleton Laboratory. This laboratory provides 1ps pulses at 800nm with a repetition rate of 1kHz. The energy of each pulse is 800μJ, which is about 30000 times larger than the pulse energy provided by the previous systems. The laser is a regenerative amplifier from Spectra-Physics (Spitfire) pumped by a Titanium Sapphire Tsunami also from Spectra-Physics.

White light continuum pulses are generated by focusing the high-energy, 800nm pulses from the amplifier in a non-linear medium [80], in our case, glycol contained in a flowing cell. We used a set of interference filters to select the wavelength of the probe beam before the sample. The pump beam comes from the same amplifier and is frequency-doubled (400nm). The rest of the set-up is similar to the one used in the low-power excitation experiment apart from the introduction of a balanced-detection system in order to improve to signal-to-noise ratio. In time-resolved spectroscopy, a balanced-detection system consists of two probe beams, focused to two distinct spots on the sample and detected by two photodiodes. Only one of the two probed areas is photo-excited and the intensities of the probe beams are chosen so that the difference of the two signals is zero when there is no photo-excitation. In this way, the probe laser noise is compensated and hence highly reduced.

3.3 Ultrafast Lasers

Mode-locked lasers producing intense short pulses are fundamental in the study of ultrafast dynamics. They have allowed the investigation of microscopic quantum processes not previously accessible in a wide range of materials. The basic theory of mode-locking

and the propagation of mode-locked pulses through dielectric media is the subject of many books [78, 81]. This section of the thesis contains a brief description of the lasers used in the present experiments, a discussion of the methods used to characterize their output and an investigation of their noise characteristics.

3.3.1 70fs Titanium Sapphire Laser

The laser used in most experiments described in this thesis is a Spectra-Physics Tsunami, a mode-locked Titanium Sapphire (Ti:Sa) laser. The Tsunami has a pulse width of 70fs at 810nm. The mode-locked laser is optically pumped with the 5W Spectra-Physics Millenia cw laser. The Tsunami tuning range is from 720nm to 1080nm, requiring several mirror sets, and its repetition rate is 82MHz i.e. there are approximately 12ns between each pulse. The average power of the laser is about 2W at 810nm and greater than 200mW over its useful range. At 810nm, there are therefore about 10^{11} photons per pulse and the peak power for a 100fs pulse is approximately 20kW.

The mode-locking of the Tsunami is achieved by the combination of passive mode-locking, based on Kerr lensing [82] and active mode-locking with an acousto-optic modulator (AOM) driven by a signal derived from a photodiode monitoring the laser output. The positive feedback provided by the AOM encourages the mode-locking to self-start. The negative group velocity dispersion required to counteract the effects of the mirrors and the Ti:Sa crystal is provided by a four-prism compensator and a Gires-Tournois Interferometer. Using the combination of the two methods, it is possible to obtain pulse durations in the range of 70fs to 2ps.

3.3.2 20fs Titanium Sapphire Laser

The laser used in chapter 6 is a sub-20fs pulse width laser from FEMTO LASERS. The laser layout is shown in Fig 3.3 with its optical components described in Table 3.1. The

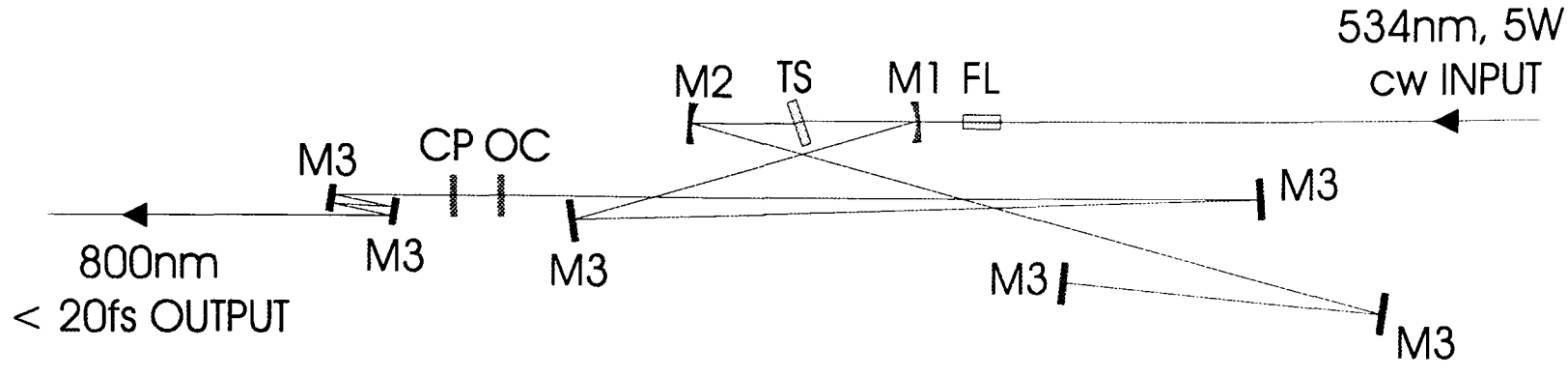

Figure 3.3: Layout of the sub-20fs Ti:Sa from FEMTO LASERS. The optical components are descibed in Table 3.1. The extracavity chirp compensation system with reflections on high-dispersive chirped mirrors is introduced after the compensation plate (CP).

laser is a self mode-locking oscillator with a thin, highly-doped Titanium Sapphire crystal described in detail in reference [83]. The layout of this laser is very simple and based on broadband chirped multilayer dielectric mirrors. The 20fs laser is pumped by the same 5W Spectra-Physics Millenia cw laser. As the pulse duration $\Delta\tau$ and the spectral width $\Delta\omega$ are related by the relation $\Delta\omega \cdot \Delta\tau \geq 1/2$, its spectral width is more than 45nm (FWHM). Its average output power is approximately 300mW with a peak power of 100kW, at a repetition rate of 75MHz.

3.3.3 Temporal Characterization of the Pulses

The temporal characteristics of the laser pulses are measured with a dispersion-minimized broadband interferometric autocorrelator [84]. An interferometric autocorrelation of a pulse from the high-resolution laser is shown in Fig 3.4a with its corresponding spectrum in Fig 3.4b. In this example, the number N of fringes above the half maximum value is 13 and the spectrum is centered at about 818nm with a spectrum width (FWHM) of 60nm. The autocorrelation has nodes in its envelope at $\pm$35fs and $\pm$70fs, which indicates that the pulse is slightly chirped. However, different configurations of the extra-cavity chirp compensation system suggest that the autocorrelation in Fig 3.4a comes from the

Abbreviation	*Description*	*Comment*
FL	Focusing lens	488 - 532nm
M1	Curved dicroic input mirror	700 - 900nm
TS	Ti:Sa crystal	p path
M2	Curved dispersive mirror	700 - 900nm
M3	high-dispersive chirped mirror	700 - 900nm
OC	Output coupler	790nm
CP	Compensation plate	790nm

Table 3.1: Optical components of the FEMTO LASERS sub-20fs Ti:Sa layout shown in Fig 3.3

best possible unchirped pulse.

In order to extract the pulse duration from the autocorrelation, assumptions are made as to the exact temporal shape of the pulses [84]. The fringes have the period of one optical cycle, which is used to calibrate the time axis of the autocorrelation. The fringe spacing in the autocorrelation is therefore given by $\Delta\tau = \lambda_0/c = 2.72$fs, where λ_0 is the centre of the spectrum and c is the light speed. The pulse duration (FWHM) is given by $\Delta t = N \cdot \Delta\tau/B$ [83], where $B = 1.897$ [84] is the deconvolution factor assuming a $sech^2$ pulse shape and $N = 13$ is the number of fringes. Consequently, we measure in this example a pulse width $\Delta t = 18.6$fs.

3.3.4 Laser Noise and Lock-In Detection

In order to improve the sensitivity of the pump-probe experiments, we investigated the intensity noise spectrum of the Tsunami and of the fast silicon avalanche photodiode (APD) used as the signal detector. Both the laser intensity noise and the APD electronic noise follow a 1/f dependence dominating at frequencies below 100kHz, plus a frequency

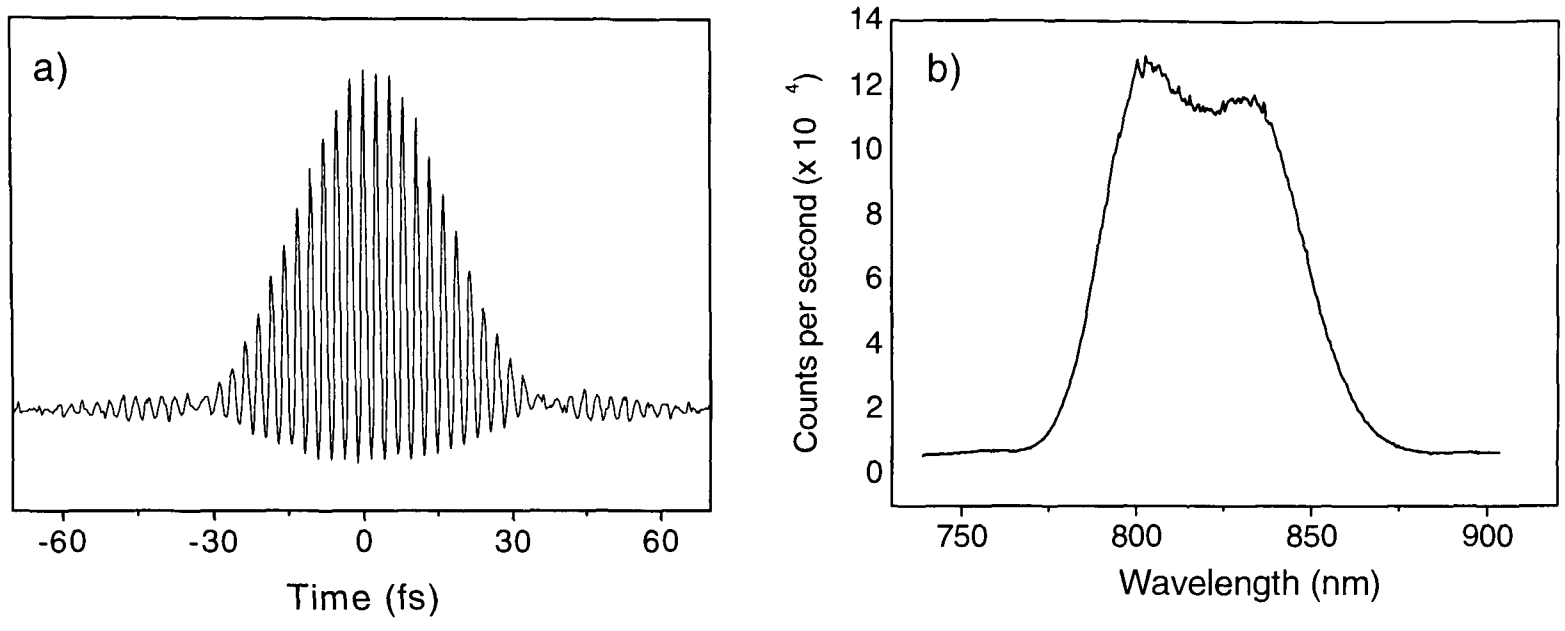

Figure 3.4: a) Interferometric autocorrelation of a 18.6fs pulse with b) its corresponding pulse spectrum.

independent component. The constant component of the laser noise is the shot noise, being the fundamental noise limit.

In order to improve the signal-to-noise ratio in pump-probe experiments, lock-in detection is often used. As the intensity noise of the laser decreases rapidly with increasing frequency, the higher the lock-in detection frequency, the better the signal-to-noise ratio of the experiment. Therefore, a system performing high-frequency lock-in detection was developed. We used a quartz acousto-optic modulator (AOM) to provide the modulated pump beam at a much higher frequency (1MHz) than with a mechanical chopper. In the AOM, the laser beam is diffracted by an ultrasonic wave leading to two output beams, the diffracted and the non-diffracted beams. By varying the amplitude of the ultrasonic wave, the amount of diffraction can be modulated. In order to obtain the best modulation depth, the diffracted beam is used as the pump. The AOM has a modulation bandwidth of 3-4MHz with almost 100% modulation depth on the diffracted beam. The angular separation of different wavelengths is negligible compared with the spot size of about 50μm.

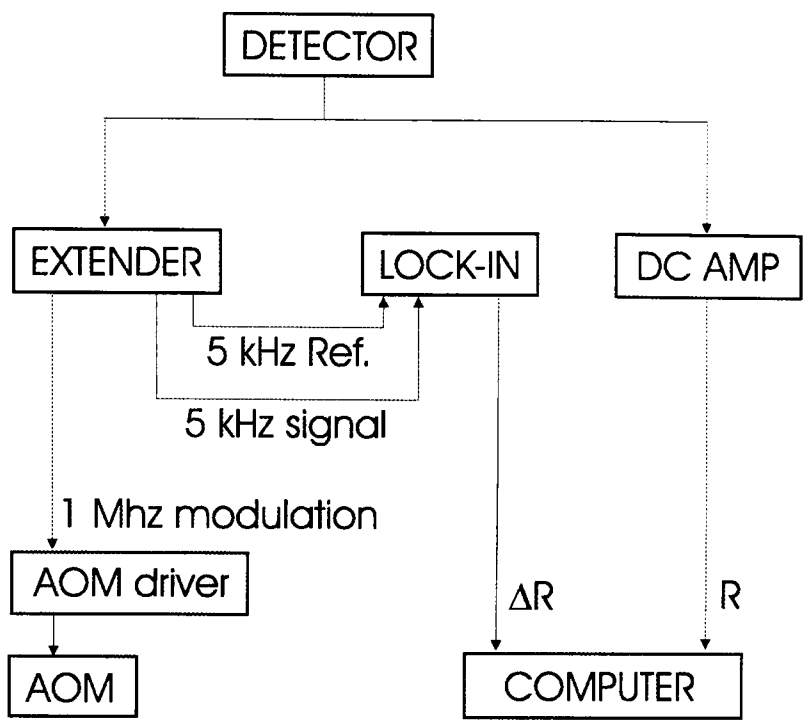

Figure 3.5: Electronic connections between the detector, the lock-in extender, the lock-in and the acousto-optic modulator (AOM).

Standard lock-in amplifiers have a frequency limit of about 100kHz and therefore, in order to be able to use a lock-in detection at higher frequencies, we used the Palo Alto Research high-frequency lock-in extender. This instrument mixes both the electrical signal which controls the AOM and the signal from the photodiode with a high-frequency internal oscillator in a double-balanced-mixer circuit to give a reference and a signal at 5kHz, which are then passed to a standard lock-in amplifier. The circuit layout with the different pieces of equipment is represented in Fig 3.5. The lock-in amplifier was set up with a time constant of 100ms, giving an equivalent noise bandwidth of 2.5Hz and was allowed to settle for two seconds between measurements.

The high-frequency lock-in detection requires linear high-speed detectors. The detector was a Hamamatsu APD module (C5460). It is a fast silicon avalanche photodiode, linear over more than four orders of magnitude of optical power and having a bandwidth of 50MHz.

The experiments were done with a modulation frequency of 1MHz in order to avoid the

low-frequency noise and the 0.6 and 1.2MHz relaxation oscillation noise peaks observed in Ti:Sa lasers. Comparisons of low- and high-frequency lock-in detection were made and the high-frequency system gave the expected decrease of over one order of magnitude in the minimum detectable pump-probe signal.

So far, we have been discussing high-frequency noise. However, there are also fluctuations of the laser intensity on a timescale of a second or more. These fluctuations cannot be removed by the lock-in detection and appear in the experiments as fluctuations of the magnitude of the signal i.e. they scale with the signal size, unlike the high-frequency noise which obscures the signal. This type of noise can be reduced by averaging experimental traces.

With this system we achieved a sensitivity in $\mathcal{R}$ of 10^{-6} for most of the experiments.

3.4 Cryogenics and Thermometry

In order to probe the superconducting phase of HTSC, it is necessary to cool samples whilst still having optical access to them. This was achieved using a helium flow exchange gas cryostat (CF1204) and a helium flow microscope cryostat (CF2102) from Oxford Instruments.

In the exchange gas cryostat, the sample is mounted in a space which contains He gas. The helium space is thermally-isolated from the surroundings by a vacuum. The outside of the helium space is cooled by liquid helium flowing through a copper tube. The He gas in the sample space conducts heat to and from the sample. The thermometer in this cryostat is a calibrated silicon diode which is thermally-contacted to the copper block on which the sample is mounted.

In the microscope cryostat, the sample is mounted in vacuum on a copper cold finger. This cold finger is attached via an indium washer to a copper block which is cooled by liquid helium and in which is embedded a heater and thermometer. In this cryostat, the

thermometer was a Rh:Fe four-point resistance thermometer.

In both cases, the temperature was controlled using a PID controller (proportional integral differential) with a resolution better than 0.5K. In order to ensure accurate measurements of sample temperature, it is important to guarantee a low-thermal resistance between the sample and the thermometer and allow a reasonable time for the system to equilibrate after any temperature changes. Good thermal contact is more difficult to achieve in the microscope cryostat, because of the lack of exchange gas, therefore particular care was taken with this cryostat to attach the sample with a good low-temperature thermal conduction (e.g. with GE varnish) and to use indium washers between the different parts of the cold finger. However, the microscope cryostat is necessary in the 35fs resolution experiment, as it contains only one thin window instead of three as in the other cryostat and hence as it reduces the pulse group velocity dispersion.

3.5 Sample Preparation and Characterization

We have studied single crystals and thin films of $Bi_2Sr_2CaCu_2O_{8+\delta}$ and $Tl_2Ba_2CuO_{6+\delta}$ in chapter 5, $YBa_2Cu_3O_{7-\delta}$ thin films in chapter 6 and $YBa_2Cu_3O_{7-\delta}$ detwinned single crystals in chapter 7. To characterize the samples, we investigated all single crystals and thin films by both resistivity and ac magnetic susceptibility measurements. The resistivity measurements were made with a standard four-point resistance technique and provide a direct measurement of the resistive-to-superconducting transition at the surface of the sample. On the other hand, the real part of the magnetic susceptibility provides a direct measurement of the Meissner effect.

We characterized some samples with X-ray diffraction and electron probe microanalysis (EPMA) to determine the sample composition and disorder. Moreover, the surface quality was checked with a polarized microscope and the optical properties of the samples were characterized at room temperature by measuring the transmission and reflection

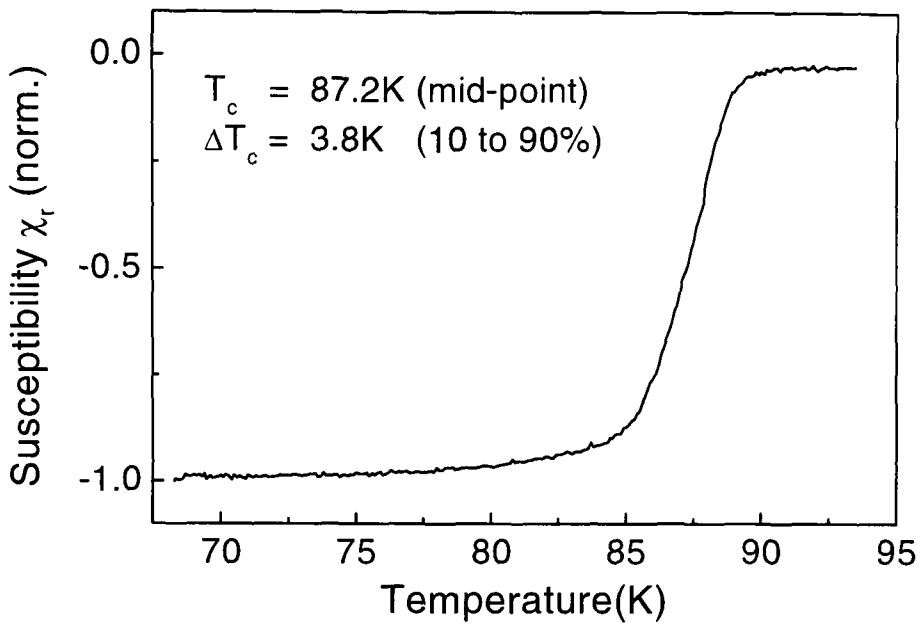

Figure 3.6: Real part of the magnetic ac susceptibility χ of slightly overdoped $Bi_2Sr_2CaCu_2O_{8+\delta}$ single crystal. The transition is centered at 87.2K and has a width of 3.8K.

spectra using a Perkin Elmer spectrophotometer. The results of these latter measurements are in agreement with the published spectra [19, 82].

To ensure the samples did not degrade, they were stored in a dry atmosphere in a desiccator as HTSC react with atmospheric moisture. Each sample was cut into several pieces and fresh pieces of the sample were used for each experiment since some degradation of the sample surface was observed.

3.5.1 BSCCO Single Crystals

We have measured a range of $Bi_2Sr_2CaCu_2O_{8+\delta}$ (BSCCO-2212) single crystals from two different sources: from the School of Metallurgy and Materials, University of Birmingham by J.S. Abell and from the Clarendon Laboratory, University of Oxford by C. Chen. All samples were flux-grown and slightly overdoped with critical temperatures T_c between 80.6K and 87.2K and transition widths ΔT_c of 0.5 to 4K. The samples were grown using a large temperature gradient technique (about $10^oC/cm$), achieved by placing the crucibles

close against the hot side of the furnace. The starting composition was $Bi_{2.4}Sr_2CaCu_2O_8$, and the final composition was $Bi_{2.07}Sr_{1.74}Ca_{0.92}Cu_2O_{8+\delta}$ as determined by EPMA. The critical temperature of the optimally-doped material was 90K. The material was annealed either in air or in atmospheric pressure O_2, giving critical temperatures of 85.7 and 83.5K respectively in the weak overdoped regime. 5% and 10% Pb-doped BSCCO single crystals were also investigated, with critical temperatures of 82.8K and 80.6K respectively, again in the overdoped regime. Fig 3.6 presents the ac susceptibility measurement of a slightly overdoped BSCCO-2212 single crystal with a transition centered at 87.2K and a transition width of 3.8K.

3.5.2 BSCCO and TBCO Thin Films

We measured the ultrafast response of $Bi_2Sr_2CaCu_2O_{8+\delta}$ (BSCCO-2212) and $Tl_2Ba_2CuO_{6+\delta}$ (TBCO-2201) thin films from the Department of Chemistry, State University of New York, Buffalo by Z.F. Ren and J.H. Wang.

The BSCCO-2212 samples were slightly underdoped films grown by rf magnetron sputtering with critical temperatures T_c between 70 and 80K and transition widths ΔT_c of about 7K. The thin films were grown on $LaAlO_3$ and were 300 to 400nm thick.

We have also investigated state-of-the-art TBCO-2201 thin films also grown by rf magnetron sputtering on $SrTiO_3$. These samples are close to being optimally-doped with a transition temperature of about 82K and a transition width of 8K. The advantage of the $Tl_2Ba_2CuO_{6+\delta}$ material is that the full doping dependence, from highly underdoped to highly overdoped, can be obtained simply by varying the oxygen concentration δ i.e. without the need of chemical substitutions.

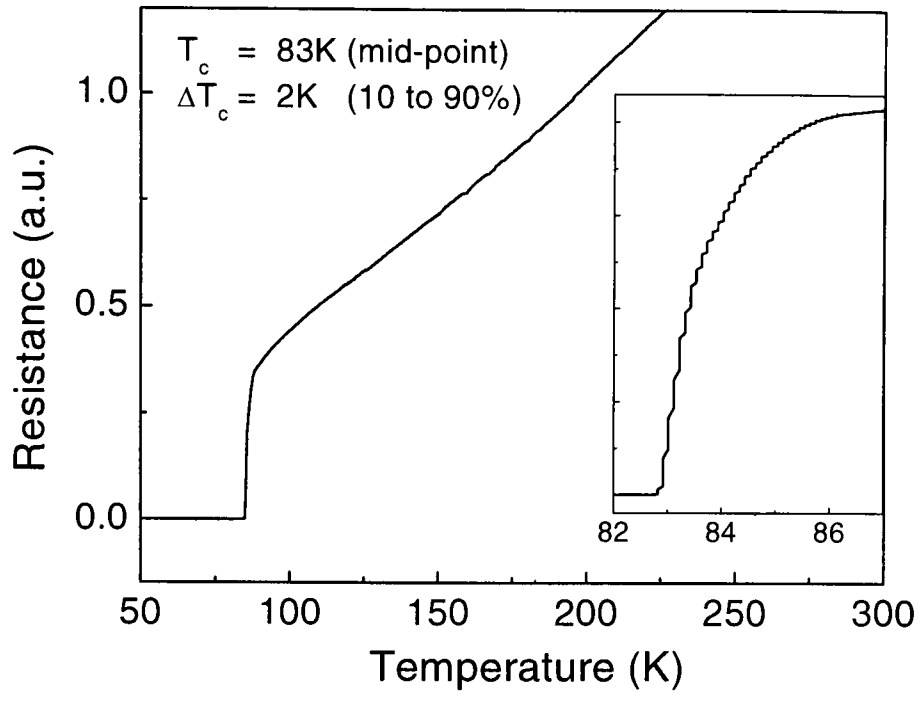

Figure 3.7: Four-points resistivity measurement of optimally-doped $YBa_2Cu_3O_{7-\delta}$ thin film. The transition is centered at 83K with a transition width of 2K.

3.5.3 YBCO Thin Films

The $YBa_2Cu_3O_{7-\delta}$ thin films used in chapter 6 are commercially-grown samples from THEVA, Germany. There are optimally-doped 200nm thick films grown by magnetron sputtering on MgO and $SrTiO_3$ substrates. The four-point resistivity measurements in Fig 3.7 presents a critical temperature of 83K, less than the optimal value due to strains inferred from the thin film substrate.

3.5.4 YBCO Single Crystals

The $YBa_2Cu_3O_{7-\delta}$ samples used in chapter 7 for the anisotropy measurements were single crystals produced by flux growth by C. Chen in the Clarendon Laboratory, University of Oxford. They have transition temperatures around 92.5K with a transition width less than 0.2K, after being annealed in an oxygen atmosphere.

The single crystals and thin films exhibit twinned microstructures with two perpen-

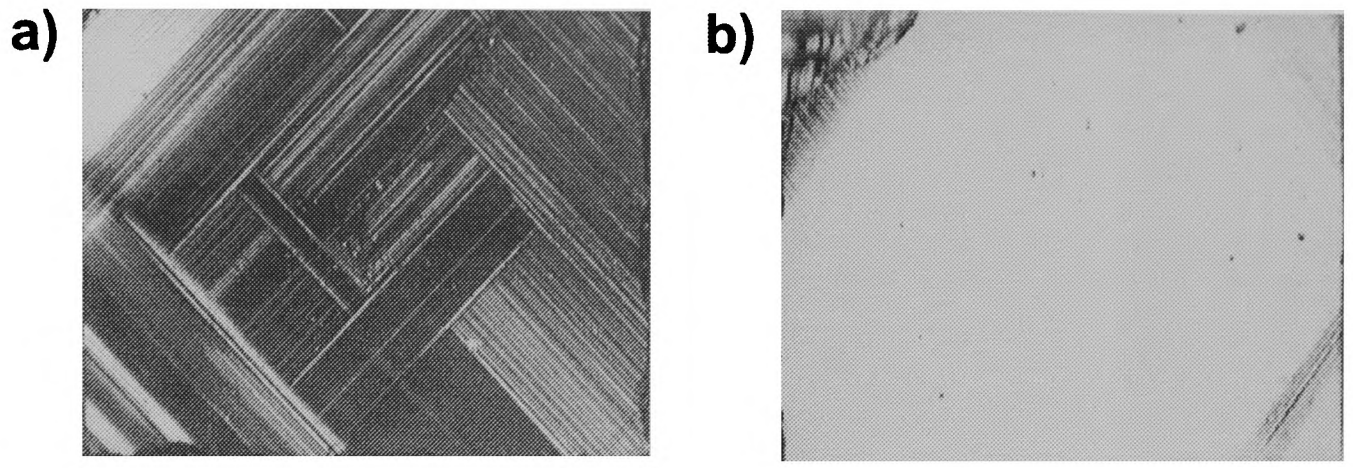

Figure 3.8: Image of YBCO single crystal surfaces with a polarized microscope, (a) before detwinning and (b) after detwinning.

dicular twin domain systems. In other words, in some areas of the sample, the unit cells have their a-axis along one direction and in other areas, the unit cells have their a-axis perpendicular to this direction [85, 86]. A model for the twin domains has been developed by Chen et al. [86], concluding that the average area of one twin domain is 18 cells i.e. 2.7nm^2.

It is possible to detwin YBCO single crystals and hence to have all the unit cells with their a-axis parallel to each other [87]. The crystals were detwinned by applying a uniaxial stress of about 10MPa in the a-b plane along one of the crystal axes at 350°C in flowing oxygen at 1Bar. The amount of stress required for full detwinning varies as a function of the crystal quality with less strain and lower temperature being indicative of a lower defect density. After dewinning, the b-axis is aligned throughout the entire crystal perpendicular to the direction of the applied stress, as the lattice parameter a is smaller than b. The critical temperature before detwinning was about 92.5K, but there is evidence that the crystals become slightly underdoped after detwinning due to oxygen depletion. A twinned crystal exhibits patterns in a polarized microscope image as represented in Fig 3.8, allowing the detwinning process to be monitored.

Chapter 4

Previous Ultrafast Studies of HTSC

In this chapter we present an overview of the previous time-resolved pump-probe experiments on high-temperature superconductors (HTSC). The experimental apparatus used in the following sections is basically similar to the standard pump-probe set-up presented in section 3.2.1. We first focus on thermo-modulation experiments performed on metals at room temperature and at high photo-excitation energy to introduce the concepts of thermalization, Fermi surface smearing and the Allen theory [88] of carrier relaxation processes in metals. Next, we present a review of experiments on the most-studied HTSC, $YBa_2Cu_3O_{7-\delta}$ (YBCO). After an overview of the work published prior to this thesis on other HTSC, mainly on bismuth and thallium-based compounds, we introduce basic concepts of coherent phonon oscillations observed in YBCO. In the next section, we present the Kabanov model [53], a theoretical model of the photo-induced reflectivity and transmission of materials with a small energy gap in the excitation spectrum. The YBCO data from the underdoped to the overdoped regime are in good agreement with the predicted temperature dependence of the initial transient magnitude and of the relaxation rate. Finally, we introduce the two main theories on the long-lived signal observed on the nanosecond timescale in HTSC.

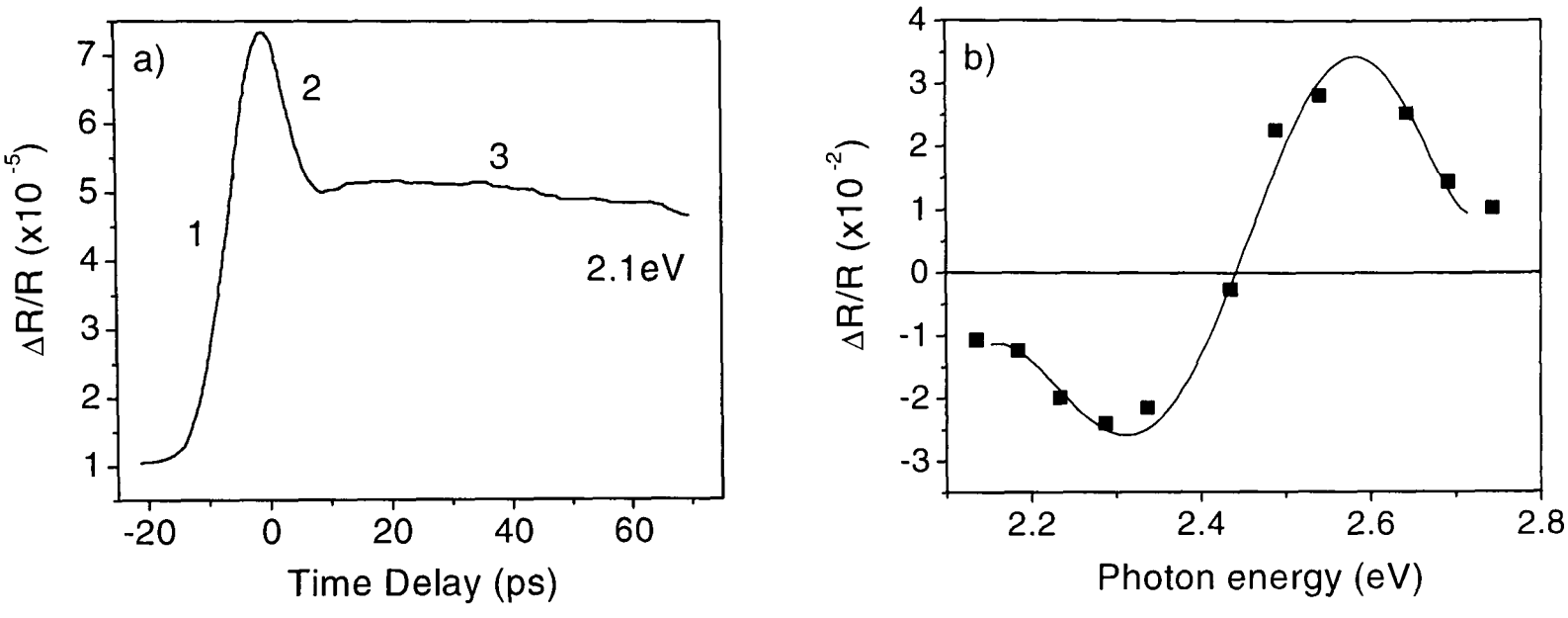

Figure 4.1: (a) Photo-induced reflectivity of copper measured by Eesley et al. [89] at 2.1eV and (b) magnitude of the photo-induced reflectivity of gold at 0.2ps as a function of the probe energy measured by Schoenlein et al. [90] (the solid line is a guide to the eyes).

4.1 Ultrafast Experiments on Metals

In order to better understand experiments on HTSC, it is necessary to present the basic concepts of the ultrafast spectroscopy on metals. The first picosecond thermo-modulation experiment was performed on copper at room temperature by Eesley [89] in 1983. The probe beam was from a dye laser which could be tuned between 2.03 and 2.17eV (610-572nm) and the samples were excited at 1.92eV (645nm) with a high photon density (about 30 times larger than in our experiment). He observed a fast, resolution-limited initial transient, as illustrated in Fig 4.1a for 2.1eV. Schoenlein et al. [90] performed similar measurements on gold and measured the probe energy dispersion of the peak magnitude, shown in Fig 4.1b with derivative-like feature centered at 2.45eV.

The change in temperature induced by electrons excited by the pump beam modifies the reflectivity of the metal in several ways. First, a higher electronic temperature can cause a change in the occupation of the states near the Fermi energy (*Fermi surface*

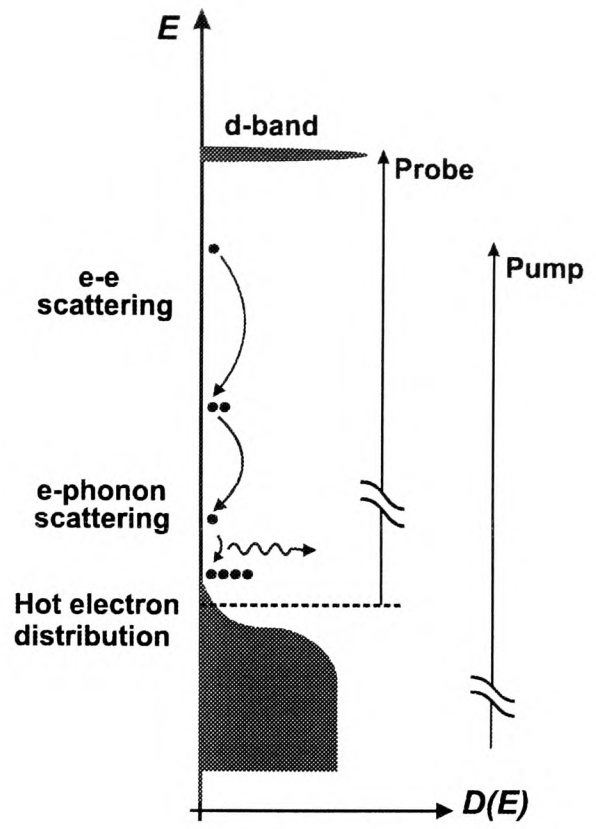

Figure 4.2: Pump-probe mechanism in a metal: photoexcitation from occupied to unoccupied electronic states, thermalization with e-e and e-ph scattering, Fermi surface smearing and modification of the absorption transitions (and thus the reflectivity) from states near E_F to a narrow d-band.

smearing), blocking some states and opening other states for optical transitions. A resulting change in absorption can be probed in transmission and reflectivity and usually occurs on the femtosecond timescale. Second, photo-excited electrons can cause strains in the sample due to thermal expansion. Optical transitions are modified as the band structure is determined by the lattice. This lattice effect depends on the phonon escape time out of the probed area, which is typically more than 10ps.

In femtosecond experiments on metals with d-band, the Fermi surface smearing effect is the most often considered effect because of its sub-picosecond transient changes and because of the presence of narrow d-bands. In Fig 4.2 is illustrated the high-intensity pump pulse exciting electrons from occupied to unoccupied states. This process is followed by an initial electron-electron thermalization estimated to be very short, several femtoseconds [25], and thus negligible with respect to the pulse duration ($\sim$ 100fs). As

the thermalization time τ_{e-e} is much faster than the electron-phonon relaxation time τ_{e-ph}, electrons are decoupled from the lattice and the system can be described with an electronic temperature T_e and a lattice temperature T_L. Because the electronic heat capacity is much smaller that the lattice heat capacity, T_e can be much higher the T_L. If the final states of the probe optical transition are located in a dispersionless narrow d-bands and if the initial states are near the Fermi energy, the probe transitions can be affected by the non-equilibrium electronic distribution at the Fermi energy i.e. by the Fermi surface smearing. Therefore, the amplitude and the sign of the change in reflectivity $\mathcal{R} = \Delta R/R$ strongly depends on the wavelength of the probe beam and the peak magnitude has a derivative-like feature, as observed for copper in Fig 4.1b.

Consequently, Fig 4.1a can be understood as the following in the Fermi surface smearing picture. Phase 1 in the figure corresponds to the thermalization for the hot electron, however the rise time is actually often limited by the pulse width. Phase 2 corresponds to the cooling of the non-equilibrium distribution and phase 3 is attributed to lattice effects with typical timescales being determined by heat diffusion.

The relaxation time of the photo-excited electronic system, i.e. the cooling which takes place in phase 2, can give important information about the sample. Two effects should be considered: the energy relaxation, i.e. electron-phonon scattering and scattering with other excitations (e.g. plasmons or spin waves), and secondly, the transport of energy out of the probed volume. Brorson et al. [91] proved experimentally that decreasing the thickness of the film in metal thin films reduces the transport of energy perpendicular to the surface of the film. They demonstrated that this transport can be neglected if the film thickness is on the order of the optical skin depth.

4.2 Allen Theory and the Electron-Phonon Coupling

Allen [88] investigated theoretically the energy relaxation of high-energy electrons through electron-phonon scattering, taking into account electron-electron and phonon-phonon scattering for thermalization. He calculated that, in metals, when electrons are heated with a laser pulse to a temperature T_e greater than the lattice temperature T_L, the electronic temperature follows

$$\partial T_e/\partial t = \gamma_T(T_L - T_e) \tag{4.1}$$

due to the electron-phonon interaction, with the thermal relaxation rate

$$\gamma_T = 3\hbar\lambda\langle\omega^2\rangle/\pi k_B T_e \tag{4.2}$$

In this expression, $\lambda\langle\omega^2\rangle$ is an important parameter in the conventional theory of superconductivity, as

$$\lambda\langle\omega^2\rangle = \sum_a \eta_a/M_a \tag{4.3}$$

where the sum is over atoms a of mass M_a in the unit cell and η_a is a Fermi surface average scattering per unit of displacement, has made possible many microscopic calculations. λ is the electron-phonon coupling constant and $\langle\omega^2\rangle$ is the second moment of the phonon spectrum. The model predicts therefore that the thermal relaxation of electrons in metals is determined by the electron-phonon coupling constant λ.

Assuming that the photo-induced reflectivity is proportional to the difference of the electronic and lattice temperature, i.e. $\mathcal{R}(t) \propto (T_e - T_L)$, Allen was able to extract the mean electron-phonon coupling constant λ from the dynamics of gold, copper and tungsten. He obtained values in good agreement with values obtained from resistivity [92] and neutron scattering [93] measurements. Several measurements of λ [94, 95] in conventional superconductors were also in good agreement with the Allen formula.

No other experiment is known which directly probes $\lambda\langle\omega^2\rangle$, and few experiments separate λ from other effects. Moreover, whilst the coupling constants λ extracted from resistivity [92] and neutron scattering [93] data are related to the momentum relaxation, the coupling constants λ extracted from the Allen formula is related to the energy relaxation. The BCS theory also refers to the coupling constant λ related to the energy relaxation, which makes the ultrafast dynamics measurements especially important to determine this constant.

4.3 Previous Experiments on $YBa_2Cu_3O_{7-\delta}$ (YBCO)

Three important femtosecond experiments on HTSC were published in 1990. They were degenerate pump-probe spectroscopy experiments on c-axis thin films[1] using a CPM[2] dye laser at 630nm (1.98eV). Brorson et al. [96] performed reflection and transmission measurements at room temperature to investigate the normal state dynamics with an absorbed photon density on the order of 10^{-3} per unit cell ($20\mu Jcm^{-2}$). For optimally-doped YBCO with $T_c = 90K$, they observed a photo-induced *increase* of the reflectivity and *decrease* of the transmission, with a resolution-limited initial transient and a decay to a long-lived signal after about 300fs, as shown in Fig 4.3. In contrast, insulating YBCO exhibited a *decrease* in reflectivity and an *increase* in transmission with a 1ps decay time to a level close to zero. Brorson et al. applied the Allen formula [88] to extract the electron-phonon coupling constant and obtained $\lambda \cong 1$.

Chwalek et al. [97] measured the temperature dependence of photo-induced transmission of YBCO ($T_c = 83K$) from 7K to room temperature. The absorbed photon density was also on the order of 10^{-3} per unit cell. Their room temperature results were in agreement with those observed by Brorson et al. The temperature dependence of the

[1] A c-axis thin film is defined with the c-axis normal to the film surface.

[2] Colliding Pulse Mode: laser with a passive mode-locking in a saturating absorber and with intra-cavity dispersion compensation.

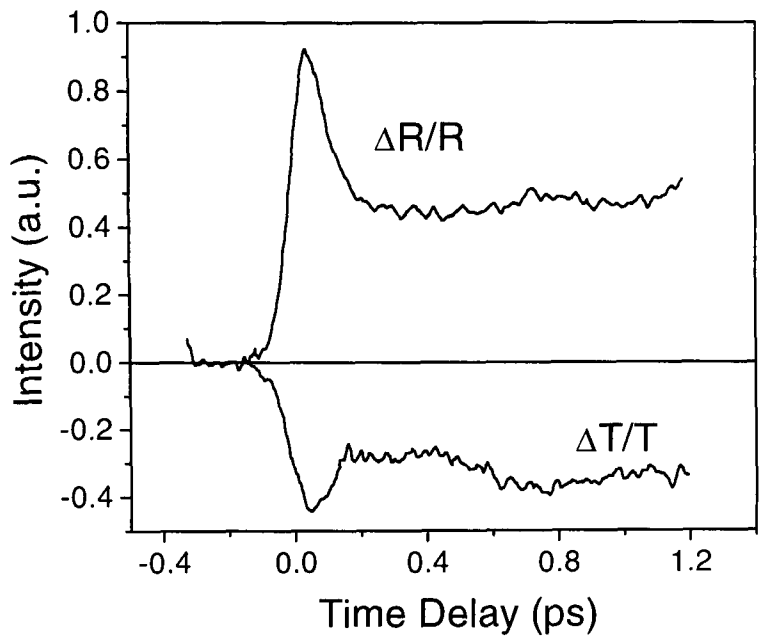

Figure 4.3: Photo-induced reflectivity and transmission of optimally-doped YBCO at room temperature by Brorson et al. [96].

peak value of $\mathcal{T}$ exhibits a change of magnitude at T_c, as shown in Fig 4.4. They reported an increase in magnitude by a factor of two from above T_c to below T_c.

The third experiment was performed by Han et al. [98]. They measured the photo-induced reflectivity of optimally-doped YBCO with $T_c = 90K$ from 10K to room temperature, with an estimated absorbed photon density of $2{\cdot}10^{-3}$ per unit cell ($40\mu Jcm^{-2}$), slightly higher than in the experiment performed by Chwalek et al. The results were again in agreement with those of Brorson et al. for the sign of $\mathcal{R}$ and the long-lived signal, however they did not observe a fast transient in the normal state. For temperatures below T_c, they observed a fast *negative* transient which decays to a long-lived positive signal. The temperature dependence of the peak amplitude below T_c is shown in Fig 4.5. The data are best fitted (solid line in Fig 4.5) by the two-fluid model [15] for the relative density of Cooper pairs. A fit to the data using the BCS model in the weak-coupling limit [99], with the superconducting pair density obtained from measurements of the penetration depth, was not as good as the two-fluid model and therefore the signal was associated with quasiparticles generated by breaking of Cooper pairs following

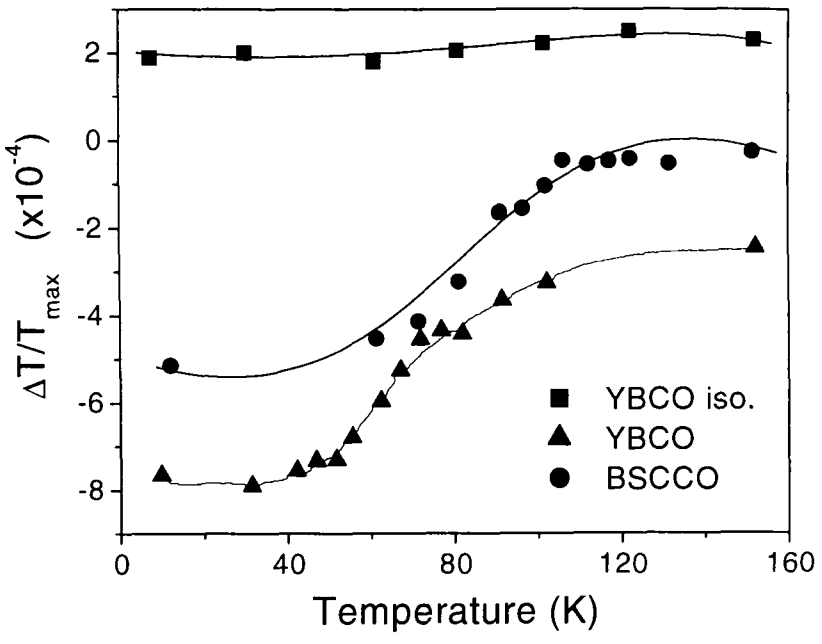

Figure 4.4: Temperature dependence of peak magnitude of the photo-induced transmission reported by Chwalek et al. [97] for insulating YBCO, superconducting YBCO and superconducting BSCCO. The solid lines are guides to the eyes.

photo-excitation.

The fast transient in the superconducting phase was interpreted in terms of Fermi surface smearing of an interband transition by Eesley [100] and Chwalek et al. [97] in a similar manner as in metals, but with the presence of a superconducting gap. However, Han et al. [98] explained the fast transient in terms of a modification of the Drude reflectivity. An increase in the normal carrier density Δn due to the breaking of Cooper pairs by the photo-excited carriers leads to an increase in the plasma frequency $\omega_p^2 = 4\pi ne^2/m$ in the Drude model. Secondly, an increase of the plasma frequency ω_p has the effect of increasing the Drude part of the reflectivity. Both probe mechanisms, Fermi surface smearing and Drude reflectivity, assume that the number of broken pairs are much larger than the number of photo-excited carriers, i.e. that most of the excess energy with which the carriers are excited goes into pair breaking. This process called *avalanche multiplication* consists of electron-electron scattering and electron-phonon scattering.

Han et al. attributed the decay of the fast transient to the loss of energy from

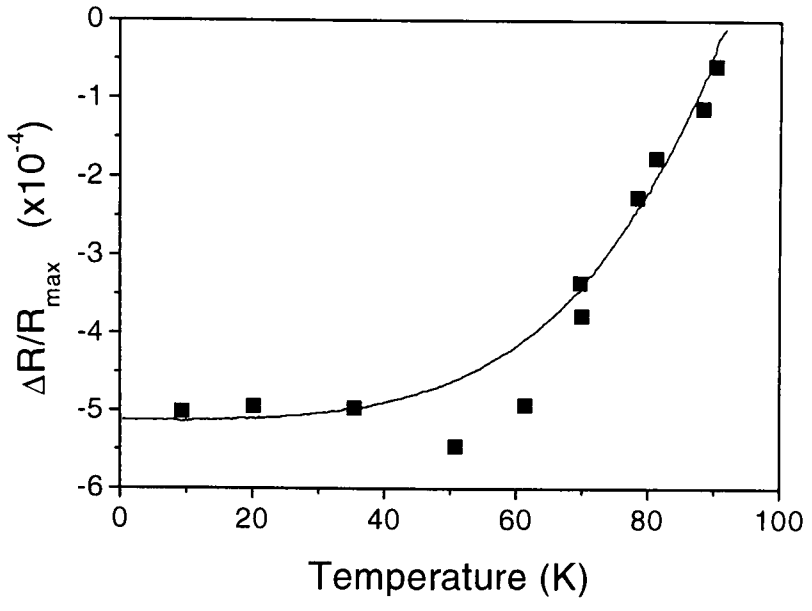

Figure 4.5: Temperature dependence of the photo-induced reflectivity of superconducting YBCO reported by Han et al. [98]. The solid line is from a two-fluid model [15] of the relative density of Cooper pairs.

high-energy phonons following the Rothwarf-Taylor equations [101] applied to BCS superconductors.

In all of these experiments, the long-lived signal observed after the initial transient was attributed to a bolometric response, i.e. to lattice heating and cooling described by the heat-conduction equations [102]. Eesley [89] estimated the lattice temperature increase is not more than 1K in metals.

Similar degenerate pump-probe experiments in reflection at 2eV were made on $Y_{1-x}Pr_xBa_2Cu_3O_{7-\delta}$ thin films by Kazeroonian et al. [103] at room temperature. Doping YBCO with Pr lowers T_c, probably by removing holes from the CuO_2 planes, but the effect is still not fully understood [104]. They showed that increasing the Pr content x moves E_F upward and therefore a fixed 2eV probe pulse can access to optical transitions slightly below ($x = 0.0$), very near ($x = 0.1$) or slightly above ($x = 0.25$) the Fermi level. They observed a change of sign of $\mathcal{R}$ from negative to positive, as the doping level was decreased through $x = 0.1$ ($T_c = 80K$). Kazeroonian et al. interpreted their results using the Fermi surface smearing model, the sign change being due to the shift of the Fermi

energy with x through the energy being probed at 2eV. Reitze et al. [105] extended their measurements to a temperature dependence down to 4K. They observed the same change of sign as a function of doping, with another change of sign for the Pr content $x = 0$ as a function of temperature at T_c.

The next group of experiments used a continuum light for the probe beam. Chekalin et al. [106] measured at 70 and 92K the photo-induced reflectivity and transmission spectrum from 1.89 to 2.02eV of YBCO thin film with $T_c = 80$K, with a pump beam energy of 2.03eV. The pump power was much higher in these experiments than in the previous ones [96, 97, 98, 103, 105], with an absorbed photon density of 0.78 photon per unit cell (energy density of 15mJcm^{-2}), which corresponds to an excitation density 1000 times more intense than in our experiments and 10 times more intense than the threshold for a complete closure of the gap observed in BSCCO [10]. The spectrum of the imaginary part ε_2 of the dielectric constant extracted from the data was interpreted as being due to the Fermi surface smearing of an interband absorption with initial and final states at the Fermi energy, as they observed a derivative-like feature centered around 2.05eV similar to the one observed in metals. They also observed an extra absorption band centered at 1.96eV, which they attributed to the a change in the single-particle DOS due to the closure of the superconducting gap. However, the magnitude of the induced signal was $\gtrsim 10^{-2}$, due to the much higher excitation density, which could affect the results compared to the low-excitation experiments. The high-excitation density may also lead to a degradation of the sample. Other continuum probe experiments have been reported by Lozovik et al. [107]. They used a YBCO thin film with $T_c = 89$K and an even higher excitation density, 2.5 higher than the one used by Chekalin et al. The results did not show the same spectral dependence of ε_2, although they suggested that the difference might be due to the doping level leading to a shift in the Fermi energy. Although both experiments suggested a probe mechanism involving interband transitions

associated with the Fermi energy, these experiments have to be treated with caution. as they are far from the weak perturbation limit.

Feenstra et al. [52] present a non-equilibrium study of superconductivity in $DyBa_2Cu_3O_{7-\delta}$ thin film using photo-induced mm-wave absorption. The time evolution of the transmission is monitored at $5cm^{-1}$ subject to far-infrared pulses tunable from 100 to $2000cm^{-1}$. They observed a bolometric signal and a fast non-equilibrium signal with a decay on the order of several microseconds i.e. much longer than the decay observed in the others experiments. They interpreted the long decay as pair re-formation with a strong enhancement due to the unusual properties of quasiparticles residing near the nodes of a predominantly d-wave superconductors. They argued that the pair re-formation processes in a d-wave superconductor are very different from those in s-wave. While the quasiparticles are cooling down to an energy of the order of k_BT, the excess quasiparticles relax toward the nodes. After this relaxation is completed, pair re-formation processes will only generate phonons with an energy of the order of k_BT and a momentum of order of $\hbar q_{ph} \approx k_BT/\upsilon_s$ where υ_s is the sound velocity. As $T << k_B\upsilon_s$ it follows that $q_{ph} << k_F$ and hence most recombination processes will involve two quasiparticles in nodes at opposite sides of the Fermi surface. Moreover, the coherence factor is proportional to Δ_k/k_BT becoming therefore zero at the nodes. Consequently, the quasiparticles relax to regions in k-space with a strongly-reduced pairing amplitude, explaining the strong enhancement of the decay time.

In addition to the pump-probe experiments described above, ultrafast dynamics in YBCO has been investigated by measuring the photo-response of current-biased bridge structures of YBCO. Hegmann et al. [108] observed a fast and a slow component in the voltage response below T_c using 100ps, 532nm laser pulses. The amplitude of the slow component was interpreted as a resistive bolometric response, where the laser pulse heats the bridge into the superconducting transition region. The resolution-limited transient

was interpreted as a change in the kinetic inductance of the bridge due to temperature-induced changes in the superconducting state. Since a change in the kinetic inductance corresponds to a change in the superconducting carrier density, this experiment proves that laser pulses actually modulate the Cooper pair density.

Williams et al. [109] measured the photo-response using 100fs, 390nm laser pulses. Above T_c, the physical origin of the fast component was attributed to non-equilibrium electron heating, in which only electron states are perturbed by the laser pulse, while the phonons remain in thermal equilibrium. Below T_c pair breaking followed by quasiparticle recombination leads to rapid changes of the superfluid density, which in the presence of a bias current gives rise to a transient due to the kinetic inductance modulation. This interpretation is therefore not bolometric in nature, contrary to the conclusion of Hegmann et al. From the observed electrical transients, Williams et al. were able to extract the electron thermalization time constant, 560fs, and the mean electron-phonon relaxation time constant, 1.1ps.

4.4 Previous Experiments on Bismuth- and Thallium-based compounds

YBCO and its related compounds like $Y_{1-x}Pr_xBa_2Cu_3O_{7-\delta}$ have received by far the most attention in ultrafast experiment until now. Only a few studies of other materials have been made so far. Eesley et al. [9] investigated $Tl_2Ba_2Ca_2Cu_3O_{10}$ (TBCO-2223) which has three CuO_2 planes separated by TlO planes and chains. The experiment measured degenerate pump-probe reflection at 2eV. The results showed a negative transient, which decays with a time constant of 0.5ps above T_c and a positive transient below T_c, which decay in about 2ps. They observed the relaxation time to diverge[3] at T_c, which has

[3]The temperature dependence of the relaxation time has a similar form as in YBCO (see Fig 4.9 in section 4.2) with a divergence at T_c.

subsequently been called into question. Indeed, Han et al. [110, 111] argued that the form of the divergence at T_c is highly dependent on the sample quality, and more specifically on the inhomogeneities of the sample, and on the excitation intensity.

The Bi-based superconductors $Bi_2Sr_2CaCu_2O_8$ (BSCCO-2212) and $Bi_2Sr_2Ca_2Cu_3O_{10}$ (BSCCO-2223) have been investigated by Brorson et al. [96], Chwalek et al. [97] and Thomas et al. [8], but very little systematic work has been done so far. Brorson et al. [96] performed room temperature measurements of both $\mathcal{R}$ and $\mathcal{T}$ on optimally-doped BSCCO-2212 and BSCCO-2223 thin films with a low photon density on the order $5{\cdot}10^{-4}$ per unit cell ($\sim 10\mu Jcm^{-2}$). They reported a positive $\mathcal{R}$ and a negative $\mathcal{T}$ for BSCCO-2212 and the opposite for BSCCO-2223. At the same excitation density, Chwalek et al. [97] measured the temperature dependence of the induced transmission $\mathcal{T}$ on optimally-doped BSCCO-2223 ($T_c = 100K$) thin films. The temperature dependence of the negative peak value is shown in Fig 4.4. The broad $\mathcal{T}$ transition at T_c can be explained by the poor quality of their BSCCO-2223 samples, as they reported a broad superconducting transition and the presence of intergrowth BSCCO-2212 phase within their films. Thomas et al. [8] measured the doping dependence of the photo-induced transmission of Y-doped $Bi_2Sr_2Ca_{1-y}Y_yCu_2O_8$ at room temperature. They reported a negative $\mathcal{T}$ for $y < 0.4$ i.e. for the superconducting materials and a positive $\mathcal{T}$ for $y > 0.4$ i.e. for the insulating materials. However, they used a very high-excitation density enabling photo-induced transmission $\mathcal{T}$ as high as $3{\cdot}10^{-2}$ and thus this experiment is not in the same perturbation limit as the previous experiments on BSCCO [96, 97].

4.5 Coherent Phonon Oscillations in YBCO

An oscillatory component in the photo-induced reflection transient was first observed in insulating YBCO [112] and was interpreted as coming from the generation of coherent

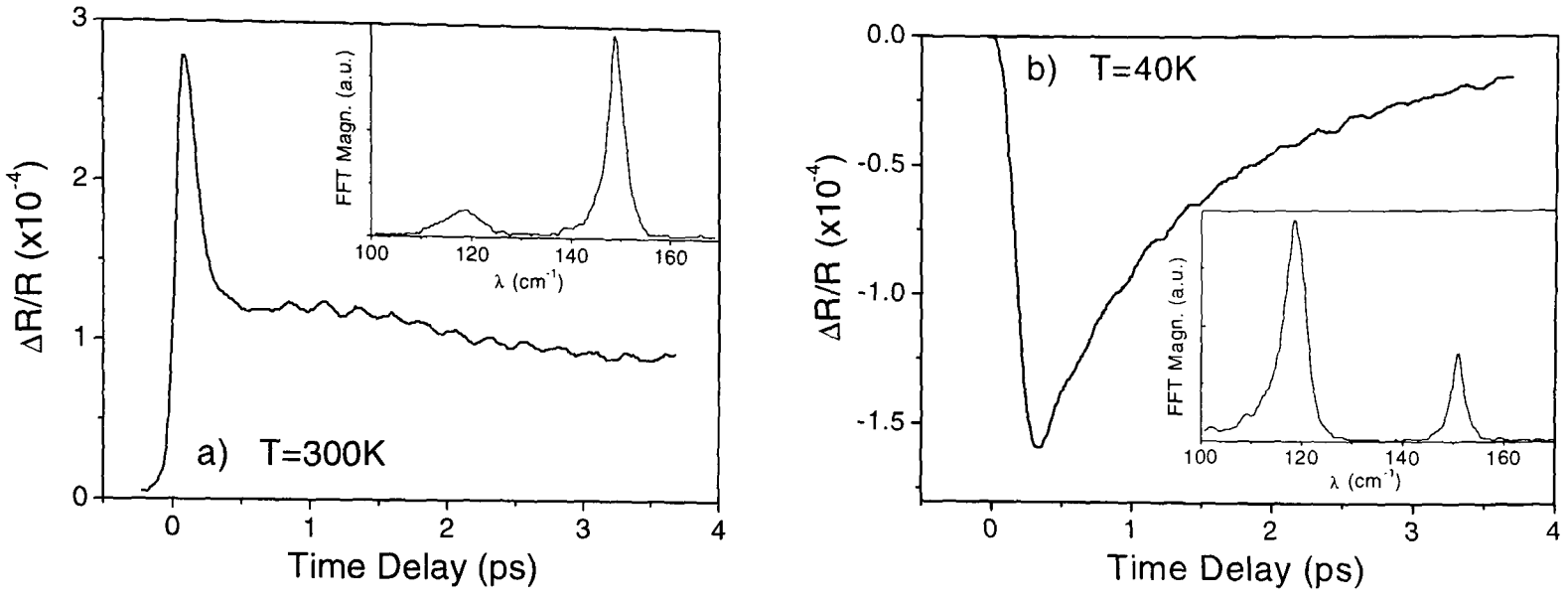

Figure 4.6: Photo-induced reflectivity of optimally-doped YBCO thin film at (a) 300K and (b) 40K measured by Albrecht et al. [113]. Insets show the Fourier transform of the phonon modulation.

phonons. A period of 237fs was measured, which corresponds to a Raman active phonon mode at $142cm^{-1}$. Albrecht et al. [113] reported a degenerate pump-probe reflection experiment at 2eV with an excitation density of $15\mu Jcm^{-2}$ on optimally-doped YBCO thin films with T_c = 89-92K. The results show the same dynamics above and below T_c as in the previous experiments, as illustrated in Fig 4.6, but with clear oscillations superimposed. The Fourier transform of the oscillations shows two clear peaks at $120cm^{-1}$ and $150cm^{-1}$ which correspond to two of the A-symmetry YBCO phonons. The magnitude of the $120cm^{-1}$ response shows a temperature dependence similar to a weak-coupling BCS superconducting gap, whereas the magnitude of the $150cm^{-1}$ phonon increases at T_c. The dephasing time of the two oscillation modes increases linearly with decreasing temperature but with a much greater gradient below T_c. This effect was interpreted as being due to the decrease in electronic scattering of the phonons as the superconducting gap opened.

Mazin et al. [13] attributed the oscillatory signal to the displacive excitation of coherent phonons (DECP). The DECP model was used previously to describe the oscil-

latory component in semiconductors and semimetals [114, 115], where again A-symmetry Raman-active "breathing modes" were observed.

Albrecht et al. interpreted the non-oscillatory part of the signal as being due to either Fermi surface smearing or a shift of the plasma frequency as proposed first by Han et al. [98]. However, Mazin et al. [13] proposed that the entire $\mathcal{R}$ response in HTSC is due to distortions of the lattice induced by the pump pulse leading to a modification of the refractive index as in Raman scattering. Above T_c, the lattice distortions would be due to excitations of electrons into higher-lying anti-bonding orbitals. Below T_c, the distortion would be due to the breaking of Cooper pairs. The amplitude of the distortion below T_c would be determined by a balance between an increase in strain energy and a decrease in electronic energy. The greater the pairing energy, which is proportional to the number of pairs, the larger the lattice distortion. In other words, in this model the microscopic mechanism for the excitation is that superconductivity induces small displacements in the equilibrium position of the ions, since the pairing energy depends on the density of states at the Fermi energy changing with the ionic positions. When superconductivity is modulated by a laser pulse, the ions are pulled back towards their normal equilibrium positions, exciting coherent phonons. The non-oscillatory part of the signal corresponds to the adiabatic response of the lattice and follows the number of excited electrons above T_c and the number of broken pairs beneath T_c. The oscillatory part of the signal is due to the impulsive excitations of phonons by the sudden removal of electrons from bonding orbitals or pair breaking. Only phonons with a period longer than the rate of electron excitation or pair breaking can oscillate.

A criticism of the Mazin model is presented in chapter 6, based on the measurements of the rising edge dynamics. We will show that the model cannot explain the non-oscillatory component of the dynamics.

4.6 Kabanov model for YBCO dynamics

This section presents the Kabanov model [53], which describes the temperature dependence of the amplitude and the relaxation time of the photo-induced transients in experiments with low-excitation density. This model explained the dynamics as being due to the superposition of two signals, one related to an s-wave BCS-like gap, the superconducting gap, and one related to an s-wave temperature independent gap, the pseudogap.

Below T_c, the initial photo-excitation by the pump pulse and the subsequent thermalization are estimated to be completed within 100fs. The system is then in a near-equilibrium state with the electron temperature T_e only a few Kelvin in excess of the lattice temperature ($T_e \simeq T_L$). In this case, the pair recombination processes are fast compared to anharmonic phonon decay. The relaxation rate of the photo-induced quasiparticles is thus dominated by phonon relaxation. Because of the presence of the superconducting gap in the low-energy DOS, phonons with energy less than 2Δ cannot contribute to the relaxation of carriers; consequently the situation is strongly modified with respect to that in a metal and a bottleneck occurs after the thermalization. As a result, there is a non-equilibrium distribution of quasiparticles forming a near-steady state with high-frequency phonons with $\hbar\omega > 2\Delta$. The quasiparticle recombination in this system is governed by the emission and absorption of the high-frequency phonons since the phonons with $\hbar\omega < 2\Delta$ do not participate in the direct relaxation.

In this model, the transition probability for the probe light is given by the Fermi golden rule. The amplitude of the photo-induced absorption $\mathcal{A} = \Delta A/A$ is proportional to the number of photo-excited quasiparticles n_{pe}. Therefore, measuring the photo-induced transmission $\mathcal{T}$ or reflectivity $\mathcal{R}$, which are in the weak perturbation limit proportional to $\mathcal{A}$, actually probes the temporal evolution of the photo-excited carrier density n_{pe}.

From the non-equilibrium phonon and quasiparticles distribution and from the con-

servation of energy, Kabanov et al. derived an expression for the photo-excited carrier density n_{pe} for a *temperature independent isotropic* gap:

$$n_{pe} = \frac{\varepsilon_I/\Delta}{1 + \frac{2\upsilon}{N(0)\hbar\Omega_c}\exp(-\Delta/k_BT)} \tag{4.4}$$

and for a *temperature dependent isotropic* gap, i.e. a BCS gap $\Delta(T)$:

$$n_{pe} = \frac{\varepsilon_I/(\Delta(T) + k_BT/2)}{1 + \frac{2\upsilon}{N(0)\hbar\Omega_c}\sqrt{\frac{2k_BT}{\pi\Delta(T)}}\exp(-\Delta(T)/k_BT)} \tag{4.5}$$

where ε_I is the energy per unit cell deposited by the incident pump laser pulse, $N(0)$ is the density of states at E_F, υ is the number of high-frequency phonon modes per unit cell and Ω_c is the phonon cut-off frequency i.e. the highest phonon frequency in the superconductor.

Kabanov et al. were able to fit all the thin film YBCO data from the underdoped regime to the overdoped regime. As a result, the signal obtained in the highly underdoped regime is fitted with a temperature independent isotropic gap as shown in Fig 4.7, and the highly overdoped regime is fitted with a temperature dependent isotropic gap as illustrated in Fig 4.8. The temperature independent gap was associated with the *pseudogap*, whilst the temperature dependent gap was identified with the *superconducting gap*. The dynamics at other doping levels can be fitted with a superposition of the pseudogap and superconducting responses.

The relaxation rate of the photo-induced quasiparticles near T_c is dominated by the energy transfer from the high-frequency phonons to the phonons with $\hbar\omega < 2\Delta$. Kabanov et al. used the kinetic equation for phonons taking into account phonon-phonon scattering and obtained the following expression for the decay rate:

$$1/\tau = \frac{12\Gamma_\omega\Delta(T)^2}{\hbar\omega^2\ln\{1/(\varepsilon_I/2N(0)\Delta(0)^2 + \exp(-\Delta(T)/k_BT))\}} \tag{4.6}$$

where Γ_ω and ω are the linewidth and frequency of the main high-energy phonon involved in the relaxation. Kabanov et al. assumed that the main phonon mode is the A_{1g}-symmetry apical O(4) with linewidth $\Gamma_\omega \cong 13$ cm^{-1} and frequency $\omega \cong 400$ cm^{-1}.

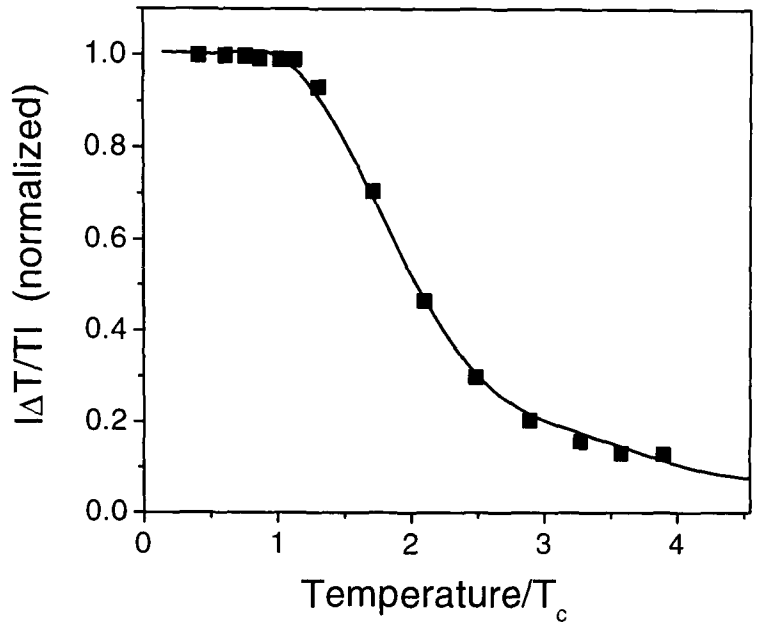

Figure 4.7: Temperature dependence of the photo-induced transmission in underdoped YBCO (δ = 0.18, T_c = 77K) measured by Mihailovic et al. [120] The solid line is the induced transmission from equation 4.4 for a temperature independent gap.

Expression (4.6) fits the divergence of the relaxation time τ at T_c observed in all data on YBCO, as illustrated in Fig 4.9. Upon increasing temperature closer to T_c less low-energy phonons become available for re-absorption, meaning the recombination mechanism becomes less and less efficient. Consequently the relaxation time increases, explaining the divergence at T_c. A *temperature dependent isotropic* gap was used to obtain (4.6), but theoretical investigation of the relaxation time still needs to be done in the case of a predominantly d-wave gap.

Kabanov et al. also derived an expression for n_{pe} from a temperature dependent and independent anisotropic gap with nodes. The difference between an s-wave and a d-wave (or strongly anisotropic s-wave) gap symmetry can be observed at low temperature only. In the d-wave case, the model predicts a decrease of the signal magnitude already from 4K instead of a constant value observed until about 60K (cf. Fig 4.7).

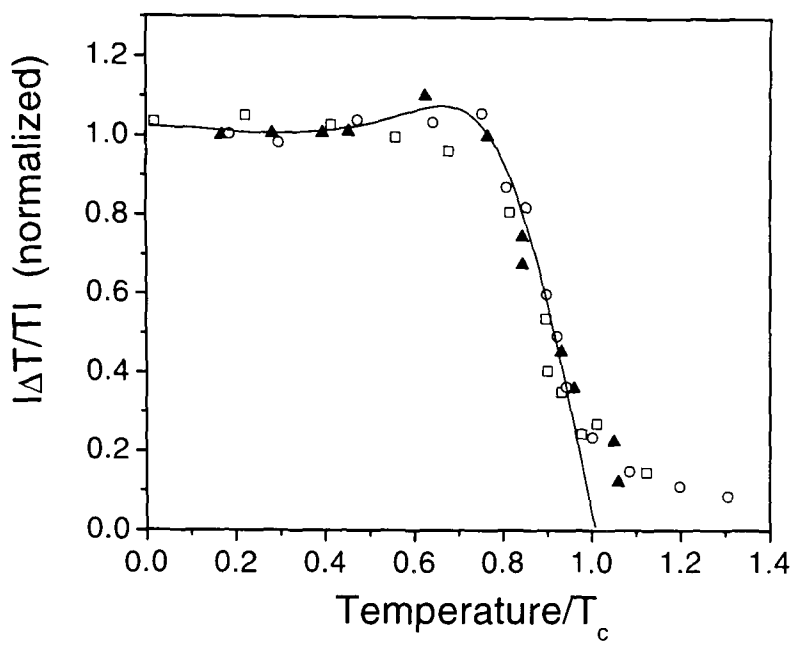

Figure 4.8: Temperature dependence of the photo-induced transmission in overdoped YBCO ($\delta = 0.1$, $T_c = 90K$) measured by Mihailovic et al. [120] (open circles), Stevens et al. [116] (open squares) and Han et al. [98] (solid triangles). The solid line is the induced transmission from equation 4.5 for a temperature dependent gap.

4.7 Slow Component Models

In addition to the fast transient response occurring on a femtosecond timescale, a distinct slower response was consistently observed in YBCO [116], BSCCO-2212 and $Bi_2Y_xCa_{1-x}SrCu_2O_8$ [8]. This component is reproducible and exhibits a divergence at T_c, as shown in Fig 4.10 for YBCO. It was attributed to bolometric effects by Eesley et al. [9] in the same way it has been attributed in metals. The first explanation as a possible non-bolometric origin of this component was given by Thomas et al. [8] followed by a detailed study by Stevens et al. [116]. The data in Fig 4.10 are well fitted with a thermally-activated model with an activation energy of $3.5k_BT_c$. For a BCS-like isotropic gap, the obvious quantity which follows a thermally-activated temperature dependence is the population of quasiparticles. A d-wave gap would modify the temperature dependence of the population of thermally-excited quasiparticles via the density of states,

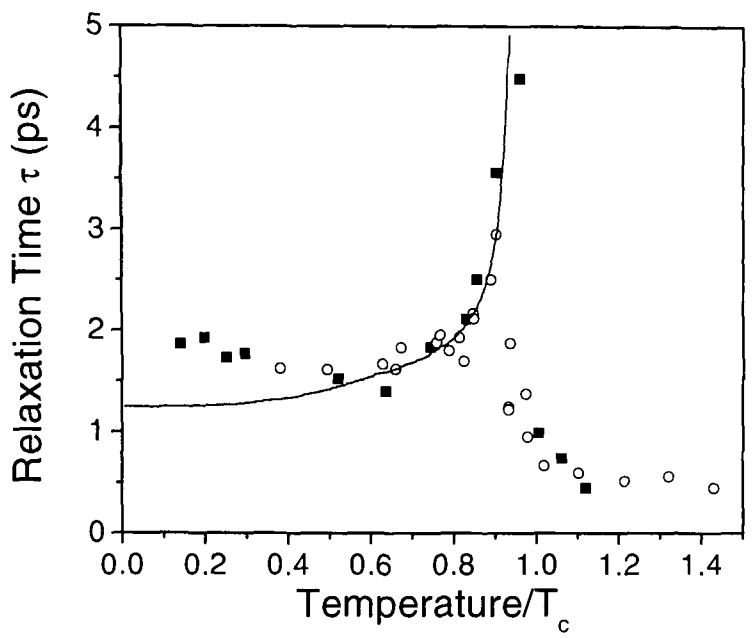

Figure 4.9: Relaxation time τ of optimally-doped YBCO from Han et al. [98] (squares) and Mihailovic et al. [120] (circles). The fit is from equation 4.6.

however a calculation is complicated by a lack of understanding of the detailed band structure. From their fit, Stevens et al. [116] proposed two possible models.

A non-thermal quasiparticle model where the pump excites electrons from states below the Fermi energy to unpaired hole states at the Fermi energy. The probe beam can then excite these electrons to higher lying states leading to an increased absorption. The thermalization time of the quasiparticles being a few picoseconds is in disagreement with the lifetime of the long-lived component being over 12ns, the repetition time between two consecutive laser pulses. Stevens et al. proposed that the long-lived component is due to the presence of localized unpaired hole states near the Fermi energy, which is supported by the observation of a Van Hove singularity just below E_F in ARPES measurements [72]. Kabanov et al. [117] developed a theoretical model for intra-gap localized states and explained both the lifetime and the temperature dependence of the slow component.

The second model is a bolometric quasiparticles model where the pump heats the superconductors leading to an increased thermal population of quasiparticles at the Fermi energy and, as in the first model, to an increased probe absorption. Concerning the

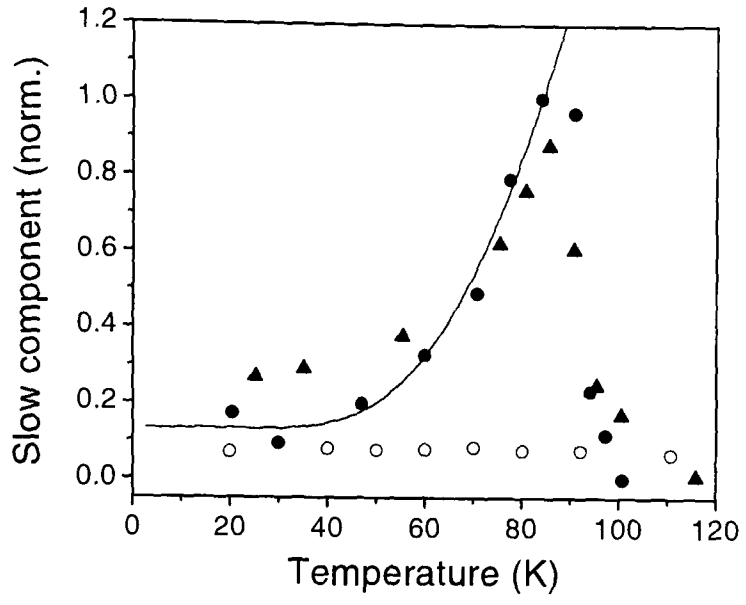

Figure 4.10: Temperature dependence of the long-lived component of optimally-doped YBCO in photo-induced transmission. The solid circles are from Stevens at al. [116], the triangles from Mihailovic et al. [122] and the line is a thermally-activated fit $e^{-\frac{3.5k_BT_c}{T}}$. The open circles were obtained from insulating YBCO.

detailed feasibility of the bolometric model, Smith [118] developed a thermal diffusion model and predicted a time constant for the decay of the bolometric effects of 21ns, in agreement with the data within the experimental errors. In this model, the magnitude of the photo-induced signal is proportional to the increase in the number of thermally-excited quasiparticles caused by heating of the sample by the energy from the pump pulse. Thus, the temperature dependence of the slow component is given by the derivative of the thermal quasiparticle population with respect to the temperature divided by the heat capacity [119]. The low-temperature heat capacity rises much more slowly than the activated temperature dependence and thus the temperature dependence of the slow component magnitude is still approximately following an activated dependence.

4.8 Conclusion

At low-excitation density, most of the YBCO data from different groups [98, 116, 120] are now consistent with each other for the photo-induced reflectivity and transmission and from the underdoped to the overdoped regime. There is now a consensus that the fast component below T_c is somehow connected with modifications in the low-energy excitation spectrum associated with the formation of the superconducting gap below T_c. However, none of the theoretical interpretations of the experimental results [13, 53, 98, 121] are widely accepted. As Kabanov et al. [53] argued, the underdoped response seems to be related to the pseudogap, whilst the overdoped response to the superconducting gap. The model they developed fits well the data for the entire doping dependence, however it raises important questions. Kabanov et al. concluded from the temperature dependence of the transient magnitude that the superconducting gap has an s-wave symmetry. Most of the HTSC experiments and theories are today in favor of a predominantly d-wave superconducting state as seen in section 2.6. Moreover, we saw that the model implies the presence of two sets of uncoupled phonons, which is not understandable with our present understanding of HTSC.

Most of the previous ultrafast studies of HTSC have been made on YBCO, which is special because of the presence of the chains introducing a strong anisotropy in the a-b plane and a second, higher plasma frequency. In this thesis, we present measurements of detwinned YBCO single crystal to show the influence of the chains on the dynamics and to remove the chain component from the underlying component.

The previous measurements on Bi and Tl-compounds were realized at the early stage of the growth of these materials and sample quality problems, such as high defect density and poor stability, could be responsible for the discrepancy between the different results. Moreover, no consistent work has been made so far on the temperature, intensity and doping dependence on those materials. In this thesis, we will also focus on these materials

to measure a universal response to the HTSC.

One of the main disagreements in the literature is about the nature of the probe mechanism. As we saw, three possibilities have been put forward: Fermi surface smearing [100], Drude reflectivity [98] and lattice distortion [13]. No systematic study of the probe wavelength dependence has been done so far apart from femtosecond measurements at room temperature and at high-excitation [106, 107]. However, a compilation of data on near-optimally-doped YBCO from different groups [97, 98, 105, 110, 113, 116, 122] shows that the photo-induced reflectivity is positive below 1.98eV and negative above 2eV which is in opposition with the Drude reflectivity and the lattice distortion model. The next chapter presents new measurements as a function of the probe beam photon energy and provides new insights into this issue.

Chapter 5

Femtosecond Spectroscopy of $Bi_2Sr_2CaCu_2O_{8+\delta}$ & $Tl_2Ba_2CuO_{6+\delta}$

Ultrafast spectroscopy has already been widely used to study carrier dynamics in $YBa_2Cu_3O_{7-\delta}$ (YBCO), however questions remain about the general applicability of the results to other cuprates. Recent heat capacity measurements strongly suggest that the electronic excitations of the condensate in YBCO may be quite different from those in other cuprates including $Tl_2Ba_2CuO_{6+\delta}$ (TBCO-2201) and $Bi_2Sr_2CaCu_2O_{8+\delta}$ (BSCCO-2212) [3]. In this chapter, we present measurements of the ultrafast optical response of thin films and single crystals of BSCCO-2212 and thin films of TBCO-2201, focusing on the dynamics associated with the superconducting and the pseudogap states.

Previous studies of HTSC have shown clear evidence of ultrafast relaxation associated with the pair density dynamics in YBCO-123 [53, 110, 116] and preliminary measurements of BSCCO-2212, BSCCO-2223 [8, 96, 97] and TBCO-2223 [9] suggest that systematic measurements of those materials might yield useful information about the nature of the gaps in both the superconducting and normal phase. BSCCO-2212 and TBCO-2201, which are described in this chapter, have the important advantages of being chemically

inert, they do not to exhibit twins and, furthermore, do not contain the Cu-O chains which complicates the optical response of the YBCO-123 materials.

Measurements of the time-resolved photo-induced reflectivity $\mathcal{R} = \Delta R/R$ were made using a pump-probe technique, as previously described in chapter 3. The samples were excited by 100fs laser pulses, either at 1.5 or 3.0eV, and then probed at 1.5eV with a time resolution of about 140fs. The results obtained with different pump energies are very similar and we report here only the 3eV data, which corresponds to optical excitations lying in the broad band of Cu-O charge transfer excitations. The samples were mounted in an exchange gas cryostat and precautions were taken to minimize laser heating. We used the same experimental conditions to measure both TBCO and BSCCO.

We have measured a range of BSCCO-2212 samples including single crystals and thin films. The single crystals were flux-grown and slightly overdoped, coming from two different sources (cf. section 3.5 for more detail). They have critical temperatures in the range of 82.8 to 85.7K, with transition widths of 0.5 to 1K. The thin films are slightly underdoped, 300 to 400nm thick and grown on $LaAlO_3$ by rf magnetron sputtering with $T_c \geq 66$K and a transition width of about 7K. The measured dynamics was qualitatively the same for all the samples, single crystals and thin films. The main difference is that single crystals showed larger heating on illumination probably due to the much lower thermal conductivity of BSCCO compared with the $LaAlO_3$ substrate.

We present the first study of the ultrafast optical response in TBCO-2201 [10]. The samples used in this study were thin films grown on $SrTiO_3$ substrates by rf magnetron sputtering followed by post-deposition annealing [18]. Those samples are known to be the highest quality thin films available at the moment for this material. Here we will present measurements of optimally-doped material with a critical temperature of 82K and a transition width of 8K. It is known that TBCO-2201 could pose special problems for measurements of ultrafast dynamics. For instance, it can be photo-doped [123], however

within the sensitivity of our experiment no such effect was observed. Unfortunately, we did observe damage to the sample from both the pump and probe laser beams at temperatures above 225K. For excitation intensities of $5\mu Jcm^{-2}$, the sample was clearly ablated leaving holes in the films. The rate of ablation was clearly higher for the 3.0eV pump light with holes forming after exposure on the timescale of minutes. This effect has not been seen with either YBCO-123 or BSCCO-2212 under similar experimental conditions. At temperatures below 225K, no damage to the sample was observed and fully reproducible results were obtained over several days of experimenting on the same part of the sample.

We first present the general temperature dependence of the dynamics before going into more detail of the dynamics of the superconducting, pseudogap and normal states. All the measurements are in the weak perturbation limit (photo-excitation density $\leq 10\mu Jcm^{-2}$), where we focus attention on the dynamics of electronic excitations, but we also present here some data in the strong perturbation limit ($\geq 1mJcm^{-2}$), where the superconducting condensate is completely destroyed. In the next section, we show evidence of superconducting correlation effects in TBCO-2201 for temperatures above T_c. We also present new ultrafast measurements as a function of the probe beam wavelength. Finally, before an overall discussion of the new results, we present measurements of the long-lived behaviour in BSCCO and TBCO.

5.1 Temperature Dependence of the Dynamics

The ultrafast photo-induced reflectivity at 1.5eV in BSCCO was measured for sample temperatures in the range of 4 to 300K. The temperature dependence of the dynamics shows three distinct temperature regions corresponding to the three different electronic groundstates of the material, as illustrated in Fig 5.1. The three regions, presented in detail in the next sections, can be described as the following:

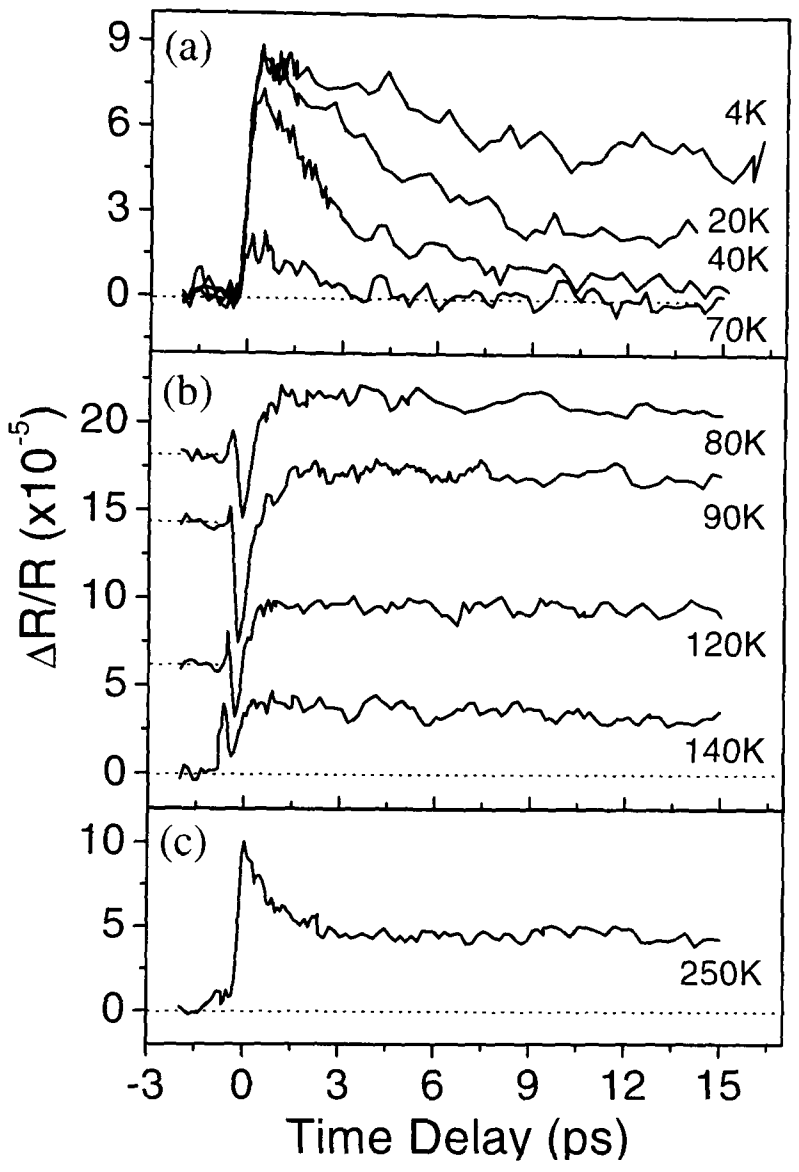

Figure 5.1: Photo-induced reflectivity of slightly overdoped BSCCO-2212 single crystal (T_c = 84K) in the (a) superconducting (b) pseudogap and (c) normal state. The response has been offsetted to remove the long-lived component and the 80, 90 and 120K scans have been offsetted for a clear presentation. The excitation density is $1.2\mu Jcm^{-2}$ in (a) and $24\mu Jcm^{-2}$ in (b) and (c), which explains the change of the signal magnitude between (a) and (b)/(c).

Superconducting phase ($T < T_c$): At 4K the differential reflectivity presents a resolution-limited, $\sim$ 150fs, *positive* transient with a long relaxation time of 40ps. With increasing temperature towards $T_c = 84K$, the signal magnitude decreases to zero and the relaxation time decreases to approximately 3ps. The signal magnitude follows the condensate density n_s, as it can be compared with penetration depth measurement (cf. section 5.2) and the decay rate of the signal is linear in temperature, which is quite different from the decay rate observed in YBCO [53, 110, 116].

Pseudogap phase ($T_c < T < T^*$, where T^* is the pseudogap onset temperature): The differential reflectivity shows a fast, resolution-limited *negative* transient with a temperature independent relaxation time of 0.5 - 1ps. The signal magnitude of the negative transient is a maximum at 110K and then decreases approximately linearly to zero at T^*. This intermediate regime coincides with the pseudogap phase detected in ARPES measurements [124] and other techniques [125], which estimated T^* to be around 125K in optimally-doped crystals and 170K in optimally-doped thin films.

Normal phase ($T > T^*$): A *positive* transient is measured again in the normal phase. The relaxation of the initial peak is on the timescale of $\sim$3ps and is followed by a long-lived signal. This response is in agreement with previous measurements of the room temperature dynamics [96] and is similar to a metallic response.

The TBCO-2201 data presented in Fig 5.2 reveal a qualitatively similar behaviour to BSCCO-2212 above and below T_c. Indeed, in the superconducting state, the dynamics is characterized by a ultrafast increase in reflectivity, whereas close to and above T_c, there is an ultrafast decrease (negative transient). The dynamics is sensitive to the superconducting phase transition with a change in sign of the photo-induced reflectivity accompanied by speeding up of the relaxation at T_c. However, photo-assisted structural

changes occur above 225K, making impossible any measurements above this temperature. Consequently TBCO-2201 provided data in the superconducting and pseudogap state but not in the normal state.

The magnitude of $\mathcal{R}$ is about 3 times larger in TBCO than in BSCCO for a similar excitation density. Moreover, due to the very good quality of the TBCO thin films and hence to less light scattering of the probe beam, the noise level in the TBCO measurements is on the order of $2{\cdot}10^{-6}$, a factor of two lower than for BSCCO under the same experimental conditions. Therefore, the signal-to-noise ratio for TBCO is almost an order of magnitude better than for BSCCO.

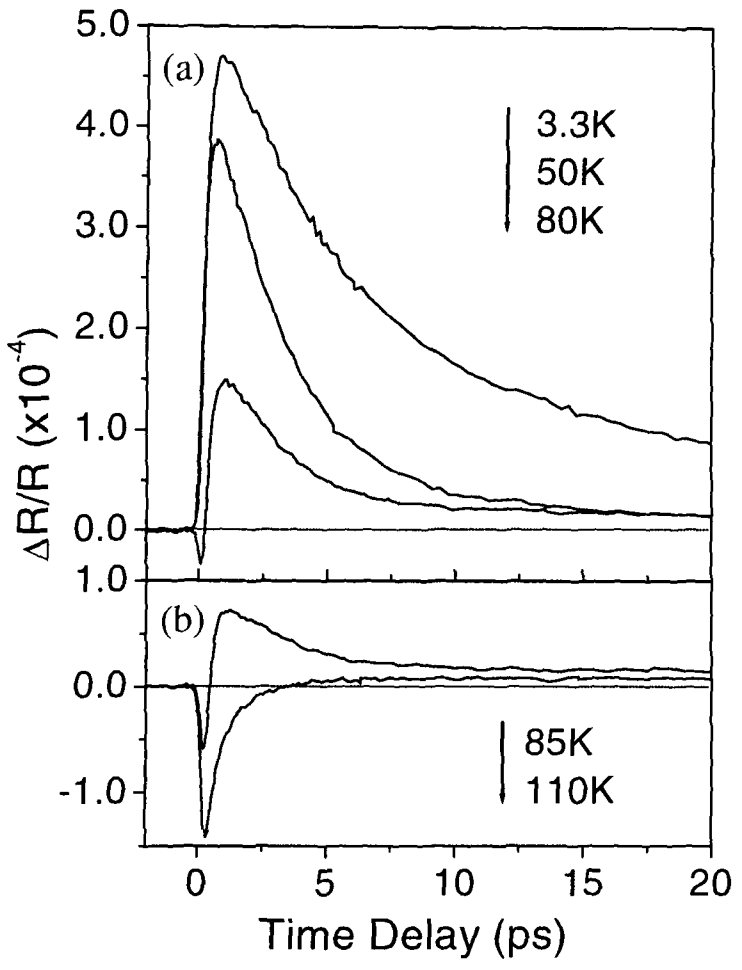

Figure 5.2: Photo-induced reflectivity of optimally-doped TBCO-2201 thin film (T_c = 82K) in the (a) superconducting and (b) pseudogap state. The response has been offsetted to remove the long-lived component. The excitation density is $2\mu Jcm^{-2}$.

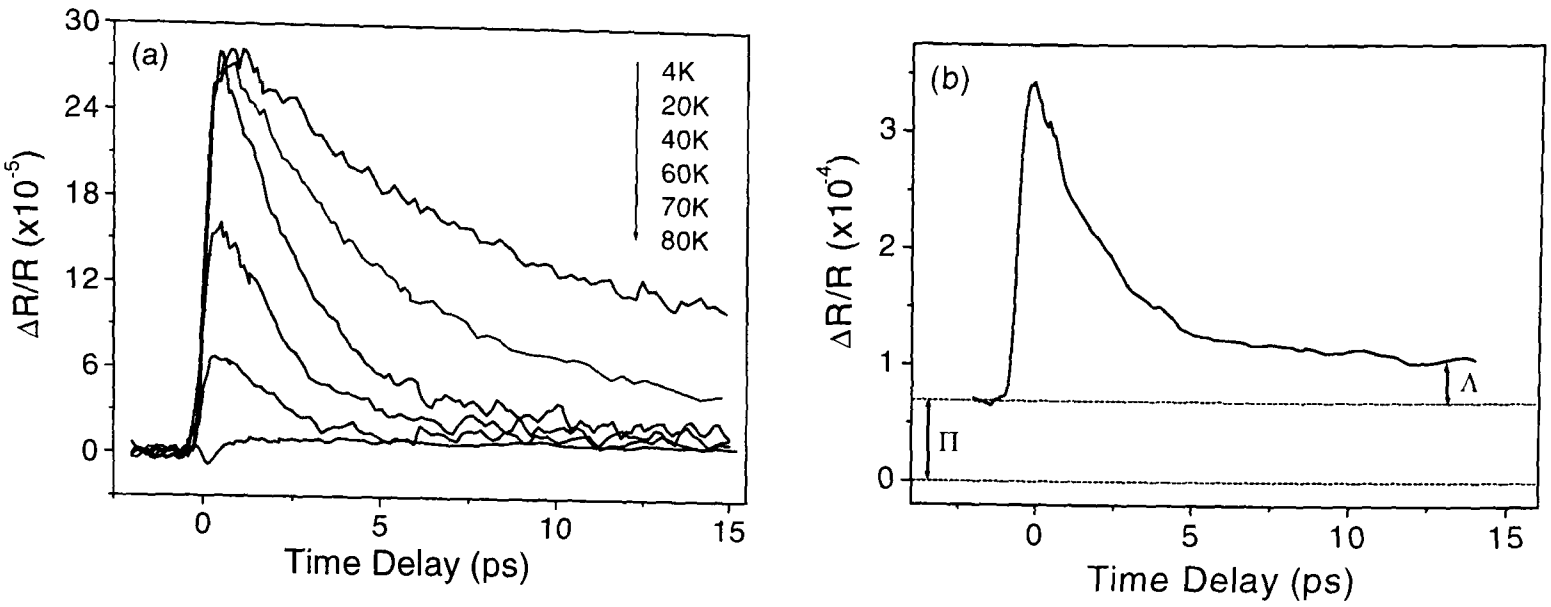

Figure 5.3: (a) Photo-induced reflectivity of slightly overdoped BSCCO-2212 single crystal (T_c = 86K) in the superconducting state. The response has been offsetted to remove the long-lived component. The excitation density is 1.2μJcm^{-2}. (b) Dynamics at 20K with an excitation density of 6μJcm^{-2}. We can observe the long-lived component Λ after 15ps and the component Π after 12ns.

5.2 Superconducting State Dynamics

The time dependence of the photo-induced reflectivity in the superconducting phase of the oxygen annealed BSCCO single crystal (T_c = 86K) is presented in Fig 5.3a. In general, the response can be separated, as for YBCO, into two components which are characterized by different timescales, as illustrated in Fig 5.3b. The initial component, which decays within a few tens of picoseconds and a longer-lived component, which lasts longer than 12ns, the laser pulse separation. The long-lived component can be characterized by the signal Λ after the initial transient (at 15ps in this example) relative to the signal at -3ps; or by the signal Π at -3ps, which is effectively a time delay of +12ns, the pulse separation time. The differential reflectance of TBCO, presented in Fig 5.4, is very similar to the BSCCO data, consisting of an initial component which decays within 40ps and a much longer-lived component.

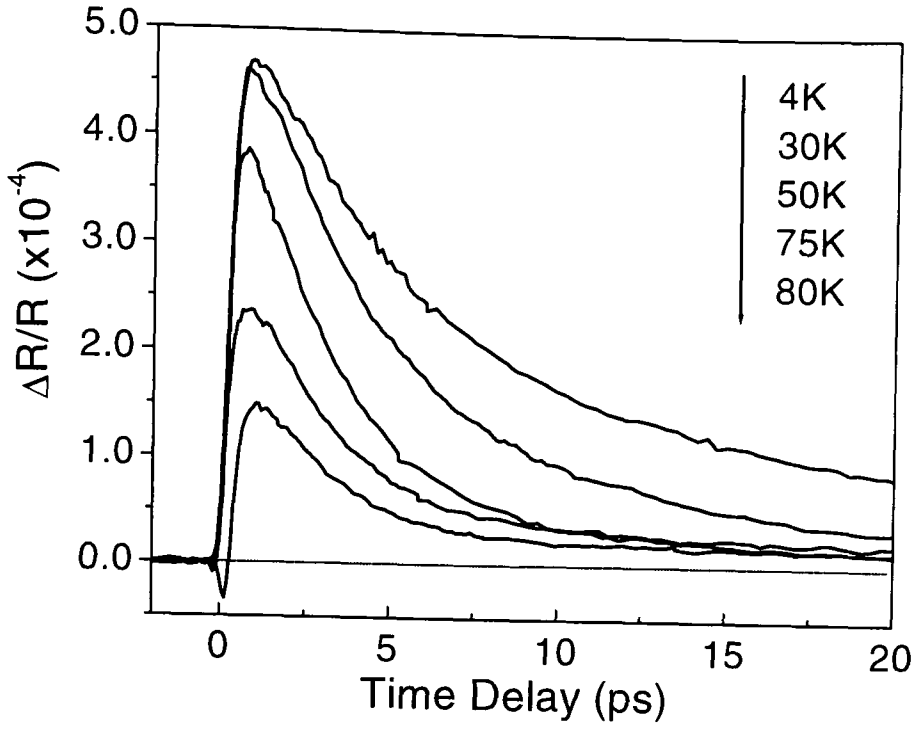

Figure 5.4: Photo-induced reflectivity of slightly overdoped TBCO-2201 thin film (T_c = 82K) in the superconducting state. The response has been offsetted to remove the long-lived component. The excitation density is $2\mu Jcm^{-2}$.

In both materials the 4K response is positive, $\mathcal{R} > 0$. It shows a resolution-limited risetime, $\sim$ 140fs and a very slow recovery time of more than 25ps, depending on the excitation density (cf. Fig 5.9). The peak amplitude of the initial component is highly temperature dependent, as shown in Fig 5.5 which shows the results of measurements on the same BSCCO single crystal. The response decreases monotonically with increasing temperature and approaches zero close to T_c (as obtained from susceptibility and resistivity measurements). This behaviour is qualitatively similar to that reported previously for YBCO [116]. We measured very similar dynamics in BSCCO-2212 single crystals and thin films, as illustrated in Fig 5.6 for T = 4K and at an excitation density of $6\mu Jcm^{-2}$. Variations in the signal magnitude between samples have always been observed due to different equilibrium reflectivities. The temperature dependences of the peak values of all single crystals are very similar to the one shown in Fig 5.5, however measurements of thin film samples slightly vary. They all decrease to zero at T_c, but some thin film samples

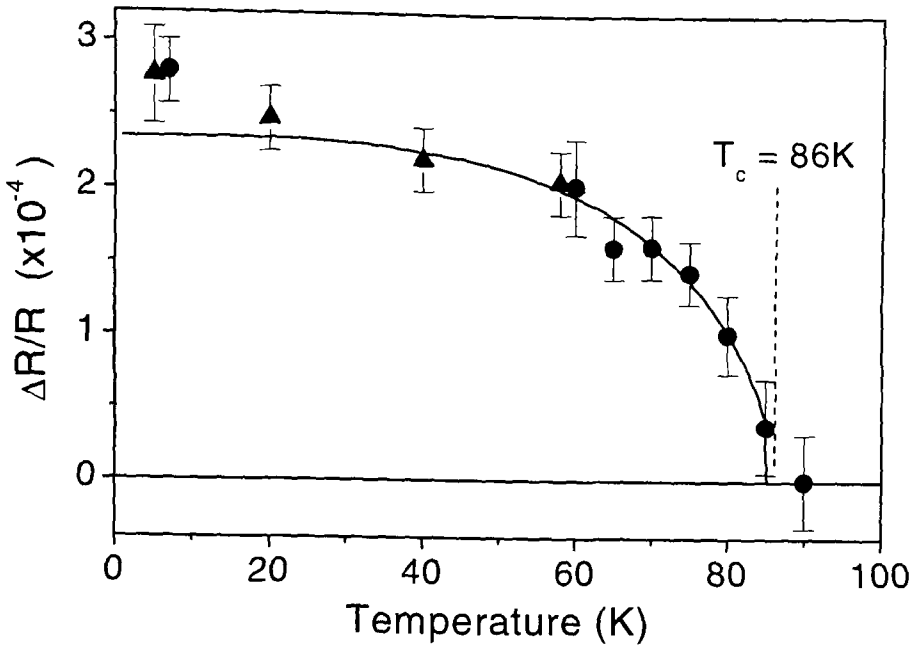

Figure 5.5: Temperature dependence of $|\mathcal{R}|_{max}$ in the superconducting state of BSCCO-2212 single crystal with T_c = 86K. The excitation density is $1.2\mu Jcm^{-2}$. The solid line is the weak-coupling BCS gap function.

exhibit a behaviour between a BCS temperature dependence and a linear dependence all the way from the maximum value at 4K to zero at T_c.

The temperature dependence of the TBCO magnitude in the superconducting state signal is presented in Fig 5.7. The initial part of the decay is more temperature dependent than in the BSCCO results, and there is a change of slope at about 70K probably due to the onset of the negative component related to the pseudogap state.

The solid curve in Fig 5.5 indicates that $|\mathcal{R}|_{max}$ displays a behaviour consistent with a two-fluid weak-coupling BCS gap function, suggesting that the optical response is proportional to the gap magnitude, decreasing towards zero with increasing temperature. The temperature dependence of the TBCO signal magnitude in Fig 5.7 and of most measurements of BSCCO thin films indicate more that the signal magnitude is reminiscent of $n_s(T)$, the superconducting pair density, determined from microwave penetration depth measurements on TBCO [127] and on other HTSC [128]. In particular, it varies approximately linearly for $T < 70K$, and it approaches zero at T_c more slowly than the

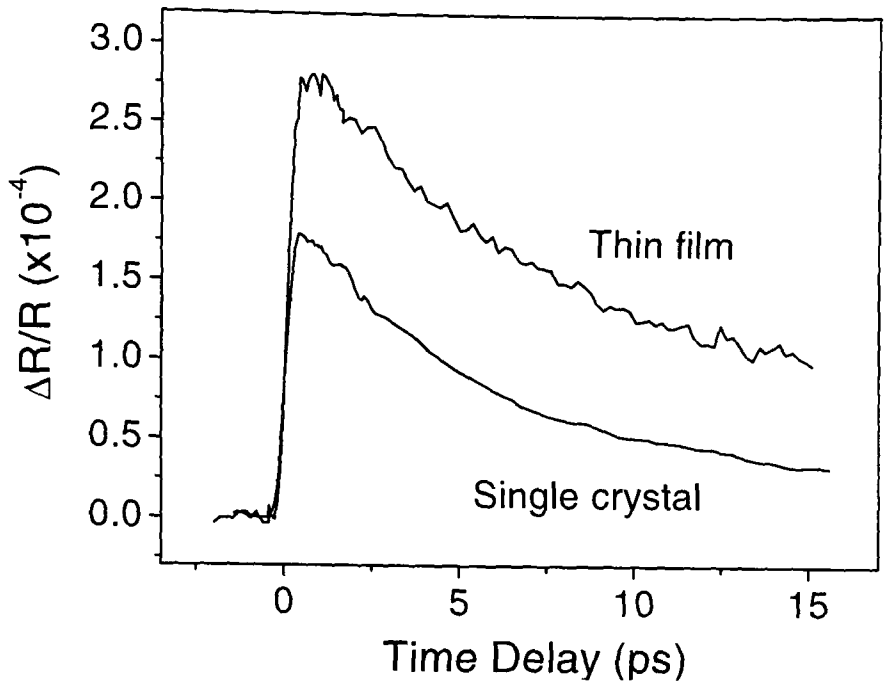

Figure 5.6: Comparison between the single crystal and the thin film BSCCO-2212 dynamics at 4K and at an excitation density of $6\mu\text{Jcm}^{-2}$.

weak-coupling BCS gap behaviour. The fact that the temperature dependence varies from one sample to another one is also an indication of a link with the superconducting pair density, as a sample dependence has also been observed in penetration depth measurements [127]. The in-plane penetration depth $\lambda_{ab}(T)$ is deduced from microwave surface impedance measurements [127] and the superconducting pair density $n_s(T)$ is deduced from $\lambda_{ab}(T)$ with the Ginzburg-Laudau model [128].

The simplest interpretation of this temperature dependence is that the 1.5eV reflectivity has a component proportional to the condensate density and that the exciting pulse destroys the condensate [116]. However, this is not supported by the linear intensity dependence of the signal in the range of 0.2 to $26\mu\text{Jcm}^{-2}$ or by experiments we have performed using a regeneratively amplified Ti:Sapphire (cf. section 5.5). These measurements show a saturation of the superconducting response and a change in the qualitative nature of the dynamics indicative of the destruction of the condensate at an excitation of 1.2mJcm^{-2}. We concluded that in the low-excitation intensity experiments, only a small fraction of the pairs are broken, estimated to be smaller than 2% (cf. section 5.5).

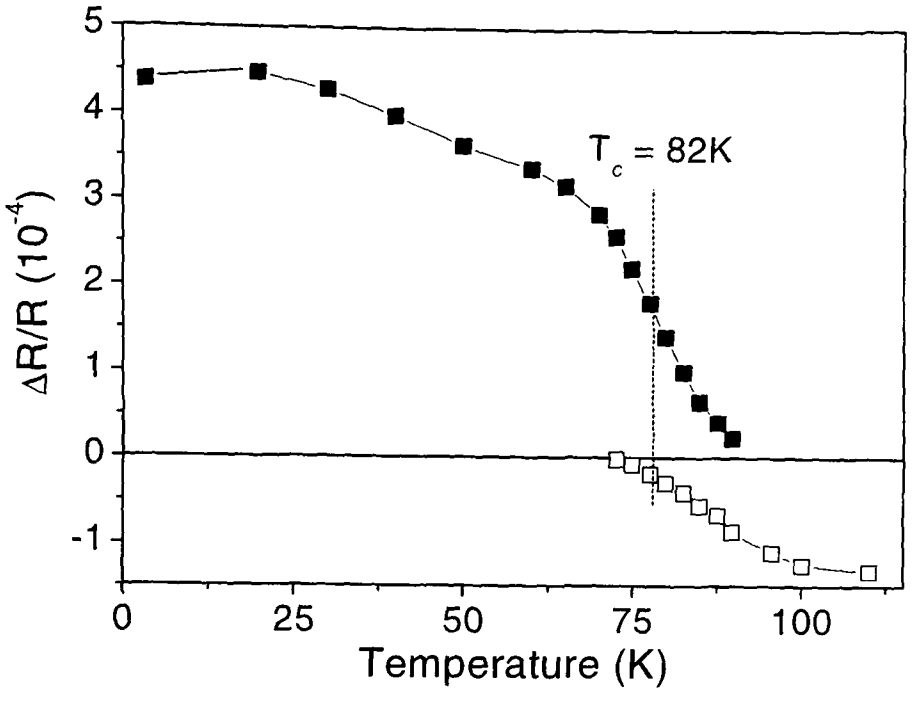

Figure 5.7: Temperature dependence of the initial transient magnitude of the superconducting state of TBCO-2201 thin film with $T_c = 82K$. The open squares are the magnitude of the negative signal in the pseudogap state. The excitation density is $2\mu Jcm^{-2}$.

The temperature and intensity dependence of $|\mathcal{R}|_{max}$ in both BSCCO and TBCO can be explained if there is a component of the reflectivity at 1.5eV proportional to superconducting pair density n_s, as observed in thermal difference spectroscopy [68]. Subsequently, the number of pairs broken during photo-excitation has to be proportional to the equilibrium population of pairs times the number of photo-excited carriers and secondly, the change in reflectivity $\mathcal{R}$ has to be proportional to the number of broken pairs. In this way, the peak value of $\mathcal{R}$ is proportional to n_s. In this model, the initial transient is associated with pair breaking, whilst the decay of the initial component is associated with the energy relaxation of the non-equilibrium carriers i.e. it follows the recombination of unpaired quasiparticles to reform pairs.

In addition to the slowing with decreasing temperature, the dynamics of BSCCO-2212 and TBCO-2201 show a qualitative change in the initial transient relaxation at about 20K. Above this temperature, the decay is well fitted by a mono-exponential decay,

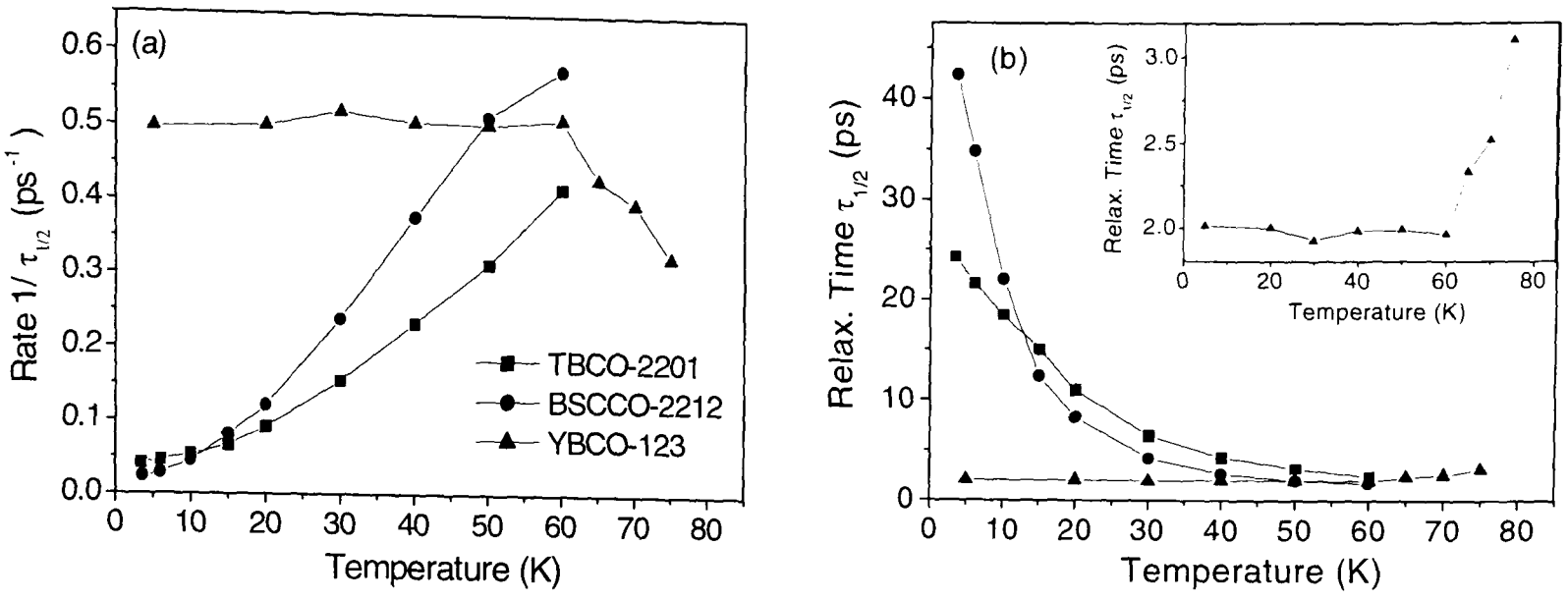

Figure 5.8: (a) Temperature dependence of decay rate $1/\tau_{1/2}$ of the initial dynamics in the superconducting state of BSCCO, TBCO and YBCO for comparison. (b) Temperature dependence of the relaxation time $\tau_{1/2}$ with a zoom for the YBCO dependence in inset. The excitation density is $1.2\mu\text{Jcm}^{-2}$.

however at lower temperatures, a more complicated temperature dependence, such as a bi-exponential decay, is required. In order to provide a preliminary characterization of the relaxation rate, we present measurements of the decay rate $\tau_{1/2}^{-1}$, the inverse half-life, in Fig 5.8a and of the corresponding relaxation time $\tau_{1/2}$ in Fig 5.8b. The data clearly show that the relaxation is strongly temperature dependent even for $T \ll T_c$. In this respect, BSCCO-2212 and TBCO-2201 behave very differently from YBCO-123, also represented in Fig 5.8 for comparison.

At low temperature the relaxation times are almost an order of magnitude larger than the values reported previously for YBCO (see for instance references [53, 110, 116]). Raising the sample temperature dramatically reduces the relaxation time by an order of magnitude over the temperature range up to T_c. $\tau_{1/2}$ increases from 3ps at 60K to 40ps at 4K for BSCCO, and from 3ps at 60K to 25ps at 4K for TBCO. The relaxation rate increases approximately linearly with increasing temperature, although there is some

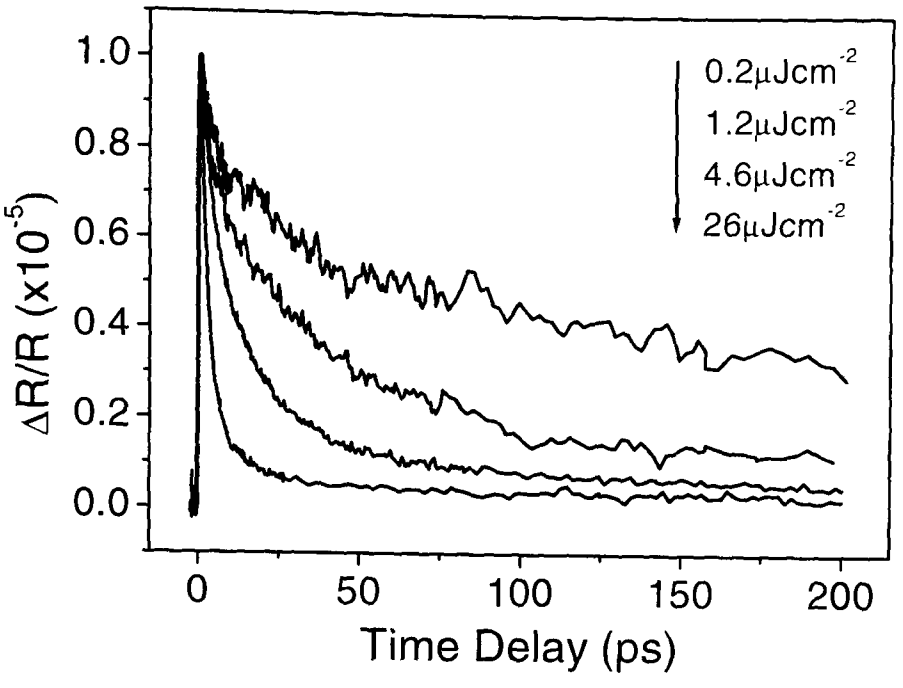

Figure 5.9: Intensity dependence of the superconducting state dynamics at 4K of optimally-doped BSCCO-2212. Intensities are in the range of 0.2 to $26\mu Jcm^{-2}$.

variation in the trend close to the critical temperature from sample to sample, as the decay is difficult to measure due to the very small signal magnitude close to T_c.

The change of slope of the relaxation rate at very low temperature ($T \lesssim 20K$) could be due to the increase of the sample heating at low temperature, explained by the decrease of the heat capacity as the temperature goes to zero [5]. In other words, the temperature indicated in Fig 5.8 would be actually lower than the real value for very low temperatures giving the upturn observed from about 20K down to 4K, which could explain the slightly non-linear temperature dependence of the rate for $T \lesssim 20K$.

Our new results contrast with those obtained by Chwalek et al. [97] for BSCCO-2223 thin films, where the rate was observed to be approximately temperature independent throughout the superconducting phase. Measurements of YBCO also indicate that the relaxation time is only weakly temperature dependent except close to T_c [110, 129] as shown in Fig 5.8. The most likely sources of discrepancy in these results are the sample quality and the extremely high-excitation density used in the previous experiments. The

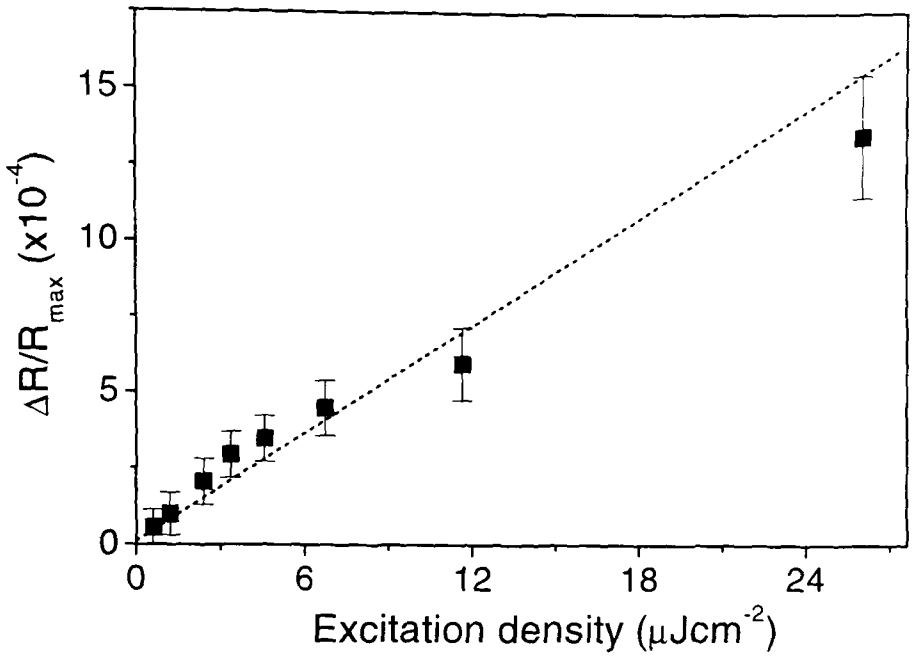

Figure 5.10: Intensity dependence of the peak values of optimally-doped BSCCO-2212 at 4K.

fact that we observe a long relaxation time at low temperatures is consistent with the high-quality of our single crystals and thin films, where elastic scattering by defects and dislocations is strongly reduced which allows the underlying inelastic scattering processes to be probed. These results are discussed in section 5.9.

The time dependence of the initial component is strongly dependent on temperature but also on the excitation intensity. The intensity dependence from 0.2 to 26μJcm^{-2} of the superconducting dynamics of BSCCO-2212 is presented in Fig 5.9. In this range of intensities, the signal magnitude is basically linear in intensity for BSCCO-2212 and TBCO-2201, as illustrated for the superconducting state in Fig 5.10 with the intensity dependence of the peak values for BSCCO-2212 at 4K. The relaxation time varies as the inverse of the excitation density, as shown in Fig 5.11 for T = 4 and 10K. The effect of an increased excitation intensity on the dynamics is very similar to an increase in temperature. Indeed, the 4K data are equivalent to the 10K data shifted by an excitation density of 1.8μJcm^{-2}, meaning that an increase of 1.8μJcm^{-2} could be equivalent to an increase of temperature from 4 to 10K, as far as the relaxation time is concerned. It is

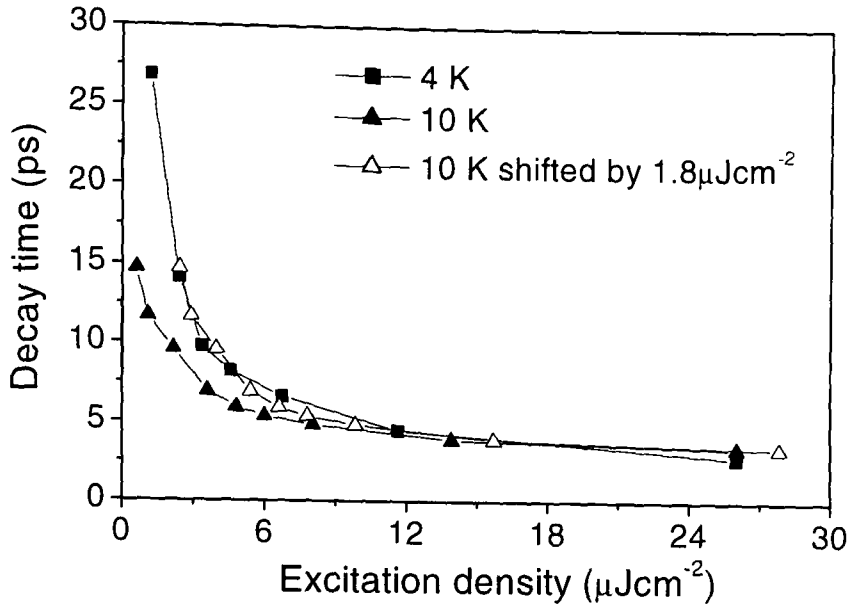

Figure 5.11: Excitation density dependence of the relaxation time of BSCCO-2212 at 4 and 10K and at 10K shifted by $1.8\mu\text{Jcm}^{-2}$.

therefore possible that the intensity effect comes from cw sample heating, at least at 4K. However, we stressed earlier that, in order to explain the temperature dependence of the peak value in Fig 5.5 and 5.7, the number of pairs broken during photo-excitation has to be proportional to the equilibrium population of pairs times the number of photo-excited carriers and $\mathcal{R}$ has to be proportional to the number of broken pairs. This argumentation concerning the temperature dependence of the $\mathcal{R}$ peak values also provides the simplest explanation for the linear intensity dependence observed at $T < T_c$.

5.3 Pseudogap State Dynamics

Fig 5.12 shows the development of the BSCCO-2212 response as the temperature is raised above T_c. Because of the very weak photo-induced signal at $T > T_c$ the excitation density was increased from $1.2\mu\text{Jcm}^{-2}$ in the superconducting state, to $24\mu\text{Jcm}^{-2}$; however the behaviour is qualitatively the same, independently of the excitation density in the low-density limit. There is now significant sample heating but not as severe as at 4K, as the thermal conductivity and the heat capacity are much larger close to T_c. We now

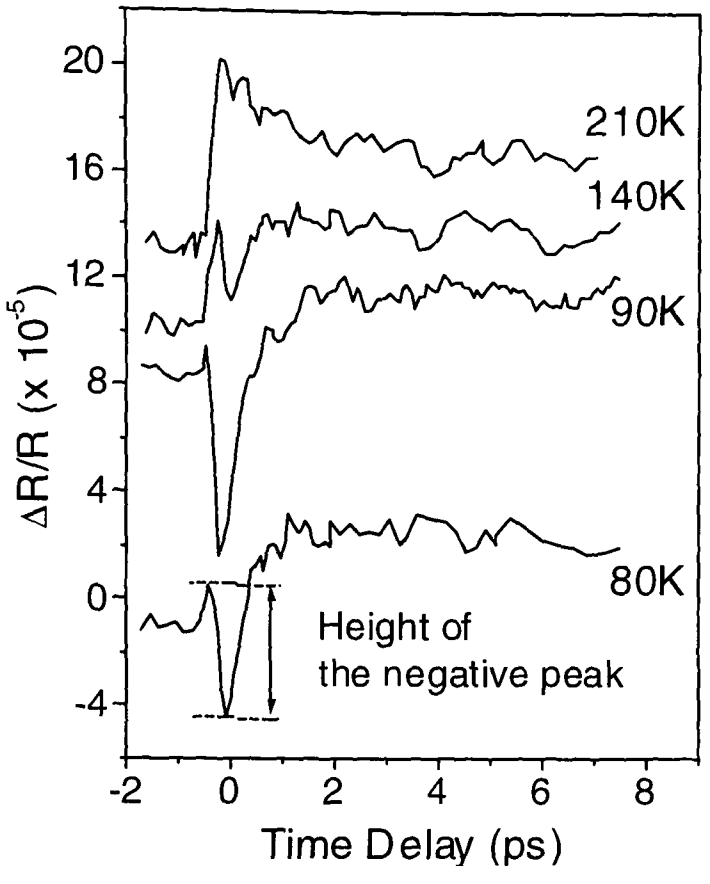

Figure 5.12: Photo-induced reflectivity of slightly overdoped BSCCO-2212 single crystal ($T_c = 86K$) in the pseudogap state. The responses have been offsetted for a clear presentation. The excitation density is $24\mu Jcm^{-2}$.

observe an ultrafast positive transient at zero delay with a clear development of an ultrafast *negative* $\mathcal{R}$ which peaks about 300fs after the positive peak. The amplitude of the negative component first increases with temperature, reaching a maximum near 110K. On further increasing the temperature, the negative $\mathcal{R}$ transient decreases and at the same time a positive response builds up that eventually develops into a characteristic metallic response at much higher temperatures. It should be stressed that there is no sharp transition from the superconducting phase to this intermediate phase, the response appearing to evolve in a continuous fashion.

The temperature dependence of the amplitude of this negative differential reflectance signal is shown in Fig 5.13a. The effect is strong in the temperature range of T_c to T_c + 35K, which corresponds to the temperature range in which a pseudogap is observed in the

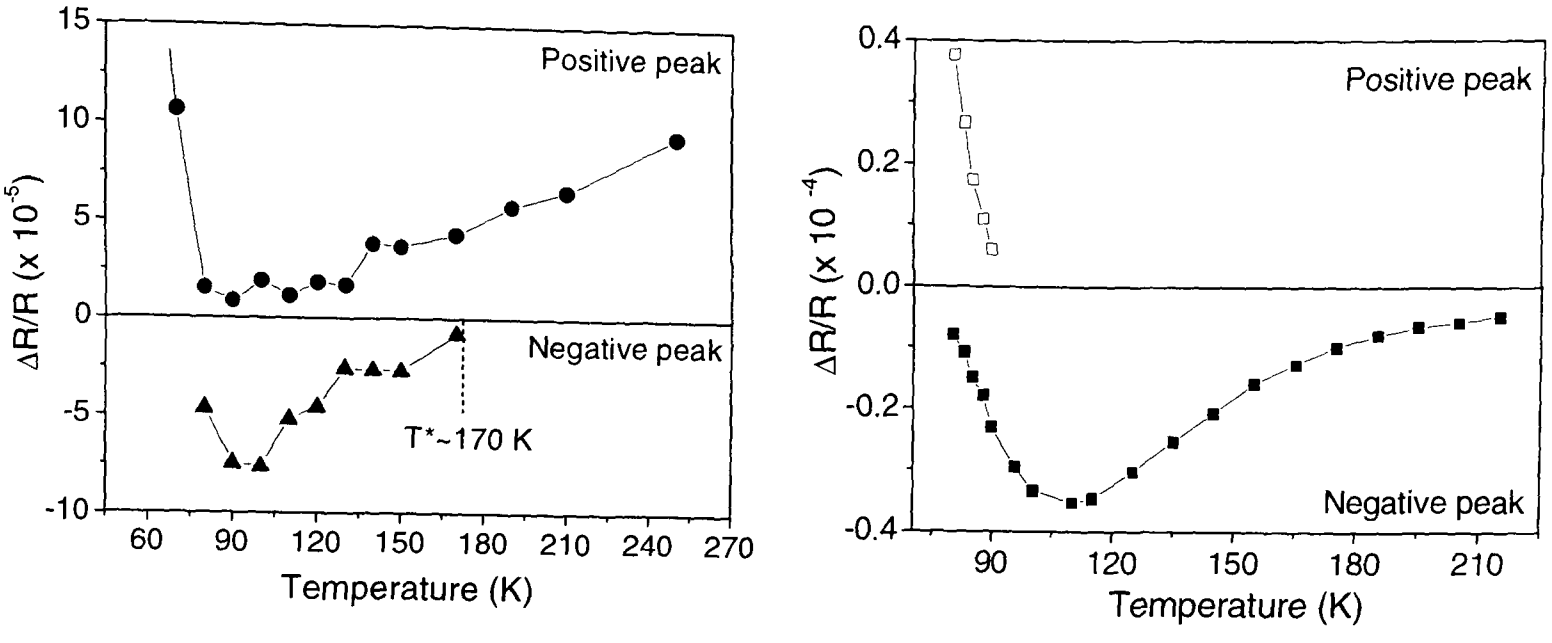

Figure 5.13: Temperature dependence of the magnitude of the negative and positive peaks in (a) BSCCO-2212 and (b) TBCO-2201 in the pseudogap phase.

excitation spectrum of BSCCO measured by angle-resolved photoemission spectroscopy [38, 39]. The transition between the normal and pseudogap states is even less sharp than the transition at T_c. However, we define T^* as the temperature at which the negative peak becomes observable in the induced response. This temperature is about 125K for the optimally-doped single crystals and about 170K for the optimally-doped thin films. The measured T^* are in good agreement with those determined from the generally accepted phase diagram [125, 126] for the doping dependence of T^*, as illustrated in Fig 5.14.

The initial TBCO-2201 dynamics above T_c is quite similar from that observed in BSCCO-2212, as shown in Fig 5.15. It is also characterized by a decrease in photo-induced reflectivity and a much faster relaxation dynamics with a decaytime of approximately 850fs. It is observed for temperatures above 73K, although it may be present at temperatures below this but obscured by the superconducting response. The negative magnitude peaks near 112K and then decreases as temperature increases up to 225K, the maximum experimentally accessible temperature. The temperature dependence of

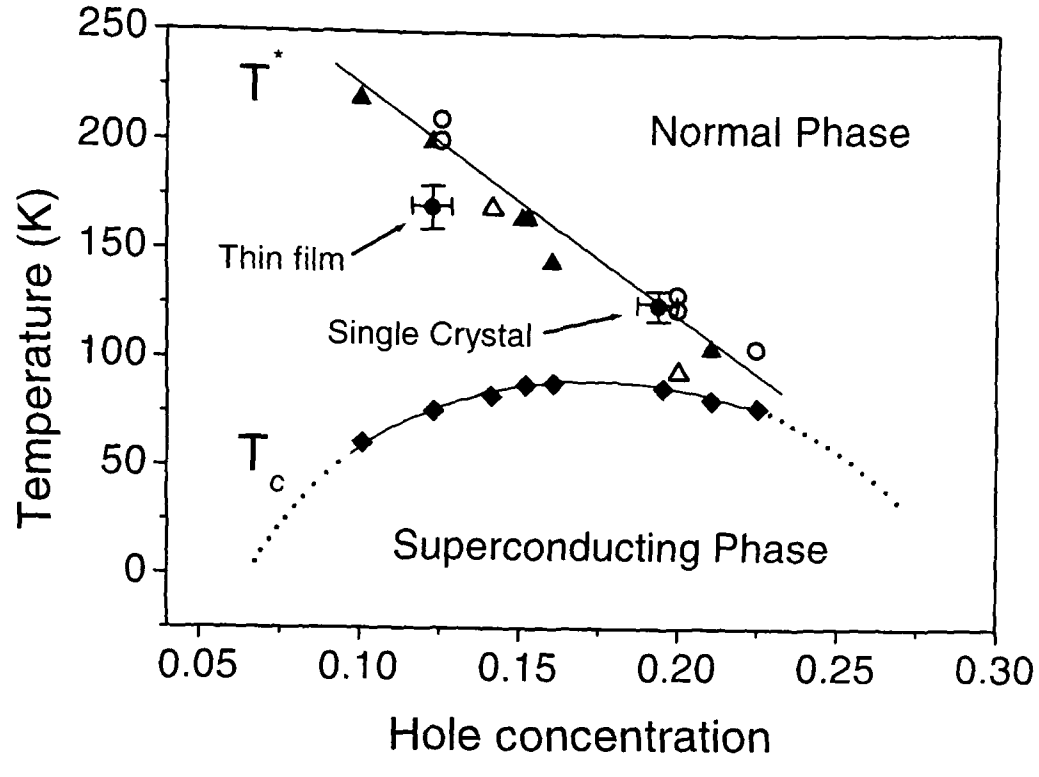

Figure 5.14: Phase diagram of BSCCO-2212 with the superconducting state below T_c, the pseudogap state between T_c and T* and the normal state above T*. The T* values are from transport [126] (solid triangles), ARPES [39] (open triangles) and NMR [125] (open circles) measurements. Our two T* data points for the thin film and the single crystal are represented in solid circles.

the peak magnitude in Fig 5.13b is very similar to that of the negative component in BSCCO-2212 (cf. Fig 5.13a) related to the pseudogap state and it is therefore likely that this component is also associated with the pseudogap. However, in the TBCO-2201 case, firmly ascribing this component to the pseudogap is made difficult by our lack of higher temperature measurements showing dynamics in the normal state and by the lack of general studies of the pseudogap state in TBCO-2201. Further experiments are ongoing to clarify this issue with detailed measurements on doping dependence.

At temperatures in the neighborhood of T*, the BSCCO-2212 response is found to consist of both a normal state, *positive* $\mathcal{R}$, and a pseudogap state component, *negative* $\mathcal{R}$, as for instance at 140K in Fig 5.12. This observation suggests that the pseudogap response does not simply arise from modified energy relaxation of the electronic system. This

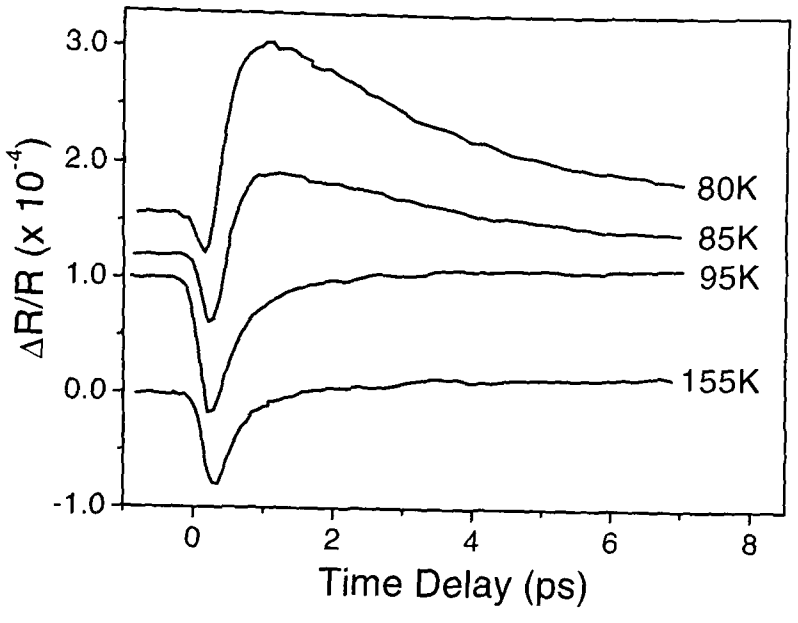

Figure 5.15: Photo-induced reflectivity of optimally-doped TBCO-2201 ($T_c = 82$K) in the pseudogap state. The responses have been offsetted for a clear presentation. The excitation density is 2μJcm^{-2}.

conclusion is further supported by the observation that the pseudogap state dynamics is much faster ($\lesssim$ 850fs) than in the normal state ($\gtrsim$ 1.5ps). This last observation is contrary to what would be expected due to the opening of a gap in the density of states. It is also in sharp contrast to the *reduced* scattering rates observed in both electrical and thermal conductivity measurements of BSCCO-2212 in the pseudogap phase [4]. From this, we conclude that the present optical experiment may modulate the electronic correlations responsible for the formation of the pseudogap, i.e. within the scenario of pseudogap formation arising from preformed pairs, photo-excitations would perturb the pair density (this issue will be discussed in more detail in section 5.6).

5.4 Normal State Dynamics

The high-temperature dynamics of BSCCO-2212 is shown in Fig 5.16. The normal state response rises within the temporal resolution, ~140fs, and then decays with a time constant of about 1.5ps to a long-lived background level. This response is very similar to

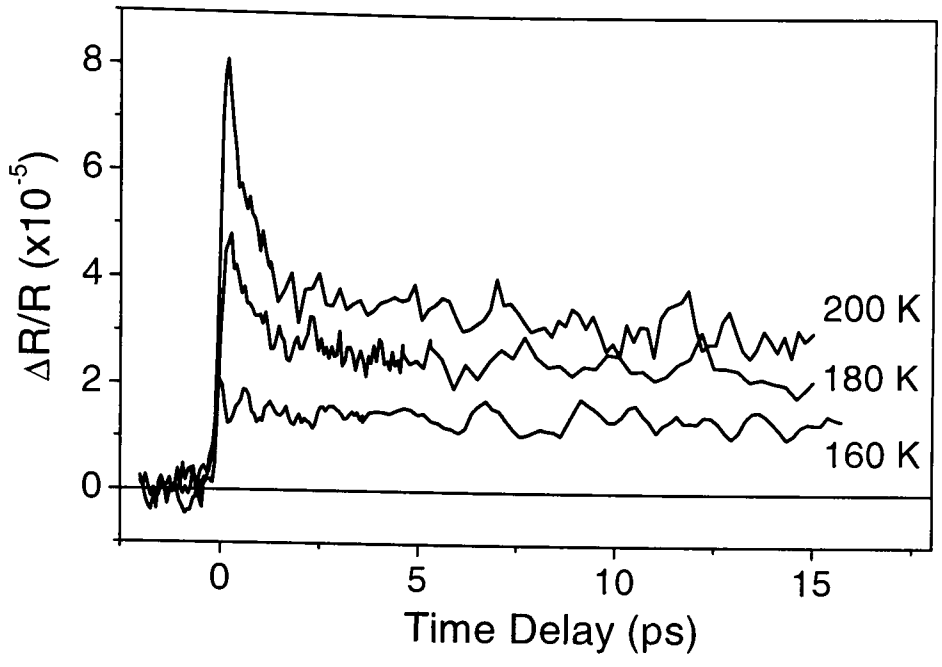

Figure 5.16: Dynamics of BSCCO-2212 in the normal state between 160 and 200K. The excitation density is $24\mu\text{Jcm}^{-2}$.

the room temperature reflectance measurements of BSCCO-2212 thin films reported by Brorson et al. [96], which has been interpreted in terms of ultrafast energy relaxation via electron-phonon scattering. The dynamics is also similar to the one measured in metals such as Ag and can be interpreted in a similar manner with Fermi surface smearing[1] or more generally with a two-temperature model with the energy relaxation being due to the cooling of a thermalized electronic system by phonon emission [6].

All previous ultrafast optical measurements of high-temperature superconducting cuprates in the normal phase have also suggested that the response closely resembles that of a normal metal, although the magnitude of the fast component in our measurements is temperature dependent, as shown in Fig 5.13a. As far as we know, this temperature dependence has not been observed in standard metals, however the temperature dependence may be due to a remnant pseudogap response.

Virtually any kind of energy relaxation with a two-temperature model will give a similar response as the one observed in Fig 5.16. However, Allen [88] argued that the

[1] The Fermi surface smearing is described for ultrafast experiments on metals in section 4.1.

relaxation rate in a Fermi metal is linear in temperature. In other words, a very useful experiment would have been to measure the temperature dependence of the relaxation rate in the normal state to determinate if the normal state of HTSC is fermionic or not. Unfortunately, we do not have enough data at the moment to clarify this issue.

The investigation of the electron-phonon coupling constant λ from the Allen theory [88] would also be very interesting for BSCCO-2212 (cf. section 4.2). This work would require numerical simulations of a non-linear differential equation fitting the $\Delta R/R$ dynamics at room temperature [94, 95, 130]. Tunneling spectroscopy experiments reported strong electron-phonon interaction in the a-b plane of BSCCO-2212, with λ values between 1.9 and 2.7 [131].

5.5 High-Excitation Density Measurements

Many measurements have been reported at low-excitation power on a range of HTSC materials, but little systematic work has been carried out at high-densities where the photo-excited population can significantly disrupt the superconducting condensate. To date, all our measurements at relatively low intensities in our laboratory and elsewhere have shown a near-linear density dependence with no indication of the expected saturation of the signal with increasing photo-excitation due to the complete destruction of the condensate.

In order to investigate the strong perturbation limit, we performed experiments using a high-power Ti:Sapphire amplifier[2]. In Fig 5.17 we present the BSCCO-2212 results obtained in the superconducting state at a lattice temperature of 10K for different excitation intensities. Below a density of $0.63 mJcm^{-2}$, the dynamics is similar to that observed in the low-perturbation limit with a linear intensity dependence of the signal magnitude and

[2]For this experiment we used an amplified Ti:Sappire 1kHz regenerative laser at the Rutherford Appleton Laboratory described in section 3.2.3.

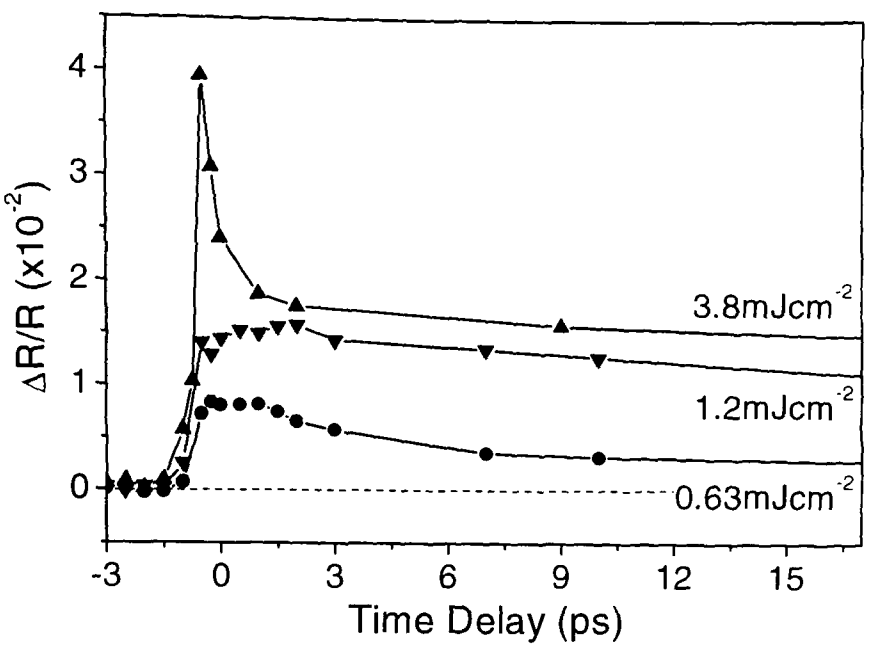

Figure 5.17: Dynamics of BSCCO-2212 at 10K and at high intensities with a change of dynamics at 3.8mJcm^{-2} corresponding to the complete suppression of the condensate.

of the relaxation rate. Above 1.2mJcm^{-2}, the dynamics is totally different with a fast, resolution-limited positive peak, a fast relaxation time of approximately 1ps and a large long-lived component. Thus, the data show a clear transition from the superconducting state dynamics below 0.63mJcm^{-2}, similar to what is observed in our laboratory, to a behaviour closer to the one observed in the normal state above 1.2mJcm^{-2}. The change of dynamics between the two regimes is represented in Fig 5.18 with the difference $\mathcal{D}$ between the peak value at zero delay and the signal at 40ps. The threshold, as defined by a dramatic change in the time evolution of the dynamics, occurs at an excitation density of approximately 1.2mJcm^{-2}. Just before the threshold, the intensity dependence of the relaxation time is modified. Indeed, the relaxation time starts increasing again, as shown in Fig 5.17, where the dynamics at 1.2mJcm^{-2} has a larger relaxation time than at lower density.

We interpret the threshold as the excitation density responsible for the complete depletion of the superconducting condensate by a laser pulse. Concerning the observed slowing

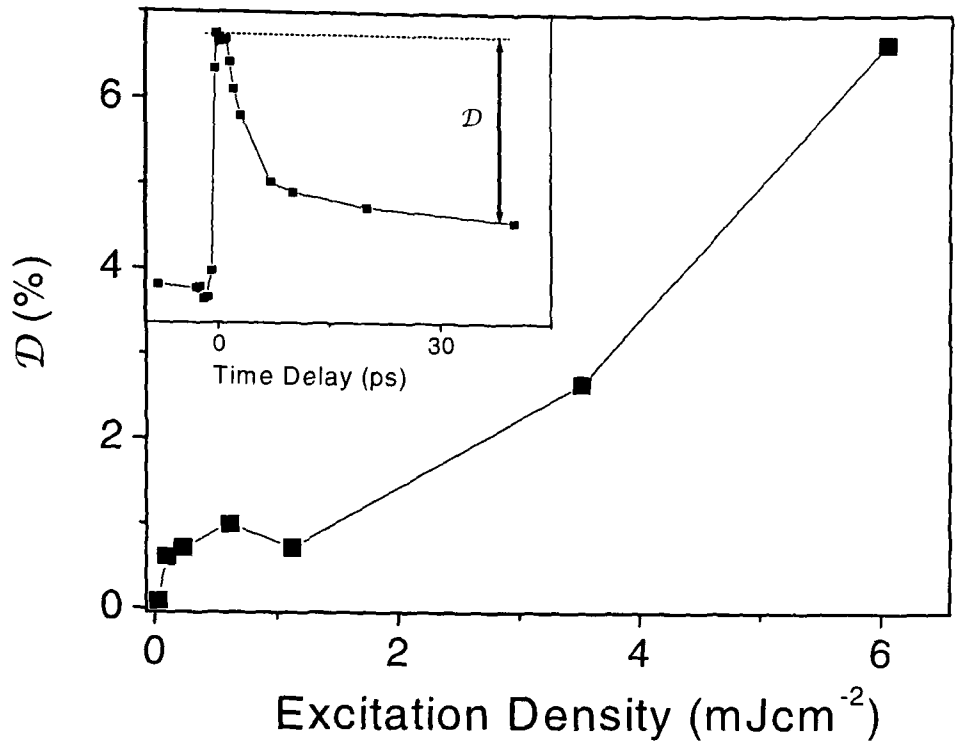

Figure 5.18: Excitation density dependence at 10K of the difference $\mathcal{D}$ between the peak value and the signal at 40ps, as illustrated in the inset.

of the relaxation dynamics with increasing excitation density, although most of the laser energy goes into heating the lattice due to the strong electron-phonon interaction, the slowing cannot be explained simply by sample heating. Changes in the relaxation times apparent in the different responses may be related to a number of possible sources as hot phonon effects [132] or modifications of quasiparticles scattering arising from the loss of the condensate phase.

In summary, quasiparticle dynamics in the strong non-equilibrium regime is markedly different from that in the weak perturbation limit. We measured the first observation of a change of regime corresponding to the complete depletion of the condensate. The change of regime in the superconducting response occurs at an excitation density over 50 times higher than the densities used in the experiments reported in previous sections. This observation and the linear intensity dependence at low-excitation densities indicate that we are far from breaking all the superconducting pairs in the low-excitation density regime in our laboratory and that we only weakly perturb the condensate density, 1/50

(2%) of the superconducting fraction at the maximum.

5.6 Superconducting Correlations and Critical Fluctuations

The change in sign of $\mathcal{R}$ between the superconducting and the pseudogap states observed in BSCCO-2212 and TBCO-2201 leads to some interesting questions. In the pseudogap state, there are several indications that we may observe the dynamics of electronic correlations associated with the pseudogap instead of quasiparticle dynamics. An important point is that the relaxation time of the pseudogap response, ~0.5ps, is a factor three faster than in the normal state. This speeding up of dynamics is contrary to expectation on the opening of a gap in the density of states and also inconsistent with the decrease in low-energy quasiparticle scattering observed in measurements of the electrical conductivity [4] in the pseudogap state. The different signs of the superconducting, pseudogap and normal response are also an indication that the pseudogap behaviour is not simply due to modified quasiparticle scattering or to modified energy relaxation of the electronic system. Moreover, at temperatures in the neighborhood of T*, $\mathcal{R}$ is found to consist at the same time of both a normal state (*positive* $\mathcal{R}$) and a pseudogap state (*negative* $\mathcal{R}$) components, as shown for instance in Fig 5.12 at 140K for BSCCO-2212. These observations suggest that we may be modulating the electronic correlations responsible for the pseudogap as already stated in section 5.3. In a scenario where preformed pairs exist, we could think of photo-excitations perturbing the pair density. A weaker form of this statement would be to say that optical excitations are modulating the correlations responsible for the pseudogap.

It is also important to emphasize that the pseudogap dynamics in BSCCO and the dynamics of TBCO above T_c are different from the pseudogap dynamics reported for

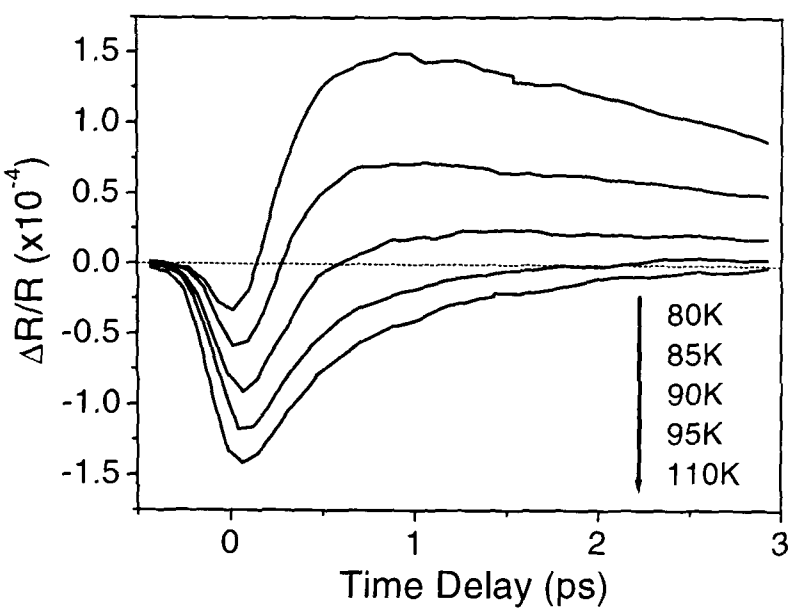

Figure 5.19: Dynamics of TBCO-2201 between 80 and 110K focused on the rise edge. The excitation density is $2\mu\text{Jcm}^{-2}$.

YBCO in section 4.5. In particular, in the BSCCO/TBCO compounds, the $\mathcal{R}$ dynamics in the pseudogap state has an opposite sign than in the superconducting state.

Perhaps the most novel behaviour seen in these measurements is in the region of the superconducting transition temperature. The amplitude of the negative signal related to the pseudogap does not peak until T_c + 28K for BSCCO, as shown in Fig 5.13. Thus there is a clear offset between T_c[3] and the temperature at which $|\mathcal{R}|_{max}$ reaches 50% of its maximum magnitude in the pseudogap state. This offset, 8K in TBCO-2201 and 5K in BSCCO-2212, cannot be explained by sample inhomogeneity.

On closer inspection of the data obtained just above T_c, as illustrated for TBCO-2201 in Fig 5.19, it is possible to separate a negative pseudogap component from a positive component reminiscent of the superconducting dynamics. The substraction of the response at 110K ($|\mathcal{R}|_{max}$ maximum) to that at 95K is shown in Fig 5.20 and indicates that a difference persists up to 95K, i.e. 13K above T_c. At such high temperatures, there is no static superconducting coherence and therefore we speculate that this component arises from superconducting critical fluctuations with a finite lifetime of about 1.5ps.

[3] T_c is defined here as the 50% point of the resistive or magnetic susceptibility transition.

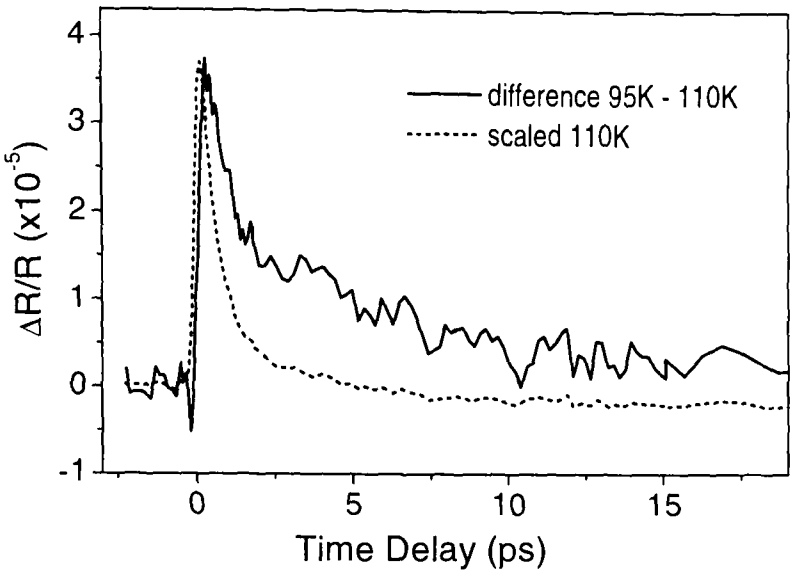

Figure 5.20: Difference between the dynamics at 95 and at 110K of TBCO-2201 and the scaled dynamics at 110K for comparison.

The changeover in dynamics near T_c is therefore not sharp but extends to temperatures above T_c, in a similar way as the superconducting anomaly observed in heat capacity measurements [5]. This observation is consistent with the presence of dynamic superconducting correlations above T_c in the manner of a Kosterlitz-Thouless-Berezinski (KTB) transition. This conclusion is consistent with the interpretation placed on recent measurements by terahertz optical conductivity in YBCO by Corson et al. [69] (cf. section 2.8).

The ultrafast optical response will continue to have superconducting character as long as the fluctuations of the phase correlations occur on a timescale comparable with the lifetime of the superconducting signal. In other words, the ultrafast spectroscopy gives a lower limit of the phase correlation time τ. At 95K, we measured a decay time of the superconducting signal of 1.5ps for TBCO-2201. Corson et al. [69] reported values of approximately 0.5ps at 85K and 0.2ps at 92K for BSCCO-2212, which are slightly lower than our measurements for TBCO-2201. Unfortunately, no work has been done on TBCO-2201 yet.

The interpretation of critical fluctuations in the HTSC is still a matter of considerable

debate. Heat capacity measurements [3] indicate that the critical behaviour is strongly dependent on the material and doping level. BSCCO-2212 with doping levels equivalent to ours show that the effect of critical fluctuations drops off on a temperature scale very similar to the positive $\mathcal{R}$ component dynamics. However, optimally-doped YBCO-123 shows very little evidence of fluctuations above T_c. This difference with YBCO may explain why critical fluctuations have not been observed in the ultrafast optical response of this material.

The nature of the critical fluctuations is also thought to vary from more BCS-like in overdoped material to more BEC-like (Bose-Einstein Condensation) in underdoped material [3]. Another recent suggestion is that the dimensionality of the fluctuations might change from 3D-like at low energies to 2D Kosterlitz-Thouless-like at higher energies [69]. We believe that the ability to time-resolve dynamics on timescales shorter than the superconducting fluctuations and the sensitivity of the ultrafast optical response to quasiparticle dynamics means that we have a unique probe of the critical fluctuations in these materials with which to address these issues.

5.7 Spectral Dependence of the Signal

Almost all measurements have only studied the quasiparticle response at a few discrete wavelengths making interpretation of the probe interaction rather uncertain. In order to address this issue, we have carried out measurements using a femtosecond white light continuum generated by an amplified ultrafast laser[4].

Fig 5.21 shows the spectral dependence of the BSCCO-2212 room temperature response acquired using interference filters to select different probe wavelengths from the continuum. We were able to detect signals from 1.38 to 2.48eV (from 900 to 500nm),

[4]For this experiment we used an amplified Ti:Sappire 1kHz regenerative laser at the Rutherford Appleton Laboratory described in section 3.2.3.

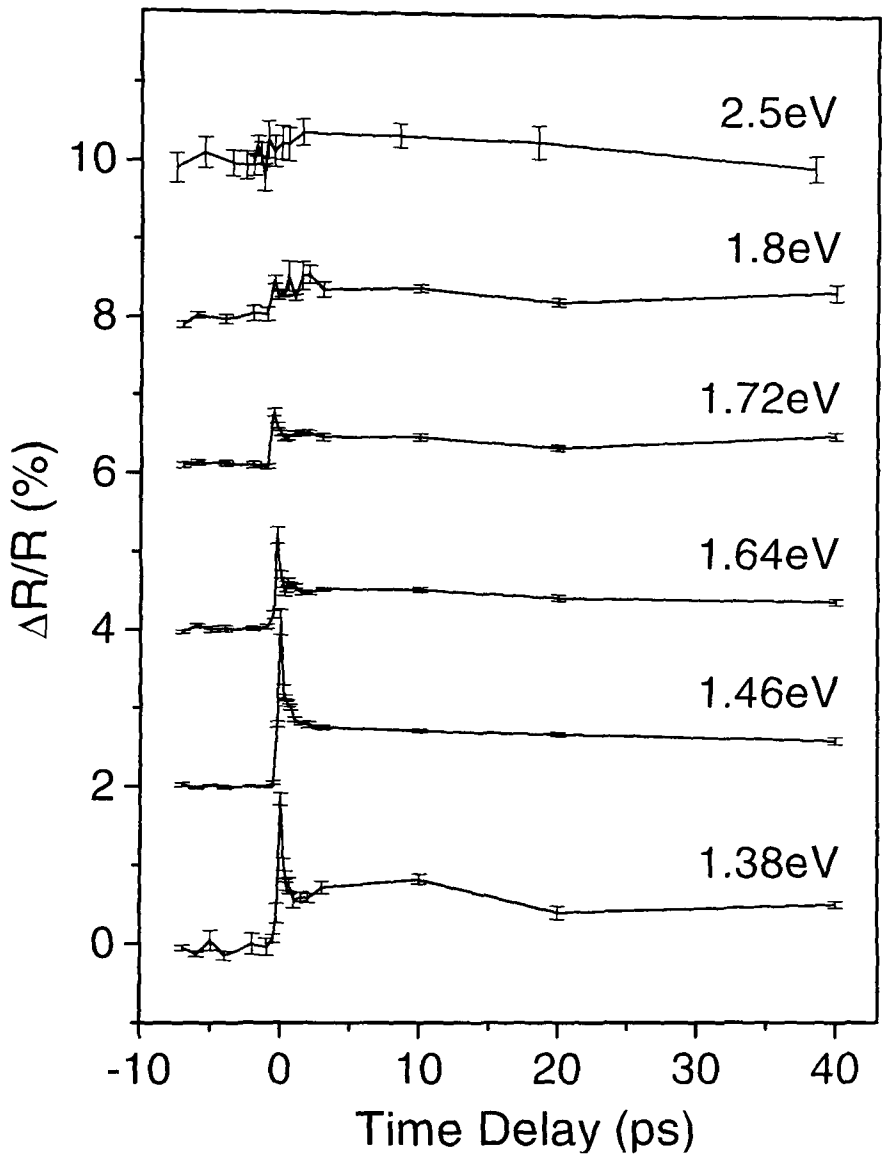

Figure 5.21: Photo-induced reflectivity of BSCCO-2212 at room temperature in function of the probe wavelength. The excitation density is $0.24 mJcm^{-2}$.

but a complete spectral dependence will require significantly better experimental performance as we were limited by the bad signal-to-noise ratio. While these signals do not in themselves give a definitive picture of the probe mechanism in BSCCO, early indications are that there is a sign change in the photo-induced signal near 2.48eV (500nm). The responses extracted at small wavelengths should be treated with some care, however the general shape seems to indicate that both the initial transient and long-lived component are stronger at longer wavelengths, which is consistent with a Drude-dominated response. In particular, no derivative-like feature has been observed in the neighbourhood of 2eV, which would indicate a Fermi surface smearing effect as expected from previous experiments[5]. Nevertheless, further work has to explore the spectrum in more detail at both shorter and longer wavelengths in order to better identify the probe mechanism.

5.8 Dynamics on the Nanosecond Timescale

In both BSCCO-2212 and TBCO-2201, a long-lived component has been observed, as presented in Fig 5.3b. The temperature dependence of the magnitude of this component for TBCO-2201 is shown in Fig 5.22; the signal is measured at -3ps, i.e. at 12ns, the laser pulse separation. We observed a strong increase of the signal when the temperature goes to zero, a relatively broad peak at T_c and another broad peak centered at about 185K.

A long-lived component has been observed in the ultrafast optical response of YBCO-123 [116, 117], but there is no evidence of the divergence at very low temperature and of the peak at 185K. The low temperature divergence is also present in BSCCO-2212, as illustrated in Fig 5.23.

Two possible explanations have been proposed to explain the long-lived component: sample heating or long-lived electronic excitations which are possibly localized (cf. section 4.6). In the heating model, the photo-induced reflectivity is given by $\mathcal{R}_{long-lived} \propto T_L$,

[5] See for details the conclusion of the Chapter 4.

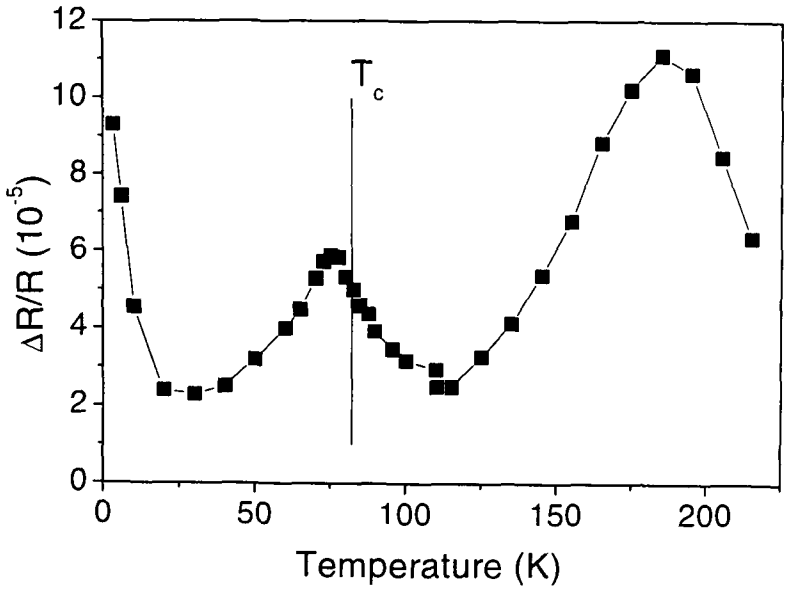

Figure 5.22: Temperature dependence of the long-lived component of TBCO-2201 measured at 12ns after zero delay.

where T_L is the lattice temperature. In this model T_L is determined by the total heat capacity; the whole energy of one pulse is assumed to contribute to the heat capacity and the lattice temperature is assumed to go back to its equilibrium value before the next pulse. As the heat capacity goes to zero with decreasing the temperature to zero, T_L increases considerably at low temperature, as shown with the solid curve in Fig 5.23. The fit reproduces well the data for $T < 20K$ and hence suggests that the long-lived component may be due to sample heating. The failure of the model to explain the behaviour at higher temperatures might be an indication that the reflectivity is not proportional to the sample temperature near T_c, or that another effect might be responsible for the long-lived component at higher temperature such as long-lived electronic states [116, 117]. The divergence at low temperature has never been observed in YBCO-123.

The peak at 185K may be related to the pseudogap temperature, as T* in TBCO-2201 is expected to be similar to the value for BSCCO-2212[6]. Unfortunately the lack of measurements in the pseudogap phase of TBCO-2201, e.g. by ARPES, prevents us from firmly relating this peak to T*.

[6]We measured a pseudogap temperature T* of 170K for BSCCO-2212 thin films (cf section 5.3).

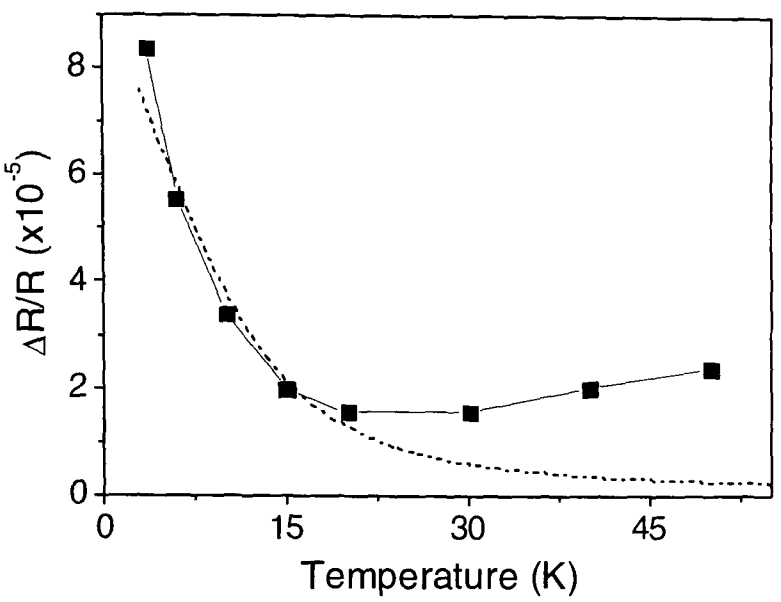

Figure 5.23: Temperature dependence of the long-lived component of BSCCO-2212 measured at 12ns after zero delay. The fit is from a lattice heating model considering the decrease of the heat capacity at low temperature.

5.9 Discussion

In order to interpret the YBCO ultrafast measurements, Kabanov et al. [53] developed an extension of the Rothwarf-Taylor model, first proposed to describe the dynamics of BCS superconductors. This model considers the quasiparticle-pair system to be in thermal equilibrium with phonons of energy higher than 2Δ. The relaxation of $\mathcal{R}$ is then due to the cooling of the combined system by the anharmonic decay of high-energy phonons. In an s-wave superconductor, this leads to a temperature independent relaxation rate for $T \lesssim \Delta/k_B$. Kabanov et al. [53] concluded that YBCO is an s-wave superconductor from the temperature independence of the relaxation rate (cf. Fig 5.8). The BSCCO/TBCO relaxation data presented here cannot be explained in this way due to the strong temperature dependence of $\tau_{1/2}$.

In this model the determining step in the pair formation is the decay of phonons of energy higher than 2Δ into phonons of lower energy. In the case of a noded gap the model predicts a divergence of $|\mathcal{R}|_{max}$ at low temperatures due to the availability

of low-energy quasiparticle states. In the case of an s-wave gap, the divergence at low temperature observed in BSCCO and TBCO could be obtained in the Kabanov model when the energy density per unit cell deposited by the incident pump laser pulse ε_I goes to zero, which is not realistic. In this s-wave model with a realistic value for ε_I, the strong temperature dependence of $\tau_{1/2}$ would imply an unreasonably small value for the superconducting gap, smaller than 5meV. Indeed, a good approximation of the anharmonic lifetime of a phonon of energy E_{ph} is given by [133] :

$$\Gamma_o(1 + 2 \cdot N(E_{ph}/2)) \tag{5.1}$$

where

$$N(E_{ph}/2) = 1/(e^{\frac{E_{ph}}{2k_BT}} - 1) \tag{5.2}$$

is the Bose-Einstein population of phonons with half the energy of the original phonon. In Fig 5.24 we present a fit of the form $A + BN(\Delta)$ to the temperature dependence of the relaxation rates in BSCCO-2212. From the fit, we obtained very small values of Δ, 3.3meV for BSCCO and 4.5meV for TBCO, and very small values of the A/B ratio, $\sim$1/20 for BSCCO and $\sim$1/10 for TBCO, instead of the expected ratio of 1/2. Therefore these results cannot be reconciled with the s-wave model.

In general, the strong temperature dependence of the dynamics at low temperatures is much easier to understand in terms of a noded gap. An s-wave gap places a lower limit on the energy of excitations which can be involved in pair formation and hence a lower energy limit on the excitations required to conserve the energy and the momentum in the formation of pairs from quasiparticles. Instead, the temperature dependence stems from the confinement at low temperatures of the quasiparticles near gap nodes, where scattering rates are observed to be low in a range of other experimental techniques [134]. In a predominantly d-wave superconductor, as the temperature decreases the non-equilibrium quasiparticles are confined closer to the nodes, which leads to a reduced phase-space for

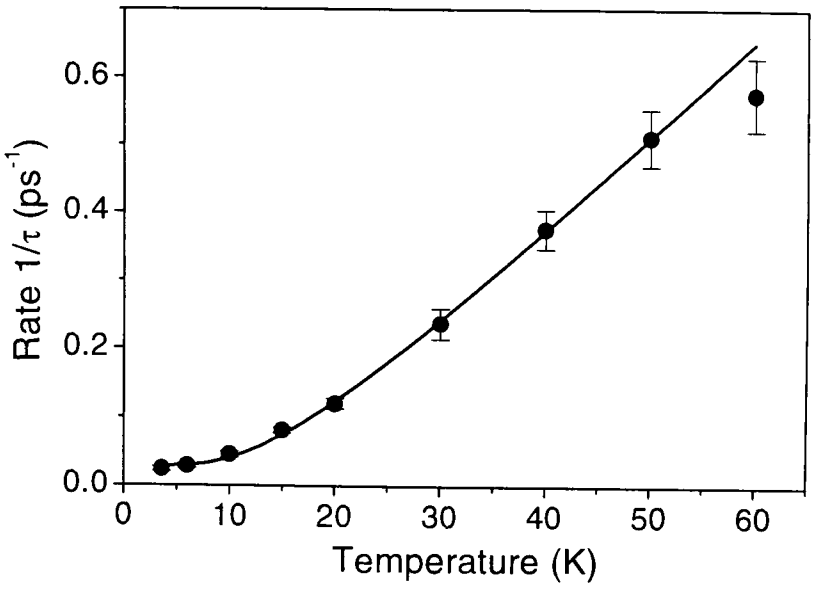

Figure 5.24: Temperature dependence of the decay rate of $\mathcal{R}$ in BSCCO-2212 with a fit from the anharmonic phonon lifetime ($E_{ph} = 3.3$meV).

scattering and also concentrates the quasiparticles in the directions where the overlap between paired and unpaired states is the smallest [52]. In this way, the slowing of the decay with decreasing temperature down to the lowest temperatures fits well into the model of the signal following the pair re-formation from unpaired carriers in the nodes of the d-wave superconductor. Feenstra et al. [52] (cf. section 4.3) have calculated the pair re-formation rate for a d-wave gap, assuming it is limited by phonon emission. These calculations do not show a strong enough temperature dependence to explain the present results. However, the calculations do show that carrier cooling by phonons is much faster than re-formation of pairs, which suggests another possible model where pair formations from quasiparticles in opposite nodes involves the scattering of a quasiparticle in one of the other two nodes. The excess energy given to the quasiparticles by the formation of a pair is then quickly removed by the emission of phonons. Further theoretical work is ongoing to test this hypothesis.

We have tried to model the re-formation of the broken pairs using a range of models. Bimolecular recombinations of quasiparticles in the presence of a thermal population of quasiparticles provides a natural explanation, as two quasiparticles are needed to form a

Cooper pair. In general, the re-formation of pairs requires the emission of a phonon[7] and in the standard model of quasiparticles dynamics in the BCS superconductors, i.e. the Rothwarf-Taylor model, the phonons and quasiparticles come into thermal equilibrium and the rate of the re-formation of pairs is limited by the *lifetime* of the phonons. Kabanov et al. rejected a d-wave model for YBCO because they predicted that the number of quasiparticles excited in the initial stages of the dynamics will diverge at low temperature. This prediction is based on the quasiparticles and phonons coming into thermal equilibrium and therefore our results suggest that this does not occur. This is supported by the much larger number of phonons available for the condensate re-formation with a d-wave gap. If this is the case, then the re-formation of the condensate will not be limited by the phonon lifetime but instead by the *rate* at which quasiparticles interact. In this case, the recombination rate will be given by :

$$\frac{\partial \Delta N_{QP}}{\partial t} = -\Gamma([\Delta N_{QP} + N_{QP}^{thermal}]^2 - [N_{QP}^{thermal}]^2) \tag{5.3}$$

where $N_{QP}^{thermal}$ is the thermal population of quasiparticles and ΔN_{QP} is the non-equilibrium population of quasiparticles. The solution to this equation has two forms of limiting behaviour: when $\Delta N_{QP} >> N_{QP}^{thermal}$ the dynamics will follow a bimolecular decay and when $\Delta N_{QP} << N_{QP}^{thermal}$ the dynamics will follow a mono-exponential decay. We therefore expect the dynamics to change from bimolecular to mono-exponential as temperature increases. The general solution of the equation is:

$$\Delta N_{QP}(t) = \frac{2N_{QP}^{thermal}}{[1 + \frac{2N_{QP}^{thermal}}{\Delta N_{QP}(0)}]e^{t/\tau} - 1} \quad with \quad 1/\tau = \Gamma N_{QP}^{thermal} \tag{5.4}$$

and in the bimolecular limit the solution is:

$$\Delta N_{QP}(t) = \frac{\Delta N_{QP}(0)}{1 + \Gamma \Delta N_{QP}(0)\ t} \tag{5.5}$$

[7] A phonon or more generally a low energy boson.

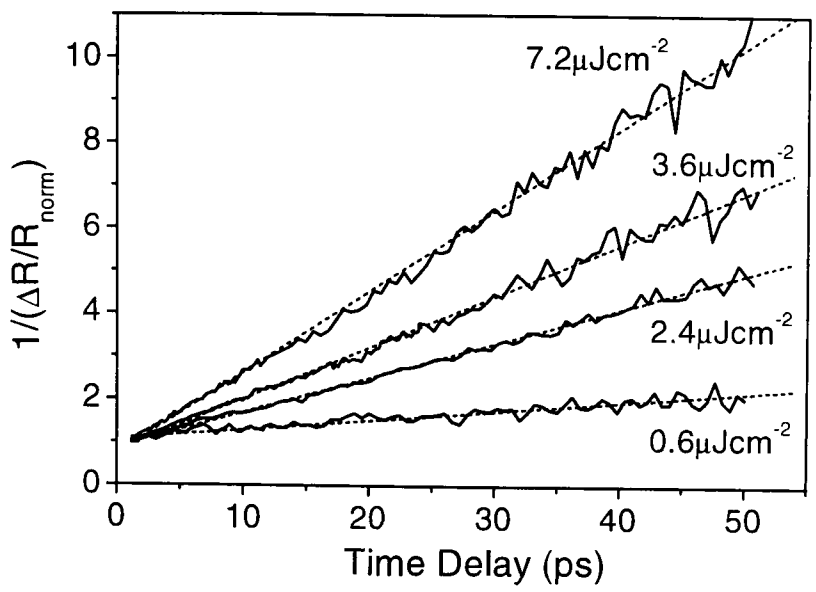

Figure 5.25: $1/(\Delta R/R_{normalized})$ dynamics of BSCCO-2212 for different excitation densities at 4K. The inverted dynamics can be well fitted with a bimolecular linear function.

The bimolecular model fits well the dynamics particularly at temperature below 20K. In Fig 5.25 is plotted $1/\mathcal{R}$ which should be linear in time in this model at 4K. The fitting parameters of the bimolecular model are $N_{QP}^{thermal}/\Delta N_{QP}(0)$ and the recombination rate $1/\tau$. In Fig 5.26, we present the temperature dependence of the fitting parameters for optimally-doped BSCCO-2212 thin film and the excitation density dependence is shown in Fig 5.27. The quadratic temperature dependence of $N_{QP}^{thermal}/\Delta N_{QP}(0)$ in Fig 5.26a is in agreement with the non-equilibrium quasiparticle fraction measured in penetration depth experiments [128]. Moreover, the temperature dependence of the recombination rate $1/\tau$ reproduces the relaxation rate $1/\tau_{1/2}$ observed in BSCCO-2212 and shown in Fig 5.8.

Comparing the intensity dependence of the dynamics with that expected from the model is complicated by laser induced heating. The bimolecular model expects to have the parameter $\Delta N_{QP}(0)/N_{QP}^{thermal}$ proportional to the excitation density and the recombination rate $1/\tau$ independent of the excitation density. However, as shown in Fig 5.27, the bimolecular fit to our results as a function of the power shows the contrary,

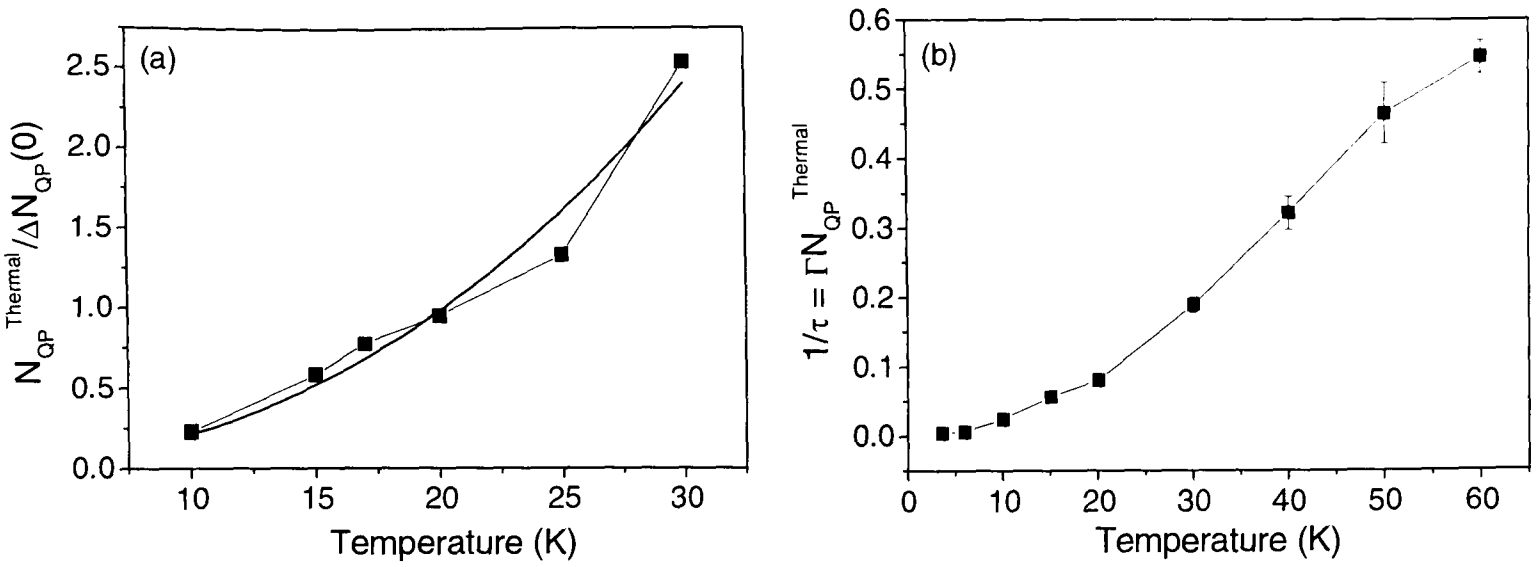

Figure 5.26: Temperature dependence of (a) the inverted non-equilibrium quasiparticle fraction $N_{QP}^{thermal}/\Delta N_{QP}(0)$ and (b) the recombinaison rate $1/\tau$ from the bimolecular model for optimally-doped BSCCO-2212 thin film.

$\Delta N_{QP}(0)/N_{QP}^{thermal}$ is proportional the excitation density only at low densities and $1/\tau$ is increasing with power. A possible explanation for this behaviour is that $N_{QP}^{thermal}$ is actually dependent on the excitation density. Another explanation would be that Γ is sensitive to the excitation density. Consequently, the intensity dependence in Fig 5.27 may well be consistent with the model, if the sample heating is included.

As pair formation requires two unpaired carriers, the bimolecular decay would give a natural explanation of the relaxation process in HTSC. The model explains the change in the form of the dynamics at 20K and fits the temperature dependence of the decay rate; however, a more elaborate model needs to be developed to explain the intensity dependence.

We could imagine having two different situations depending on the lattice temperature and the HTSC compound. In one case, pair recombination and reabsorption are fast compared to the anharmonic phonon decay. Thus, on a sub-100fs timescale the photo-excited quasiparticles and the high-frequency phonons are in near-thermal equilibrium and described by a common temperature. The relaxation rate of the quasiparticles is dominated

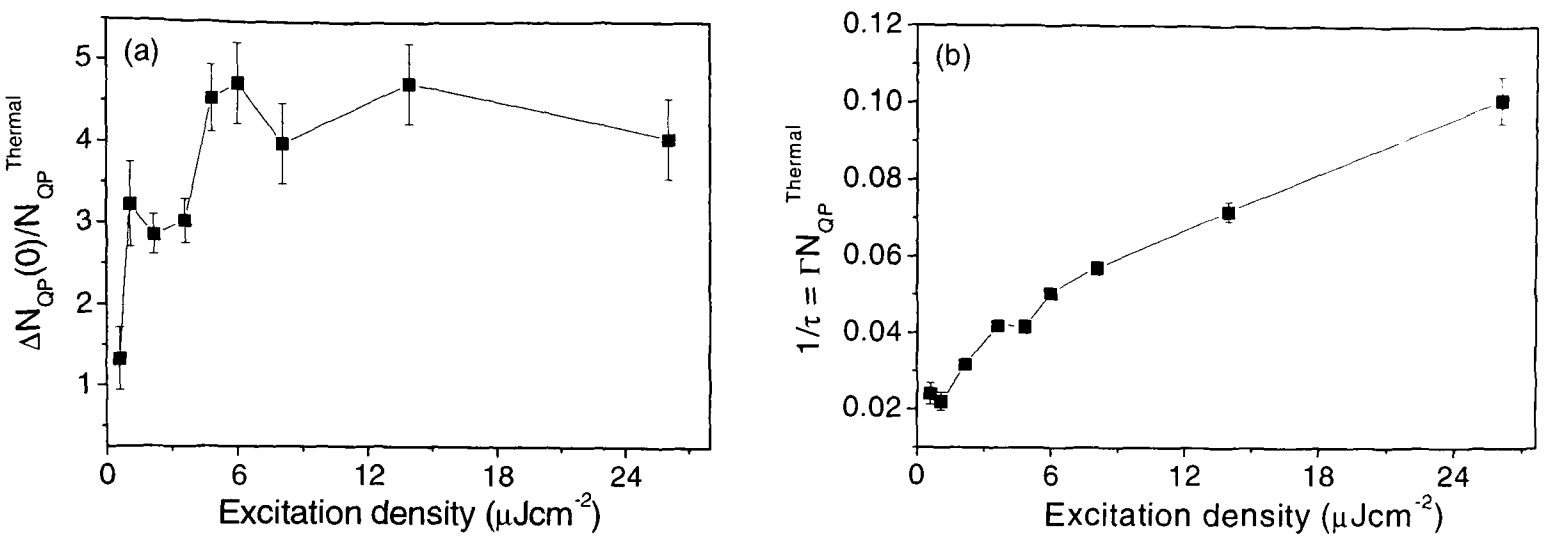

Figure 5.27: Excitation density dependence of (a) the non-equilibrium quasiparticle fraction $\Delta N_{QP}(0)/N_{QP}^{thermal}$ and (b) the recombinaison rate $1/\tau$ from the bimolecular model for optimally-doped BSCCO-2212 thin film.

by the energy transfer from high-frequency to low-frequency phonons, as successfully described in the Kabanov model [53] for YBCO-123. In another case, the recombination time is longer than the anharmonic phonon decay time and thus the photo-excited quasiparticles and the high-energy phonons have two distinct temperatures. The relaxation time of the quasiparticle density is therefore governed by the bimolecular recombination process, as described above. Demsar et al. [135] reported measurements of the mercury compound $HgBa_2Ca_2Cu_3O_{8+\delta}$ (HBCO-1223), where they also observed a linear temperature dependence of the decay rate. They used a similar bimolecular model with a theoretical expression of the recombination time τ_{rec} from the bimolecular model and an expression of the relaxation time τ_R from the anharmonic phonon decay model. They found a crossover in function of temperature between the two different times τ_{rec} and τ_R at about 70K. At low temperature, where the number of photo-excited quasiparticles is large, τ_{rec} is larger, whilst at higher temperature τ_R becomes larger. Another important result they theoretically predicted is that τ_{rec} is proportional to $exp(\Delta/k_B T_{ph})$ where T_{ph} is the temperature of the high-energy phonons and Δ is the size of the superconducting

gap. From tunneling experiments, the superconducting gap Δ is estimated to be 20meV for YBCO-123, 30meV for BSCCO-2212 [23] and 62meV for HBCO-1223 [135]. Hence, the fact that the crossover between the two regimes is proportional to $exp(\Delta/k_B T_{ph})$ would explain why a change of dynamics and a linear decrease of the decay rate $1/\tau_{1/2}$ are observed with decreasing temperature from around 70K in HBCO-1223, around 20K in BSCCO-2212 and not observed in YBCO-123 at least until 4K.

The temperature dependence of the amplitude of $\mathcal{R}$ in BSCCO and TBCO in the superconducting phase can be understood in terms of pair breaking induced by the exciting laser pulse with $\mathcal{R}$ being proportional to the number of broken pairs as discussed in section 5.2. In this case, the time dependence of $\mathcal{R}$ is expected to follow the recombination of non-equilibrium quasiparticles to reform pairs. The decrease of the signal magnitude towards zero at T_c corresponds to the closure of the superconducting gap. That would be certainly the case in conventional superconductors. However, the pseudogap i.e. the persistence of an energy gap above T_c, with strongly-correlated but phase incoherent pairs substantially changes the picture. It is indeed not possible to attribute all the temperature dependence of the response to quasiparticle dynamics. The superconducting phase is attributed to a macroscopic coherence of the superconducting pairs and, in most recent theories the pseudogap refers to preformed incoherent pairs. The issue is now the nature of the ultrafast response in these circumstances.

One possibility comes from the assumption introduced in section 5.6 that photoexcitation modulates the electronic correlation in the pseudogap phase. Instead of quasiparticle dynamics, we might be seeing in the pseudogap state the dynamics of pseudogap correlations. In this picture, the number of pairs as well as the coherence of the pairs are modulated in the superconducting state as in conventional superconductors. Below T_c, the probe mechanism would be Fermi surface smearing or a modulation of the Drude reflectivity or lattice distortions, whilst the relaxation would follow the relaxation of

high-energy phonons (Kabanov model) or the recombination rate (bimolecular model) depending on the material and the temperature. The signal observed in the pseudogap phase would arise from phase excitations and hence from a mechanism different from that in the superconducting state, which would explain the totally different responses and the coexistence of the distinct peaks at T_c and at T^*.

Another possibility is that the pseudogap state response is related to quasiparticle dynamics, as in the superconducting state. Because we observed two very distinct responses in sign and behaviour in the superconducting and pseudogap state, the two responses have to be attributed to two distinct HTSC properties. In the incoherent preformed pair model for the pseudogap state, the onset of the superconducting phase is due to the coherence of the preformed pairs. Therefore, in this model we have to be somehow sensitive to the coherence of the pairs and be able to modulate their coherence. There are different possible probe mechanisms which could be sensitive to the pair coherence in the superconducting state. Lozovik et al. [136] argue that the imaginary part of the dielectric function depends on the symmetry of the superconducting order parameter and on the coherence of the pairs, and therefore, the interband transitions are responsive to the superconducting coherence. A second possibility is that the photo-induced reflectivity arises from the Drude component of the reflectivity, in which case the probe mechanism would also be sensitive to the coherence of the pairs. Indeed, the coherent pairs have no scattering in contrast with the incoherent pairs and therefore, a modulation of the coherence will change the plasma frequency.

5.10 Conclusion

The study of ultrafast dynamics in the HTSC has concentrated mostly on YBCO-123, which is unfortunately complicated by the presence of CuO chains. Using time-resolved reflectivity, we have successfully measured the dynamics of low-energy electronic exci-

tation for the first time in the mono-layer system TBCO-2201 and we have presented the first systematic study of the bi-layer system BSCCO-2212. The ultrafast response of TBCO-2201 is remarkably similar to that of BSCCO-2212 but shows important differences from the YBCO-123 response. We obtained very reproducible results from sample to sample and from both single crystals and thin films in the case of BSCCO-2212.

The optical response is sensitive to the electronic ground state with clear distinctions between the normal, pseudogap and superconducting ground states. The results reported here for BSCCO and TBCO confirm the previous observations in YBCO that the ultrafast optical response probes the behaviour of low-energy gap excitations in the superconducting phase. But they also reveal a number of important new features: a linear temperature dependence of the relaxation rate in the superconducting phase from 4K up to 60K and an intermediate phase between T_c and T*, corresponding to an energy gap in the spectrum of electronic excitations i.e. to the pseudogap.

It is possible to model the superconducting state response as being proportional to the number of broken pairs via the dynamics of non-equilibrium quasiparticles. We proved that we are in the near-equilibrium limit and hence that we are only weakly modulating the superconducting condensate. The temperature dependence of the relaxation rate in the superconducting phase cannot be reconciled with an isotropic gap but can be understood in terms of the dynamics of quasiparticles near the nodes in a superconducting d-wave gap. This effect may arise from scattering from low-energy excitations, a strong candidate being the branch of low-energy acoustic phonons.

The BSCCO-2212 and TBCO-2201 dynamics can be reproduced with a mono-exponential decay from 20K up to T_c, but need a more complex model at lower temperature. A bimolecular model has the advantage of fitting well the dynamics at low temperature and of explaining the linear temperature dependence of the relaxation rate. This model is motivated by the idea that the re-formation of the condensate may be

limited by the rate at which quasiparticles interact and not by the phonon lifetime as in YBCO.

Several observations indicate that we may observe in the pseudogap state phase correlation instead of quasiparticles dynamics, which would explain the totally distinctive response of the superconducting, pseudogap and normal states. We also observed the effect of short-lived superconducting fluctuations in the dynamics at temperatures up to 13K above T_c in TBCO-2201. The superconducting character extending to temperatures above T_c is possibly due to a Kosterlitz-Thouless-Berezinski-like phase transition. There is no evidence of critical behaviour in BSCCO-2212 in the neighborhood of T_c, as reported in the case of TBCO-2201.

A divergence of the long-lived component has been observed in BSCCO and TBCO at very low temperature. This feature can be easily explained in term of equilibrium sample heating. However, our new measurements cannot make the distinction between the bolometric and the non-bolometric model to explain the divergence at T_c observed in YBCO, BSCCO and TBCO.

New experiments need to be carried out to focus on unresolved issues concerning BSCCO and TBCO. Probably the most important one is to measure the ultrafast dynamics of strongly underdoped and overdoped samples in order to observe the changes in the pseudogap and superconducting state as a function of the doping. Next, a systematic study of the wavelength dependence of the probe beam still needs to be investigated in order to find out the origin of the probe mechanism, which will be very helpful to develop models concerning different issues in the interpretation of the results. Experiments on thin films with variable thickness would definitively decide what is the origin of the long-lived component. The variation of the repetition rate between laser pulses with a cavity dumper would separate the transient heating (non-variable with the repetition rate) from the equilibrium heating (variable with the repetition rate), which will be helpful to un-

derstand the effect of the excitation density. Finally, experiments on other HTSC, such as Bi and Tl-compounds but with a different number of layers, as well as on other cuprates would be very useful for the general interpretation of the ultrafast results. In particular, the understanding of the form of the superconducting signal relaxation, apparently going from a bimolecular decay to a mono-exponential decay, seems to depend on the size of the superconducting gap.

Chapter 6

High-Resolution Study of Dynamics of $YBa_2Cu_3O_{7-\delta}$

6.1 Introduction

Transmission and reflection measurements of optimally-doped and underdoped YBCO-123 thin films have given very similar results to those published by Stevens et al. [116] and Kabanov et al. [53]. In this chapter I will present only new results on the rising edge dynamics i.e. during the onset of $\mathcal{R}$. The increase of the photo-induced reflectivity at times $<$ 100fs corresponds to the modulation of the superconducting condensate by the breaking of a small fraction of Cooper pairs (cf. chapter 5). All previous time-domain studies on HTSC probing the ultrafast optical response reported resolution-limited rising edge dynamics, with time resolution $\geq$ 100fs [9, 53, 96, 98, 116]. In the present investigation, 20fs laser pulses were used and for the first time we have been able to time-resolve the initial dynamics of YBCO-123.

As described in chapter 4, after the pump laser pulse excites electron-hole pairs, the photo-excited quasiparticles thermalize among themselves. In this thermalization pro-

cess, the common scattering channels are electron-electron and electron-phonon. Electron-electron scattering is the most effective channel at the beginning of the avalanche process, with electron-phonon relaxation becoming important when the quasiparticle energy is reduced to 30-50meV. Scattering of carriers by local antiferromagnetic fluctuations (electron-spin scattering) may also contribute to the avalanche process. The energy scale associated with spin fluctuations is measured to be of the order of 50meV [137, 138]. Therefore this channel could also be relevant in the second part of the relaxation although it has not been considered so far in the literature.

Our results will give new insights into the general understanding of the dynamics occurring in the first few hundred femtoseconds after photo-excitation. In the first part of this chapter we present time-resolved measurements on the early stage dynamics ($\leq$100fs), together with a model explaining the new data. In the second part, we present observations of coherent phonon oscillations in YBCO-123. As explained in more detail in section 4.4, Mazin et al. [13] proposed a model in which both the oscillatory and the non-oscillatory part of the ultrafast response arises from coherent phonon oscillations. We present here a discussion of this model based on measurements of the rising edge dynamics.

6.2 Rising Edge Dynamics in YBCO

We measured the dynamics of YBCO-123 thin films in reflection for sample temperatures in the range of 10 to 120K with a low-excitation density of $0.12\mu Jcm^{-2}$ and a time resolution of 35fs. The experimental set-up used here is slightly different from the one used in the two previous chapters and is described in detail in section 3.2.2. The signal-to-noise ratio was lower in this experiment due to increased laser noise and the degenerate pump-probe configuration. Consequently, we had to use a longer lock-in time constant (5s) for each time delay and we had to average 10 consecutive scans at each temperature.

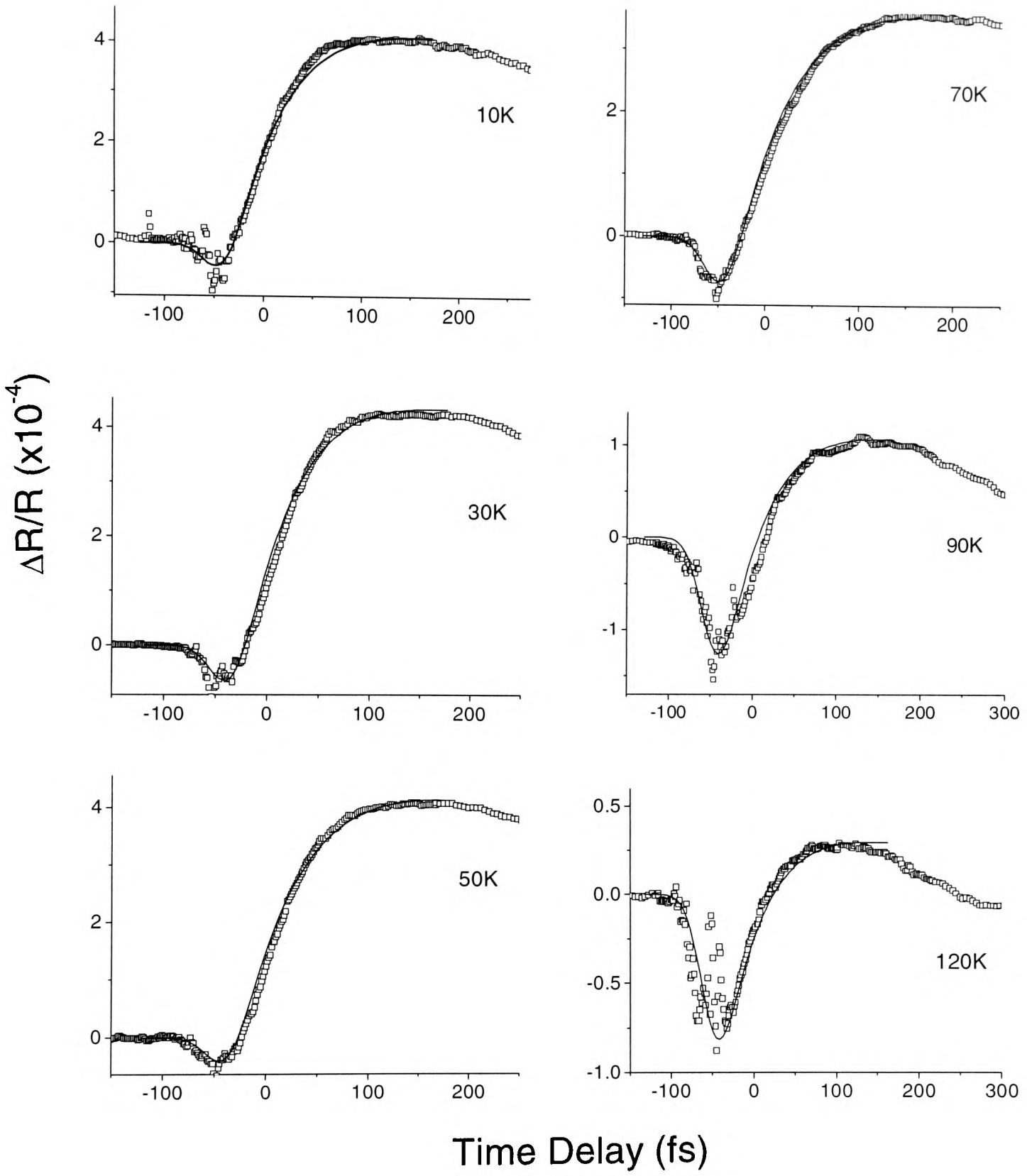

Figure 6.1: Photo-induced reflectivity of optimally-doped YBCO-123 thin film focused on the initial dynamics with a resolution of 35fs. The fits are from a model composed of a negative and a positive exponential function as illustrated in Fig 6.2.

The results obtained at 10, 30, 50, 70, 90 and 120K are presented in Fig 6.1. All data display a small negative peak preceding the rising edge, with a constant time difference of ~150fs between the minimum of the negative peak and the maximum of the positive peak. The magnitude of the positive peak has a similar temperature dependence to that previously observed in YBCO-123 [53, 116], i.e. dropping approximately to zero at T_c with increasing temperature. On the other hand, the magnitude of the negative peak is temperature independent. The negative peak has not been observed in any published data up to date. The time difference between 10% and 90% of the peak value is ~90fs, meaning that the rising edge is not resolution-limited in this experiment. The longer timescale dynamics (up to 15ps) observed with the high-resolution experiment is identical to previously reported data. Indeed, the temperature dependence of the magnitude, relaxation time and long-lived component is very similar to that from previous experiments with ~140fs resolution (cf. section 4.2 or references [53, 116]).

6.3 Model for the Rising Edge Dynamics

As already stated in chapter 5, the increase of the photo-induced reflectivity when the pump pulse excites the sample is attributed to the modulation of the superconducting condensate by the destruction of a small fraction of Cooper pairs (cf. chapter 5). Subsequently, the relaxation of the photo-induced signal corresponds to the re-condensation of the pairs. The model which fits most successfully the entire temperature range consists of the sum of two exponential decays of opposite sign:

$$\mathcal{R} = \frac{\Delta R}{R} = E_p e^{-t/\tau_p} - E_n e^{-t/\tau_n} \tag{6.1}$$

convolved with a response function. The positive exponential function has an instantaneous rise time, and its decay constant τ_p is on the timescale of 1.5ps at low temperature with a divergence at T_c (cf. Fig 4.9 from reference [98]). The negative exponential func-

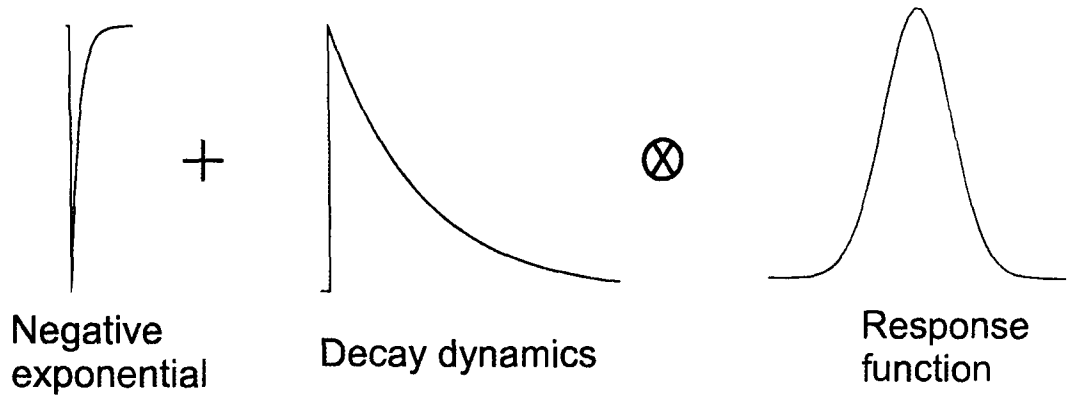

Figure 6.2: Model for the rising edge dynamics consisting of the sum of a fast negative and a longer positive exponential function. The result of the sum is then convolved with a gaussian function representing the time resolution of the experiment.

tion has also an instantaneous rise time but with a much faster decay τ_n. The response function is a gaussian with a 35fs FWHM corresponding to the temporal resolution and given by the autocorrelation of the pump and probe beams[1]. The different components of the model are illustrated in Fig 6.2 and the resulting fits to the dynamics are present in Fig 6.1. The physical justification of the two exponential functions will be presented below with a mathematically equivalent model. The parameters of the model are the magnitudes of the two functions, E_p for the positive exponential and E_n for the negative one, and the relaxation time of the negative exponential τ_n. The relaxation time τ_p of the positive component is known from an exponential fit to the longer timescale decay and hence it is fixed for the fitting.

The temperature dependence of E_p and E_n obtained from the fits are represented in Fig 6.3. Both components are approximately temperature independent up to ~60K; then the positive component decreases slowly to approximately zero at ~100K, and the same time the negative component decreases to $-3 \cdot 10^{-4}$. The decrease of the signals is centered at T_c, as shown in Fig 6.3. The fits give a temperature independent value of τ_n

[1] The autocorrelation has been measured at the sample, with an InGaP photodiode.

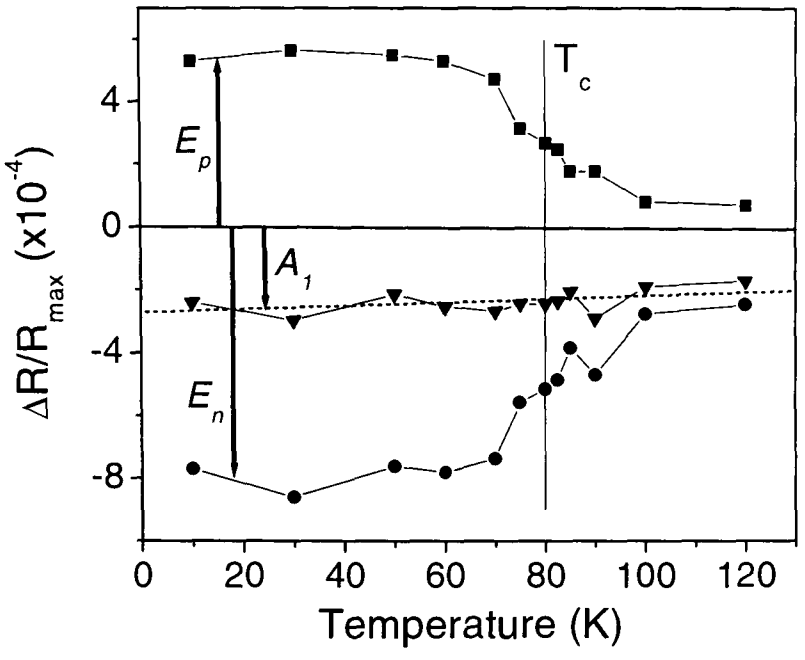

Figure 6.3: Temperature dependence of the magnitude E_p of the positive exponential (solid squares) and the magnitude E_n of the negative exponential (solid circles). The sum of the two opposite components is also represented (solid triangles).

= 55fs.

It is also clear in Fig 6.3 that the sum of the two magnitudes $E_p + E_n$ is temperature independent. This is equivalent to the condition:

$$\mathcal{R} = -A_1 e^{-t/\tau_n} + E_p(e^{-t/\tau_p} - e^{-t/\tau_n}) \tag{6.2}$$

with $E_n = A_1 + E_p$ and A_1 being temperature independent ($\sim$ -3·10^{-4}). In (6.2), the positive component has an exponential rise time with the time constant τ_n, instead of an infinitely short rise time as in (6.1). In other words, the time constant of the rising edge of the positive peak is the same as that of the relaxation of the negative component.

We can go a step further by separating the positive component into two parts, one related to the superconducting gap, following a BCS-like temperature dependence, and one related to the pseudogap and being temperature independent, as proposed by Kabanov et al. [53] for modelling the longer timescale response in YBCO-123. Therefore below T_c, the decay of the positive component is bi-exponential i.e. with the superconducting

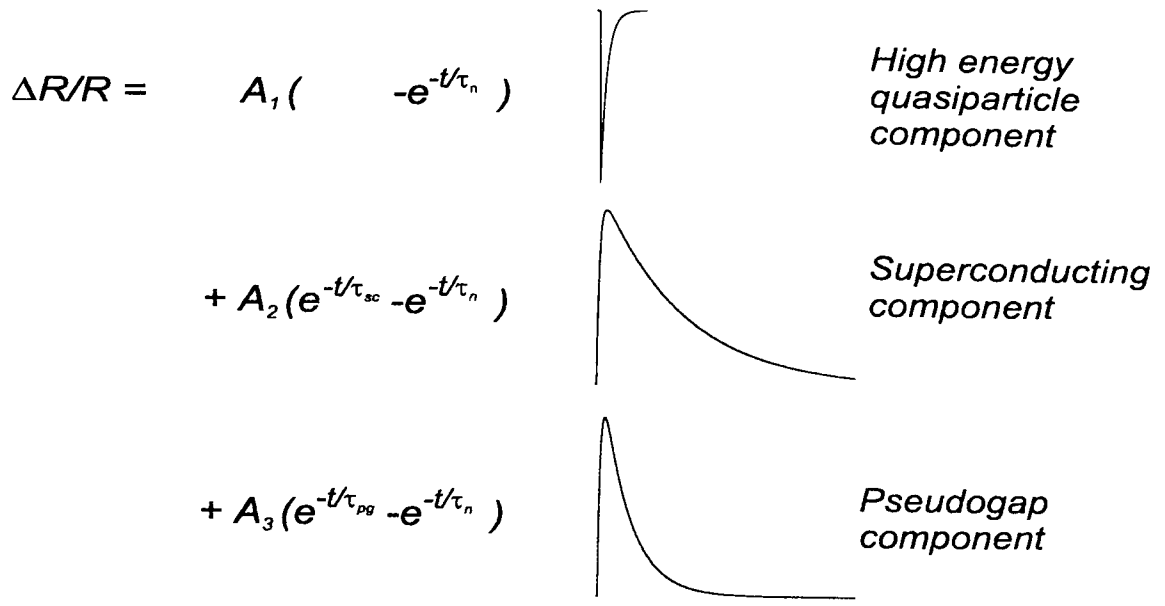

Figure 6.4: Photoinduced response model with the negative exponential component and the superconducting and pseudogap state components.

and pseudogap responses, while above T_c its decay is mono-exponential with only the pseudogap response. The photo-induced signal can be therefore written as

$$\mathcal{R} = -A_1 e^{-t/\tau_n} + A_2(e^{-t/\tau_{sc}} - e^{-t/\tau_n}) + A_3(e^{-t/\tau_{pg}} - e^{-t/\tau_n}) \tag{6.3}$$

In (6.3), the positive component E_p is separated into the superconducting response with the relaxation time τ_{sc} and the pseudogap response with the relaxation time τ_{pg}. The second and third term have the same rise time τ_n. From the measurements of Kabanov et al. [53], we used the temperature independent value of $\tau_{pg} = 0.5$ps, while $\tau_{sc} \simeq 1.5$ps from 4K to about 60K and then diverges at T_c.

To summarize, we can fit our measurements with the superconducting and pseudogap components observed previously on the longer timescale measurements, together with a new negative exponential component which is temperature independent in magnitude and in relaxation time. The three components are illustrated in Fig 6.4. Also, we observe that the rising edge of the superconducting and pseudogap components are well fitted with an exponential function with a time constant of 55fs.

We also tried to fit the data by constraining the rise time of the pseudogap and superconducting components to be different from the relaxation time of the negative exponential. Nevertheless, we noticed that the rise times cannot differ more than 15% from 55fs to give the same quality of the fits.

It is important to emphasize that the negative component observed here is qualitatively different from that observed in BSCCO-2212 and TBCO-2201, which has a much longer relaxation time on the order of 500fs and which is attributed to the pseudogap response (cf. section 5.3). A very weak, negative signal preceding the rising edge has also been observed in the superconducting state of BSCCO-2212 but no systematic study of this material has been made so far.

In this model, the rise time of the negative component is instantaneous and the rise time of the two other components follows the decay time of the negative component. From these observations, the most plausible explanation for the new fast negative component A_1 observed in YBCO-123 is that it corresponds to the lifetime of high-energy photo-excited quasiparticles. The probe beam can indeed interact with high-energy quasiparticles, which have not relaxed yet into states close to the Fermi energy. The 55fs rise time corresponds therefore, in this case, to the relaxation of photo-excited quasiparticles from energy levels above E_F by electron-electron or electron-phonon scattering. The temperature independence of the magnitude and relaxation time of the negative component in both the superconducting and pseudogap states is consistent with this explanation as the high-energy quasiparticles are not sensitive to the existence of a gap in the energy spectrum.

Nessler et al. [139] directly measured the hot electron lifetimes in BSCCO-2212 by interferometric two-photon time-resolved photo-emission technique as a function of temperature and energy above E_F. At 40K the photo-excited quasiparticle lifetimes goes from 10fs at 3eV above the Fermi energy to 50fs at 1.5eV. Unfortunately, they were not

able to measure the lifetime at energies lower than 1.5eV, where the hot quasiparticles in our experiment are located. Although Nessler et al. did not take measurements of YBCO-123, the quasiparticle dynamics well above the superconducting gap is expected to be quite similar in all HTSC. We can conclude therefore that our measurements are consistent with this picture of quasiparticle relaxation.

Nessler et al. could fit the hot electron lifetimes from 3 to 1.5eV with the function $(E - E_F)^{-2}$, which is the predicted dependence for a Fermi liquid metal. They assumed that this dependence is still valid at lower energies and hence that the normal state of HTSC behaves as a Fermi liquid. However, an extrapolation of their measurements would imply that the hot quasiparticle decay by electron-electron scattering from 1.5eV down to 370meV would take ~960fs, which is not observed in our measurements. In other words, from our data on the rising edge, we conclude that in fact it is not valid to infer Fermi liquid behaviour at energies lower than 1.5eV.

The negative component A_1 probes only one step in the relaxation of the high-energy quasiparticles down to the Fermi energy. Therefore, the total decay time has to be equal or longer than 55fs. However, we measured that both the relaxation of the negative peak and the rising edge of the positive peak have the same time constant $\tau_n \simeq 55$fs. This observation means that the complete relaxation of the hot quasiparticles has to be close to 55fs (within 15% as stated above). This is consistent with the quasiparticle avalanche process taking place during the hot quasiparticle relaxation. During this process, the quasiparticles dissipate their excess energy to other quasiparticles near E_F, Cooper pairs across 2Δ and phonons. The number of quasiparticles created as the result of a single photo-excited quasiparticle is approximated to be 150 [98]. The avalanche process implies that the characteristic time of each relaxation step decreases exponentially, explaining therefore why the total relaxation time is not much longer than 55fs.

We can also conclude from these measurements that the rise time of the supercon-

ducting and pseudogap signal is limited by the quasiparticle relaxation down to energies close to E_F and not by the destruction of the pair coherence or the breaking of a small fraction of pairs. From our data, we can indeed conclude that the modulation of the superconducting state by photo-induced quasiparticles has a time constant equal to or smaller than 55fs.

We could argued that the decay of the negative peak A_1 is itself limited by pair breaking. In this case, the negative component would not be associated with high-energy quasiparticles and the limiting step of the rising edge dynamics would be the breaking of pairs. However, this assumption is very unlikely, as both the magnitude and the relaxation time of the negative component is temperature independent, which is not plausible if the component is related to the pair breaking.

6.4 Coherent Phonon Oscillations

Coherent phonon oscillations have been observed previously in HTSC [113] by time-resolved spectroscopy (cf. section 4.5). It is proposed that coherent phonons are created by impulsive excitation as the ions are "pulled back" to their normal equilibrium positions when superconductivity is modulated. Such excited phonons are coherent in phase but only those with a period longer than the excitation time will oscillate. In pump-probe experiments, the excitation time corresponds to the pulsewidth of the excitation pulse.

We have observed coherent phonon oscillations in optimally-doped YBCO-123 thin films using 35fs excitation. Fig 6.5a presents YBCO dynamics measured at 30K and at low-excitation density. The data presented here is on a longer timescale (from 0.5 to 5ps) than in the first section of this chapter, and is consistent with previous YBCO-123 measurements [53, 116]. Distinct oscillations are now observed with a small amplitude, superimposed on the decaying profile and vanish at ~3ps. This is shown more clearly in Fig 6.6 where the oscillatory part of the dynamics is presented for several temperatures.

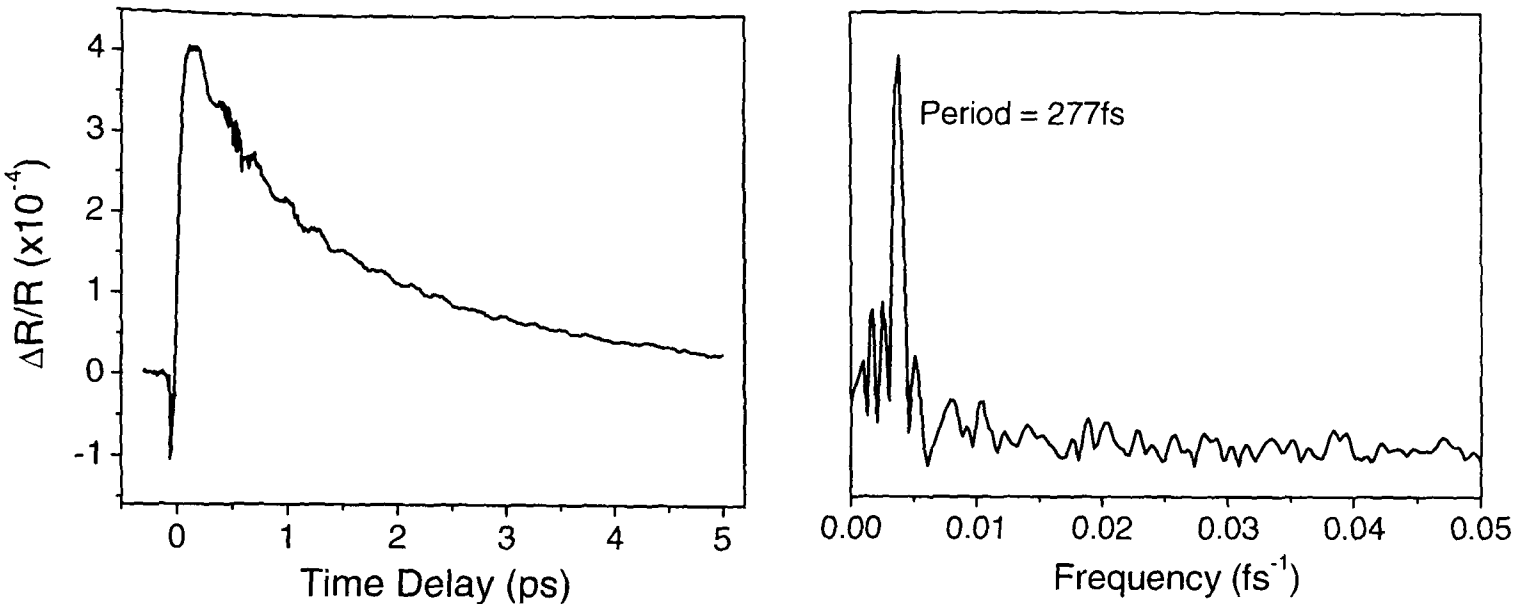

Figure 6.5: (a) Optimally-doped YBCO-123 thin film dynamics at 30K and at low excitation density with a time resolution of 35fs. (b) Fourier transform of the oscillatory part of the dynamics at 30K showing the main oscillation with a period of 277fs.

i.e. a fit of the non-oscillatory component has been substracted. There is clear evidence of oscillations for all the measured temperatures. A Fourier transform of the signal indicates that the main oscillation has a period of 277fs for all the measured temperatures, as shown for instance at 30K in Fig 6.5b. This period corresponds to the A-symmetry Ba phonon mode with an energy of $120cm^{-1}$, previously observed by Albrecht et al. [113]. There is no indication in our data of the second phonon mode observed by Albrecht et al. at $150cm^{-1}$.

In Fig 6.6 we also present fits to the oscillatory part of the dynamics with an oscillation period of 277fs. From 10 to 70K the fits are relatively good up to ~3ps, however, above 85K the fits are good only up to ~1.5ps. Albrecht et al. reported that the amplitude of the $120cm^{-1}$ phonon oscillations has a BCS-like temperature dependence. We do not have enough data to confirm this statement although the magnitude of the oscillations decrease with increasing temperature towards $T_c = 85K$. Above T_c, the magnitude seems to be constant.

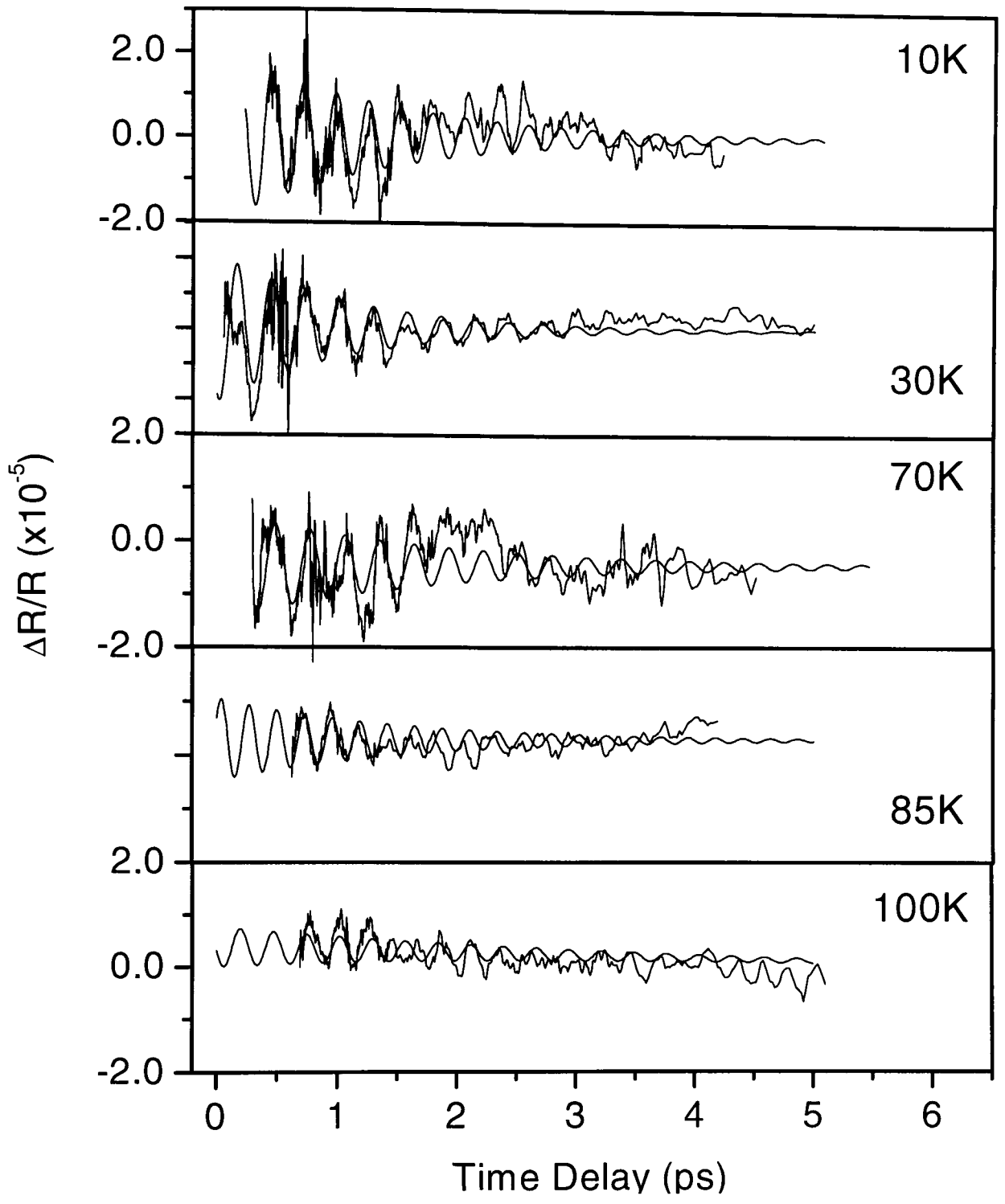

Figure 6.6: Oscillatory part of the optimally-doped YBCO-123 dynamics at several temperatures. The non-oscillatory part has been substracted to the response. The fits have a period of 277fs corresponding to the Ba phonon mode with an energy of $120cm^{-1}$.

Mazin et al. [13] attributed both the oscillatory and the non-oscillatory parts of the dynamics with the excitation of the coherent phonons. The Displacive Excitation of Coherent Phonon model (DECP) is explained in detail in section 4.5. In this model the non-oscillatory part of the signal corresponds to the adiabatic response of the lattice to the laser excitation. Our observation of a finite rise time has an important consequence for the model proposed by Mazin, as the relative magnitude of the oscillatory contribution to the photo-induced reflectivity depends on the ratio of the phonon period to the timescale of the pair breaking.

If the electronic dynamics driving the phonon displacement is of the form $n(t) = e^{-t/\tau_{sc}} - e^{-t/\tau_n}$ i.e. the underlying dynamics is expressed as the sum of two exponentials with τ_{sc} as the electronic relaxation time and τ_n as the rise time, then the DECP model gives the time dependence of the phonon coordinate and hence of the photo-induced response as the following:

$$Q(t) = \frac{\omega_0^2}{\omega'^2 + (1/\tau_{ph} - 1/\tau_{sc})^2}(e^{-t/\tau_{sc}} - e^{-t/\tau_{ph}}(\cos(\omega' t) + \frac{1/\tau_{ph} - 1/\tau_{sc}}{\omega'}\sin(\omega' t)) \quad (6.4)$$

$$-\frac{\omega_0^2}{\omega'^2 + (1/\tau_{ph} - 1/\tau_n)^2}(e^{-t/\tau_n} - e^{-t/\tau_{ph}}(\cos(\omega' t) + \frac{1/\tau_{ph} - 1/\tau_n}{\omega'}\sin(\omega' t))$$

where ω_0 is the free oscillation phonon frequency, $\omega' = \sqrt{\omega_0^2 - 1/\tau_{ph}^2}$ is the resonant phonon frequency and τ_{ph} is the phonon lifetime. From the previous section, we found that the rise time $\tau_n \simeq 55$fs, the decay time $\tau_{sc} \simeq 1.5$ps [53] and $\omega' = 2\pi/277$ fs^{-1}. The phonon lifetime $\tau_{ph} = 400$fs, taken from the Raman linewidth of the 120cm^{-1} mode [13]. The DECP response obtained from the Mazin formula (6.4) is plotted in Fig 6.7 for $\tau_n = 55$fs and compared with the result for $\tau_n = 350$fs, which was used by Mazin et al. The ratio of the oscillatory to the non-oscillatory signal is large for a small rise time, being 80% for $\tau_n = 55$fs and 15% for $\tau_n = 350$fs. In other words, when the timescale of the

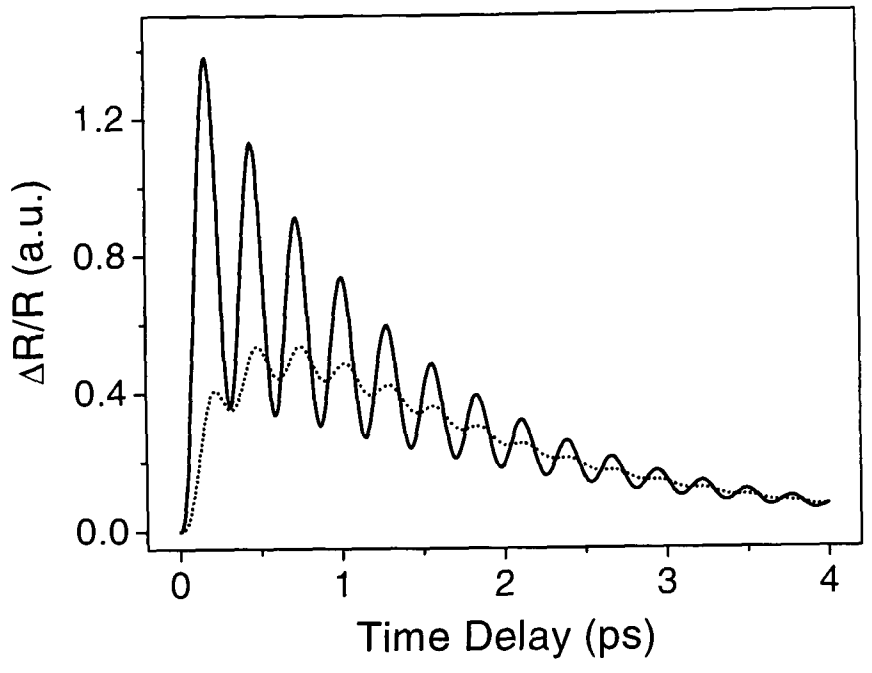

Figure 6.7: Photoinduced reflectivity from the model of Mazin et al. [13] with $\tau_{sc} = 1.5$ps, $\omega' = 2\pi/277$ fs^{-1}, $\tau_{ph} = 400$fs, and $\tau_n = 55$fs for the solid curve and 350fs for the dotted curve (equation 6.4).

excitation τ_n is smaller, the oscillatory part becomes more important. The reason for this dependence is that the shorter the timescale of the pair breaking τ_n with respect to the phonon period of 277fs, the larger the phonon oscillation effect.

In the measurements of YBCO-123 thin film presented in Fig 6.5a or from the data of Albrecht et al., the oscillatory component is relatively small, the ratio being approximately 10%. As we have seen in Fig 6.7, the ratio is very sensitive to τ_n. The value of τ_n used by Mazin et al. was the resolution-limited time of 350fs giving a dynamics similar to the observed data. However, the results presented here have shown that it is not valid any longer to interpret the dynamics as being solely due to the coherent phonon effect as proposed by Mazin et al.

The oscillatory part of the dynamics has not been observed previously in our laboratory by Stevens et al. [116] or by Kabanov et al. [53] with a time resolution of about 140fs. The reason is first that the oscillations are averaged because of the time resolution close to the phonon period, and second, that the rise time is not 55fs in this case. Indeed,

if the laser pulsewidth is longer than 55fs, then the rising edge dynamics is not limited by the relaxation of hot photo-excited quasiparticles down to the Fermi energy but by the laser pulse. Therefore, if the oscillatory part of the dynamics follows the Mazin model, which is very sensitive to the rise time, the oscillatory part would be 4 times smaller with a time resolution of 140fs than with a resolution of 35fs.

6.5 Conclusion

We have presented measurements using an ultrafast Ti:Sapphire laser with a pulsewidth of 20fs, giving a time resolution of 35fs. We resolved for the first time the rise time of the dynamics of YBCO obtaining a time constant of 55fs. We also measured a new component: a very fast negative peak attributed to the relaxation of high-energy photo-excited quasiparticles.

As the rising edge in the superconducting and pseudogap dynamics is also 55fs, we deduced that the total quasiparticle relaxation time down to states close to the Fermi energy is not much longer than 55fs and hence that the lifetime of the negative component is the slowest step in the relaxation of the quasiparticles. Another consequence is that the rising edge of both the superconducting and pseudogap response are limited by the high-energy quasiparticle relaxation and therefore that the pair breaking in the superconducting state occurs with a time constant faster than 55fs.

An important conclusion from our measurements is the demonstration that the Mazin model cannot explain the origin of the complete dynamics in YBCO-123. Indeed, with a rise time of 55fs the oscillatory part of the dynamics in the DECP model is too large with respect to the non-oscillatory part.

Chapter 7

Femtosecond Spectroscopy on detwinned YBCO single crystals

While a number of groups have reported ultrafast measurements of $YBa_2Cu_3O_{7-\delta}$ (YBCO-123), it has been difficult to interpret the data and to some extent, measurements reported by different researchers are in conflict [9, 97, 110]. All these studies have disregarded the high degree of twinning present in the a-b plane (cf. section 3.5.4). We report here the first measurements of the ultrafast response of detwinned YBCO-123 single crystals in which the in-plane anisotropy is revealed.

A new signal, which has been obscured in all previous thin film experiments, is observed for the probe electric field $\underline{E} \perp \underline{b}$, where $\underline{b}$ is the crystal axis parallel to the CuO chains (cf. YBCO-123 crystal structure in Fig 2.2). Comparing the two contributions, we find the new signal to be sensitive to the superconducting gap, whilst the signal for $\underline{E} \parallel \underline{b}$ appears to be sensitive to the pseudogap. The first part of this chapter presents the ultrafast response of detwinned YBCO-123 single crystals in which the dynamics for $\underline{E} \parallel \underline{b}$ and for $\underline{E} \perp \underline{b}$ have been separately identified [12], together with a discussion regarding the previous thin film measurements and the validity of the Kabanov model [53].

The second part of this chapter concerns the symmetry of the superconducting state. Most of the theoretical and experimental evidence available to date indicates a predominantly d-wave symmetry, although there is still some inconsistency on this issue, in particular from the ultrafast measurements of Kabanov et al. [53]. In principle, it is possible to probe the superconducting symmetry by measuring the angular dependence of the long-lived component: the temperature dependence of the amplitude of this component shows a thermally-activated behaviour (cf. section 4.6), with the activation energy being the energy gap [116].

The YBCO samples used in this investigation were single crystals produced by flux growth. After annealing in an oxygen atmosphere, they exhibit a transition temperatures of 92.5K, as measured by ac susceptibility. The single crystals have an estimated thickness of 200 to 400μm. The crystals were detwinned by applying a uniaxial stress of $\backsim$10MPa in the a-b plane along one of the crystal axes at 350°C in flowing oxygen at 1Bar, as described in detail in section 3.5.4.

Time-resolved optical pump-probe measurements were carried out under the same conditions as described in chapter 5 with a time resolution of 140fs. Using a computer-controlled half-wave plate, we adjust the polarization of the probe beam i.e. the direction of $\underline{\mathrm{E}}$ in the a-b plane. All measurements were made with an excitation density of 2.4μJcm^{-2}, a photon energy of 3eV for the pump beam and 1.5eV for the probe beam.

7.1 Anisotropy of the Reflectivity in the a-b Plane

The single crystals studied in this work have a typical anisotropy ratio of the reflectivity defined by $R_{\underline{\mathrm{E}}\|\underline{\mathrm{b}}}/R_{\underline{\mathrm{E}}\|\underline{\mathrm{a}}}$ of 3:1 after detwinning. The angular dependence of R is illustrated in Fig 7.1. The orientation of the crystal is defined in the detwinning process: the stress direction corresponds to $\underline{\mathrm{a}}$, as $(\underline{\mathrm{a}}) < (\underline{\mathrm{b}})$.

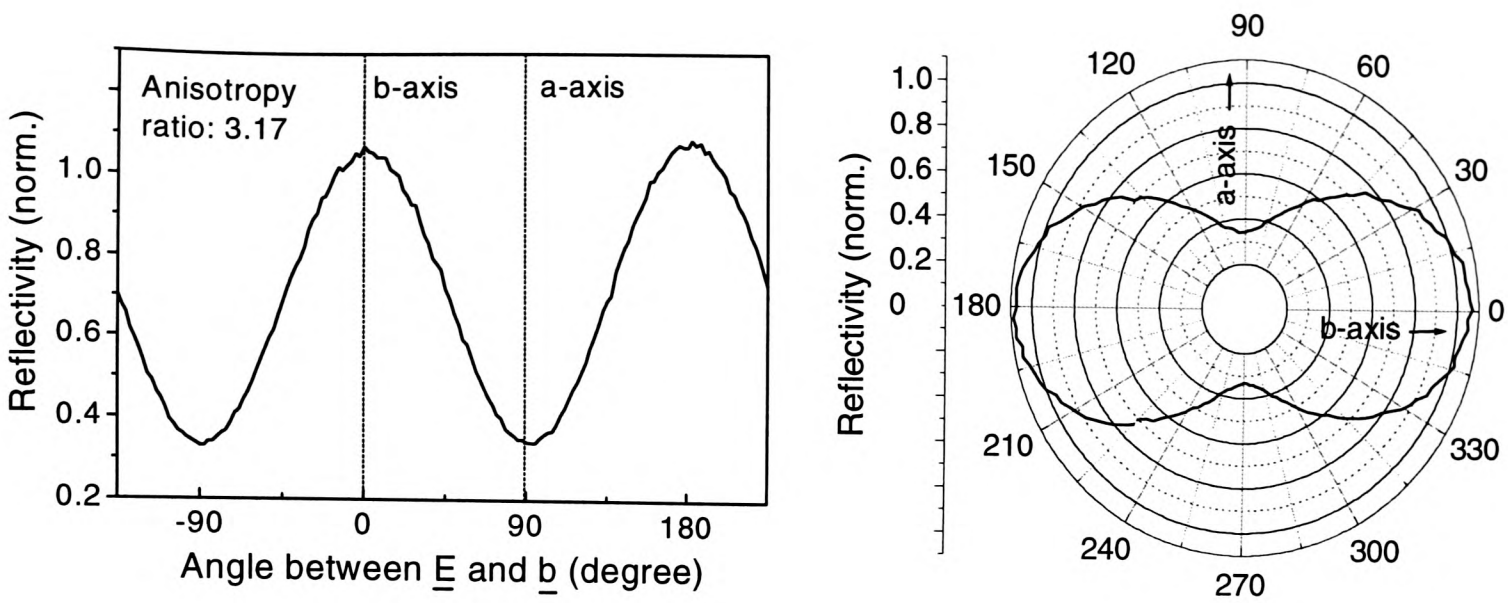

Figure 7.1: Reflectivity of detwinned YBCO-123 single crystal as a function of the probe beam electric field polarization, represented on both a linear and a polar plot.

The angular dependence of R can be fitted very well by the function:

$$R = \alpha \cdot sin^2(\theta) + \beta \cdot cos^2(\theta)$$

where θ is the angle between $\underline{b}$ and the electric field vector $\underline{E}$ (the fit gives $\alpha = 0.34$ and $\beta = 1.1$). The reflection can be therefore separated into two orthogonal components with $\underline{E} \perp \underline{b}$ and $\underline{E} \parallel \underline{b}$, the latter being the chain contribution. As the plane contribution is thought to be isotropic, $R_{\underline{E}\parallel\underline{b}}$ has actually a plane contribution as well.

The maximum anisotropy ratio we measured was 9:1, several crystals exhibited ratios of ~7:1, but most of the crystals had ratios around 3:1. We observed that the anisotropy ratio of samples was high immediately just after detwinning, but it decreased to about 3:1 in one to two days time. Moreover, high anisotropy ratios were difficult to obtain. The reason for this difficulty and for the decrease of the ratio could be due to non-optimal doping (meaning less oxygen in the chain structures), surface contamination or re-twinning after natural or laser-heating-induced relaxation. The only published work on the anisotropy of the reflectivity is from Zibold et al. [76] who reported an anisotropy

ratio of 2.75:1, which is in agreement with most of our samples.

The thin film samples we observed do not exhibit any reflectivity anisotropy within experimental error. This observation could indicate that the $\underline{a}$ and $\underline{b}$ domains are randomly oriented. However, as the film is grown epitaxially on strontium titanate, we expect the film microstructure to consist of a mosaic of $\underline{a}$ and $\underline{b}$-oriented crystallites due to strain relaxation. In order to obtain an isotropic reflectivity in the thin films, the size of the domains has to be much smaller than 50μm, the laser spot diameter.

7.2 Anisotropy of the photo-induced Reflectivity in the a-b Plane

Fig 7.2 shows the photo-induced reflectivity recorded at a temperature of 4K for the two orientations: $\mathcal{R}_a = (\Delta R/R)_{\underline{E}\|\underline{a}}$ with the electric field of the probe beam parallel to the a-axis and $\mathcal{R}_b = (\Delta R/R)_{\underline{E}\|\underline{b}}$ with the electric field $\underline{E}$ parallel to the b-axis. Different results are obtained depending on the sample quality i.e. on the surface contamination or the doping level, and we present here the most reproducible measurements. These two geometries give quite different behaviour. $\mathcal{R}_a$ has a resolution-limited rise time of about 150fs. Its decay is bi-exponential with a very fast decay τ_{a_1} of 200fs and a longer decay τ_{a_2} of 5ps, followed by a long-lived ($>$ 12ns) component which is similar to that previously reported [117]. $\mathcal{R}_b$ has the same resolution-limited rise time, a bi-exponential decay with time constants of $\tau_{b_1} = 700$fs and $\tau_{b_2} = 2.5$ps, and again a long-lived component. The sign of the long-lived component is positive for $\mathcal{R}_a$ but negative for $\mathcal{R}_b$.

Fig 7.2 also shows for comparison a typical thin film response, $\mathcal{R}_{film}$ [116], which shows a resolution-limited rise time with a mono-exponential decay time $\tau_{film} = 2.3$ps; the long-lived component is negative and very small. $\mathcal{R}_{film}$ is therefore more closely similar to $\mathcal{R}_b$ than $\mathcal{R}_a$, which is explained by the rather large reflectance anisotropy

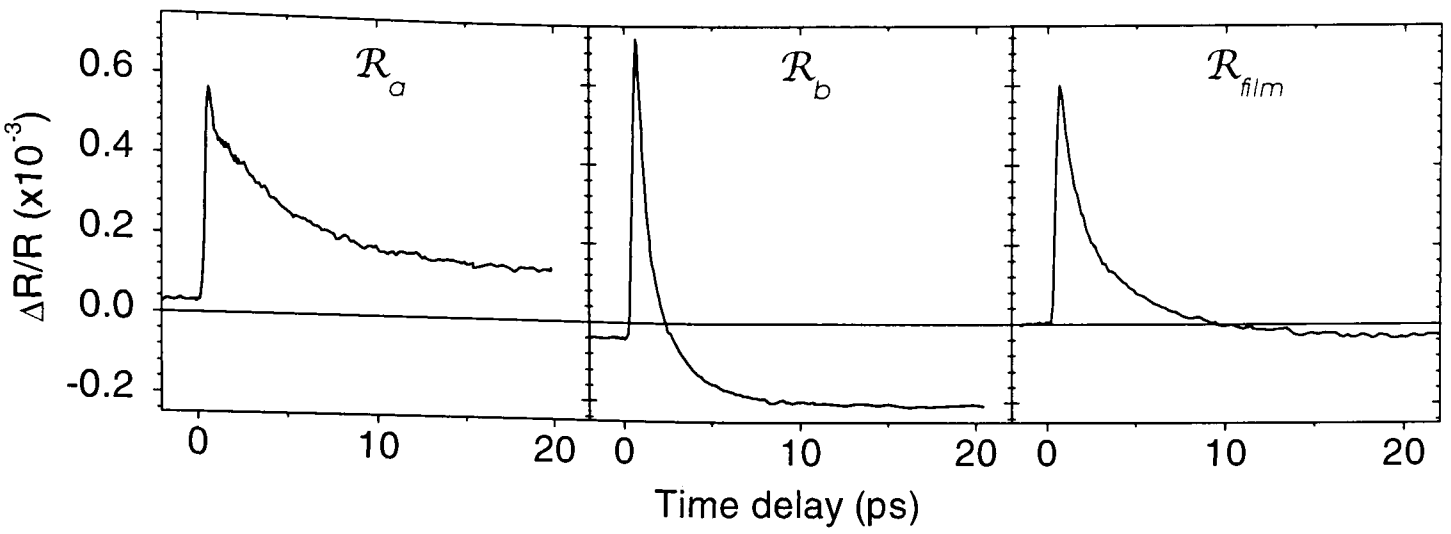

Figure 7.2: Photo-induced reflectivity $\mathcal{R}_a = (\Delta R/R)_{\underline{\mathrm{E}\|\mathrm{a}}}$ and $\mathcal{R}_b = (\Delta R/R)_{\underline{\mathrm{E}\|\mathrm{b}}}$ of detwinned YBCO-123 single crystal at 4K. A thin film response $\mathcal{R}_{film}$ is also presented for comparison.

ratio ($R_{\underline{\mathrm{E}\|\mathrm{b}}}/R_{\underline{\mathrm{E}\|\mathrm{a}}} = 3$).

Fig 7.3 shows the temperature evolution of the two signals. $\mathcal{R}_b$ has a similar form at all temperatures with changes only in the overall magnitude of the signal. $\mathcal{R}_a$ shows a much richer behaviour, which has not been previously reported in any thin film measurements. Below 80K, the signal has a relatively slow relaxation time $\tau_{a_2} \simeq 3$ps. At 80K there is a sudden change in the dynamics, as a dip in the signal is observed just after the initial peak. This negative peak, superimposed to the positive signal, has a resolution-limited decrease and its decay time is smaller than 1ps. At the highest temperatures, above 225K, the observed dynamics is very similar to the response of a wide range of metals [89].

Fig 7.4 shows the temperature dependence of the peak value of $\mathcal{R}_a$, $\mathcal{R}_b$ and $\mathcal{R}_{film}$. The magnitudes are defined here as the peak heights with respect to the -3ps signal i.e. without taking into account the long-lived component. Both $\mathcal{R}_a$ and $\mathcal{R}_b$ have a near temperature independent magnitude below $\mathrm{T}_c = 80$K, after which $\mathcal{R}_a$ drops by a factor of 2, while $\mathcal{R}_b$ drops to zero between 150 and 225K. The gradual change in magnitude of $\mathcal{R}_b$ is mirrored by $\mathcal{R}_{film}$.

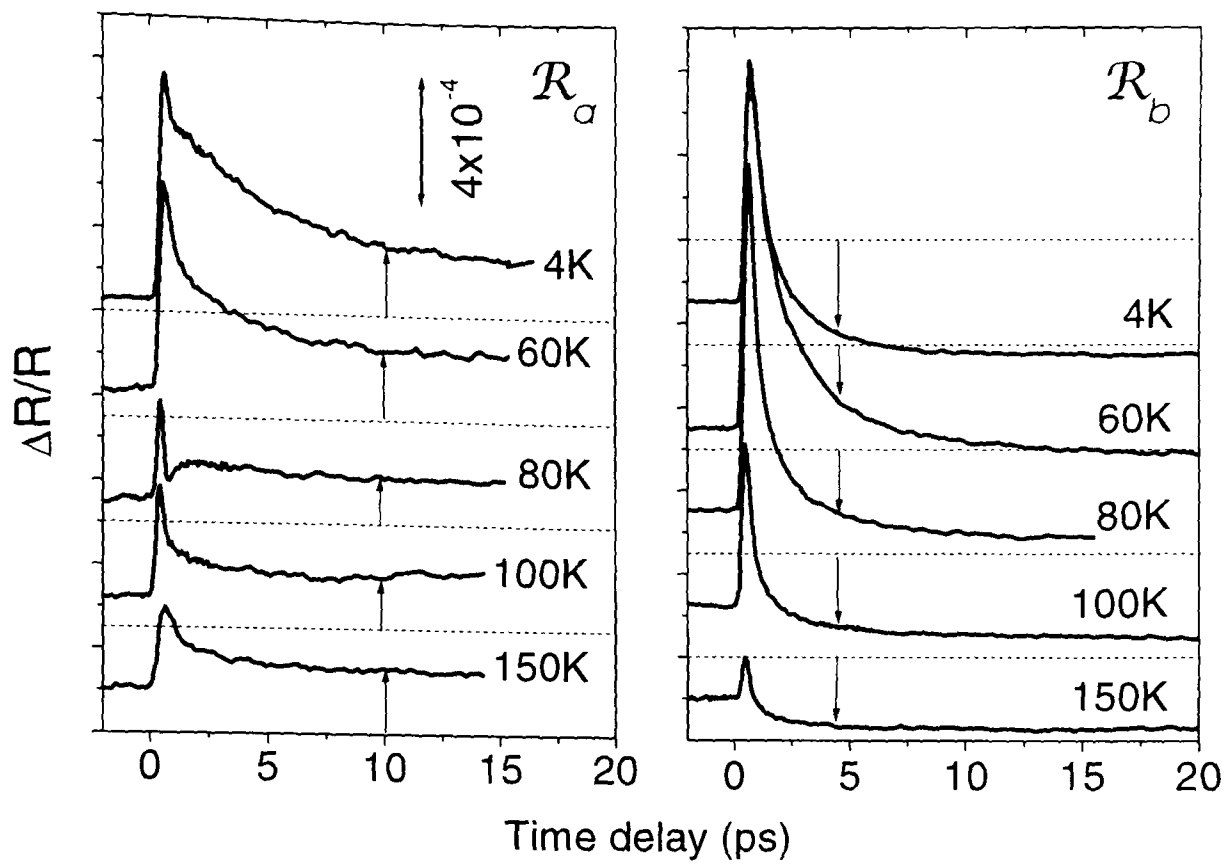

Figure 7.3: Temperature dependence of the YBCO-123 photo-induced dynamics probed with $\underline{\mathrm{E}} \parallel \underline{\mathrm{a}}$ ($\mathcal{R}_a$) and the $\underline{\mathrm{E}} \parallel \underline{\mathrm{b}}$ ($\mathcal{R}_b$).

The apparent T_c inferred from $\mathcal{R}_a$ at $T_c = 80$K is lower than the critical temperature obtained before detwinning, the ac susceptibility measurement giving $T_c = 92.5$K. The difference may be due to heating by the pump laser beam. Another possibility is that the oxygen concentration dropped during the detwinning process, resulting in a slightly underdoped surface, and our experiment probes only the top 1000Å of the crystal corresponding to the penetration depth of the probe light. This assumption is supported by the reflectivity anisotropy ratio of our sample being lower than the maximum value (7:1), however we cannot measure T_c after detwinning using ac susceptibility which probes the bulk critical temperature. We could possibly use a muon spin rotation experiment, which probes the surface of the sample.

As we saw at 4K, the relaxation of $\mathcal{R}_a$ is best modelled with a two-component exponential decay. We observed a fast, temperature independent decay τ_{a_1} and a slower, temperature dependent decay τ_{a_2} going from 4.8ps at 4K to 2.5ps at 90K, as shown in

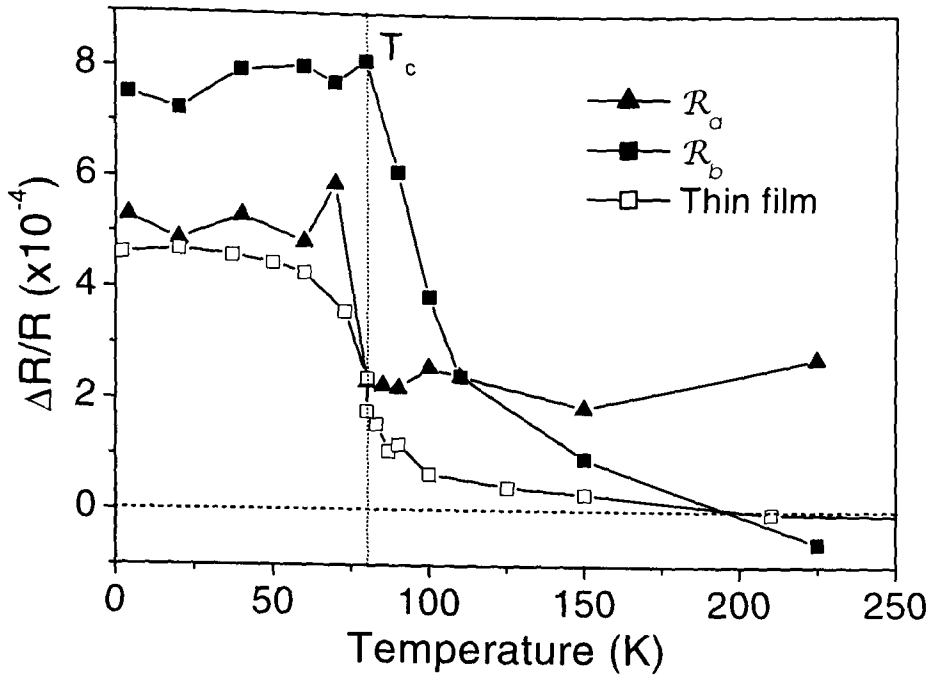

Figure 7.4: Temperature dependence of the inital transient magnitude of YBCO-123 thin film (open squares) and YBCO-123 detwinned single crystal for E || a (solid triangles) and for E || b (solid squares).

Fig 7.5a. Between 90 and 110K the complex dynamics with the negative dip cannot be fitted. At 110K, τ_{a_2} starts increasing until about 150K, probably due to the underlying negative peak, and finally τ_{a_2} decreases again. Within the experimental error, the same fitting procedure for $\mathcal{R}_b$ gives a relatively temperature independent decay with τ_{b_1} between 0.3 and 0.8ps and τ_{b_2} between 2.5 and 3ps.

A T_c of 80K, measured from $\mathcal{R}_a$, corresponds to a doping level of $\delta = 0.15$ giving a pseudogap temperature T^* of $\sim$190K [53], which is close to the extrapolated zero crossing point of $\mathcal{R}_b$ in Fig 7.4.

Our recent measurements on BSCCO-2212 and TBCO-2201 thin films and single crystals presented in chapter 5 show responses with remarkable similarities to $\mathcal{R}_a$. First, the magnitude of $\mathcal{R}_a$ decreases to a constant value at T_c in a similar way as for BSCCO and TBCO i.e. it drops at T_c instead of slowly decreasing to zero at T^*. Second, the negative peak near T_c (clearly observed at 80K in Fig 7.3) and its subsequent continuing evolution up to a higher transition temperature is extensively observed in BSCCO and

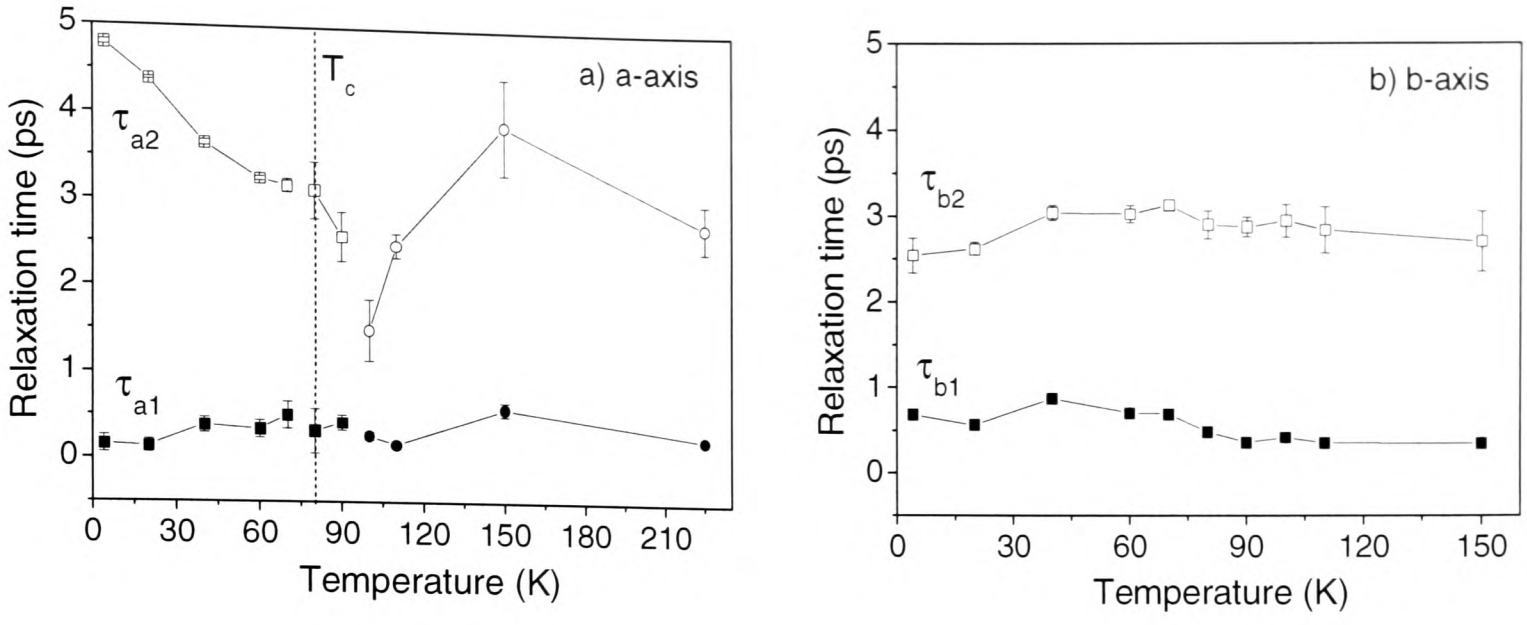

Figure 7.5: Temperature dependence of the relaxation time of YBCO-123 single crystal from a bi-exponential fit for (a) $\underline{E} \parallel \underline{a}$ and (b) $\underline{E} \parallel \underline{b}$. The open symbols are from the longer component and the solid ones from the shorter component.

TBCO. The onset of the negative component at T_c, its disappearance at a temperature close to T* and its decay time are comparable to the negative component attributed to the pseudogap phase in BSCCO and TBCO in section 5.3. Consequently, the behaviour of the new dynamics $\mathcal{R}_a$ above T_c shows that an intermediate regime exists between the low-temperature superconducting phase and the high-temperature metallic response.

Finally, the decay rate $\tau_{a_2}^{-1}$ has a linear temperature dependence below T_c. In Fig 7.6 is shown the relaxation rate of BSCCO-2212, YBCO-123 thin film (τ_{film}^{-1}) and $\mathcal{R}_a$ ($\tau_{a_2}^{-1}$) at the same excitation density. Whilst for YBCO-123 thin films, τ_{film}^{-1} is temperature independent below 60K, the temperature dependence of $\tau_{a_2}^{-1}$ is linear in a similar way as for BSCCO-2212. The dependence is less marked in the $\tau_{a_2}^{-1}$ case, although this could be explained as being due to the incomplete detwinning of the crystal.

Up to date, YBCO-123 measurements on thin films and twinned single crystals exhibited a temperature independent decay time τ_{film} below T_c - 20K [98, 53]. The temperature independence of τ_{b_2} that we observed would explain the previous measurements, as

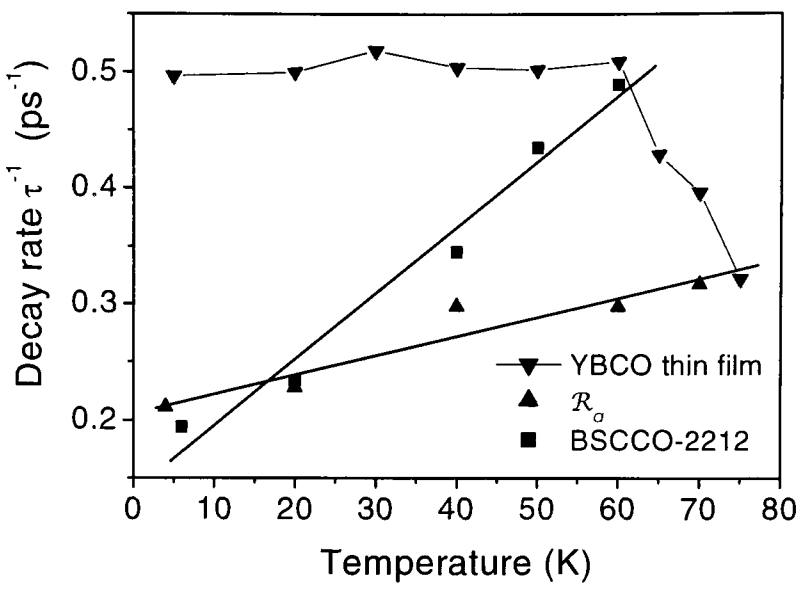

Figure 7.6: Temperature dependence of the decay rate of $\mathcal{R}_a$ (τ_{a2}), YBCO-123 thin film and BSCCO-2212 thin film for comparison.

the contribution of the film response is mainly $\mathcal{R}_b$.

We saw in section 5.3 that in BSCCO-2212 and TBCO-2201, the onset of the negative signal related to the pseudogap state is at T_c, its maximum is ~110K and it vanishes at T*. By analogy, we could argue that the relaxation time τ_{a_2} of the $\mathcal{R}_a$ (in Fig 7.5a) is decreasing from T_c to a minimum at ~105K due to the remaining of the negative peak clearly observed at 80K. Above ~105K, τ_{a_2} is increasing, but because of the lack of data points, we can only affirm that its maximum is between 150 and 210K, which is consistent with $T^* \cong 190K$.

The dynamics of $\mathcal{R}_a$ is comparable to the BSCCO and TBCO dynamics in terms of the signal magnitude, the presence of the negative peak in the pseudogap phase and the linear temperature dependence of the decay rate. On the other hand, $\mathcal{R}_b$ is similar to the YBCO thin film dynamics in terms of the signal magnitude and the relaxation time.

The two curves fitting the temperature dependence of the signal magnitudes in Fig 7.7 correspond to the quasiparticle cooling model by Kabanov et al. [53]. As described in detail in section 4.5, this model assumes that the signal is proportional to the excess number of quasiparticles i.e. to the population out of thermal equilibrium with the low-

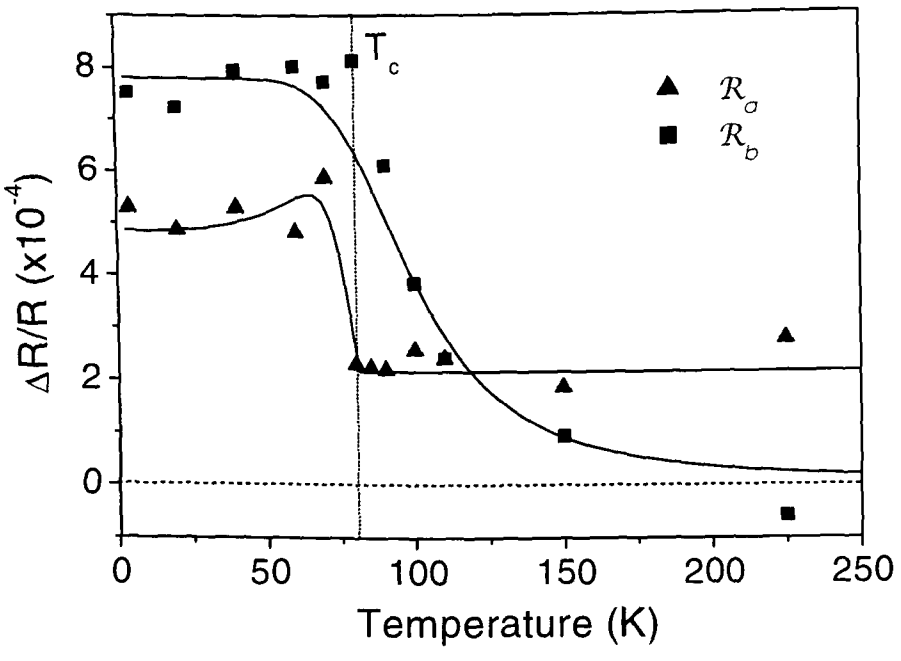

Figure 7.7: Temperature dependence of the inital transient magnitude of $\mathcal{R}_a$ and $\mathcal{R}_b$ of a detwinned single crystal. The fits are from Kabanov et al. [53] with a temperature dependent gap for the a-axis and a temperature independent gap for the b-axis.

energy phonons. The curve fitting for $\mathcal{R}_a$ assumes that the quasiparticles are excited across a standard temperature dependent BCS gap. Although the data are rather scattered, the model does fit the rapid drop in signal at T_c. The curve fitting for $\mathcal{R}_b$ assumes that the quasiparticles are excited across a temperature independent pseudogap with a magnitude of 52meV, which is in good agreement with the gap energy expected for a doping level of $\delta = 0.15$ [53]. It fits well the rather slower temperature dependence of the signal above T_c and its eventual disappearance at T^*.

In summary, with $\underline{E} \parallel \underline{b}$, we access a different optical transition from that providing the CuO_2 plane response, present in BSCCO-2212, TBCO-2201 and in $\mathcal{R}_a$. Moreover, as $|\mathcal{R}_b|_{max}$ can be fitted by the temperature independent component present in the model of Kabanov et al., we deduce that $\mathcal{R}_b$ (being the main component of $\mathcal{R}_{film}$) is sensitive to the pseudogap.

A possible origin of $\mathcal{R}_b$ can be hypothesized as follows: two different plasma frequen-

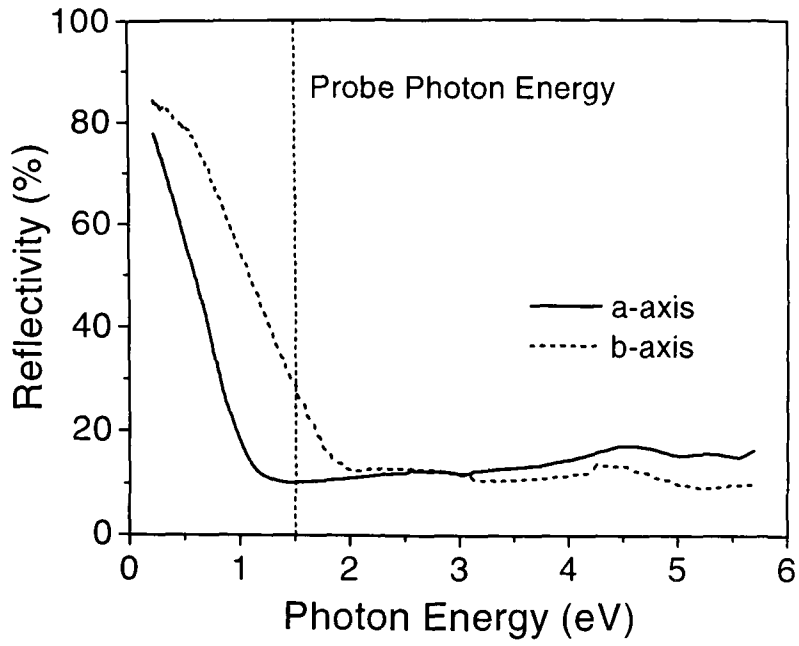

Figure 7.8: Polarized reflectance spectra from detwinned optimally-doped YBCO-123 single crystal at room temperature measured by Zibold et al. [76].

cies are observed in the reflectivity spectrum of detwinned YBCO-123 crystals. Polarized reflectivity measurements have identified these two plasma frequencies as corresponding to $\underline{E} \parallel \underline{a}$ giving $\omega_{pa} = 1.03$eV and $\underline{E} \parallel \underline{b}$ giving $\omega_{pb} = 1.48$eV [76], the difference arising from the extra holes in the CuO chains which contribute an additional component to the intraband response. The reflectivity spectra for $\underline{E}$ along the a- and b-axes are shown in Fig 7.8. The probe energy in our experiments is 1.5eV, very close to ω_{pb} but far above ω_{pa}. The proximity of the probe energy to ω_{pb} suggests that $\mathcal{R}_b$ is an intraband response i.e. from the Drude part of the reflectivity. The scattering rate of a pre-formed pair [42] in the pseudogap state [4] is likely to be different from the scattering rate of a single electron in the normal state, which would explain why the Drude reflectivity and hence $\mathcal{R}_b$ are sensitive to the pseudogap state. On the other hand, the difference between the probe photon energy and ω_{pa} implies that $\mathcal{R}_a$ likely probes an interband transitions.

A simpler possibility for the origin of $\mathcal{R}_b$ could be the existence of an extra interband transition due to the presence of the chains and sensitive to the pseudogap. In this case,

the question of how the pseudogap can influence this transition, whilst the superconducting gap cannot, must be addressed. This hypothesis would require further investigations concerning the microscopic mechanisms of the probe interaction to be evaluated.

One more alternative to explain the connection between $\mathcal{R}_b$ and the pseudogap would be that the pseudogap itself is actually located in the chains and thus that the chain quasiparticles would have a gap-like excitation at all temperatures, with thermal excitations across the gap reducing the signal as the temperature increases. However, this hypothesis has to be refuted as the pseudogap is observed in various chainless HTSC materials and as ARPES data on the pseudogap exhibit a 2D structure [38, 39].

In the Kabanov model, the quasiparticle cooling is controlled by the decay rate of phonons with energy larger than 2Δ. As there are two relaxation rates (for $\mathcal{R}_a$ and for $\mathcal{R}_b$), the model implies two distinct cooling rates. Consequently, the high-energy phonons related to $\mathcal{R}_a$ have to be uncoupled from the high-energy phonons related to $\mathcal{R}_b$. Coupled to the same set of phonon, the two dynamics would be limited by the same bottlenecked phonon relaxation and hence could not be different. In other words, one problem with the Kabanov model is that the superconducting gap and the pseudogap have to be spatially separated in order to give rise to two relaxation times, one related to the superconducting gap and one related to the pseudogap. This is only possible if the size of the domains is large enough to ensure negligible exchange of phonons between them. Stripes for instance would not be a possibility for one of the domains because of the phonon exchange between the stripes and the rest of the lattice. The hypothetical presence of the pseudogap in the chains could be a solution to this issue. In this case, the chains and the planes would constitute the two separate domains. However, this supposition requires a theoretical investigation to consider the possibility that the phonon modes in the chains and the planes are not in equilibrium.

It has been suggested by Kabanov et al. [53] from an analysis of the ultrafast results

of thin film measurements that superconductivity in YBCO-123 is s-wave in nature: this arises from the temperature independence of the decay rate τ_{film}^{-1}. In our measurements, the linear temperature dependence of $\tau_{a_2}^{-1}$ below T_c cannot be explained with an s-wave model. On the contrary, a predominantly d-wave gap has been proposed as an explanation for the linear temperature dependence of the decay rate for BSCCO-2212 and TBCO-2201 in section 5.2.

We observed that $\mathcal{R}_b$ is sensitive to the pseudogap, but also that $\mathcal{R}_a$ is sensitive to the pseudogap in the form of the negative peak observed clearly at 80K in Fig 7.3. The relaxation time of the negative peak at 80K is smaller than 1ps and hence is close to that of the negative component observed in BSCCO and TBCO, which displays decay times of ~500fs. This time is much smaller than the relaxation time τ_{b_2} of 3ps measured in $\mathcal{R}_b$. It is not possible to explain two different relaxation dynamics associated with the pseudogap in terms of the quasiparticle cooling model, where the relaxation rate is controlled by the lifetime of high-energy phonons. This observation is another indication that for the negative peak associated with the pseudogap (in Fig 5.12 and in Fig 7.3 at 80K), we may observe excitations of the pseudogap correlations as suggested in section 5.6, instead of quasiparticle dynamics. Indeed, it is the only way to explain the observation of two distinct dynamics related to the pseudogap.

In summary, $\underline{E} \parallel \underline{b}$ allows a different probe mechanism providing a new response due to the pseudogap in detwinned YBCO-123 single crystals. The present work shows the possibility of removing the component analyzed by Kabanov et al. to find the underlying response by probing only $\mathcal{R}_a$. The new response we observed is not simply related to T_c, but it is a complex response similar to what we observed for the BSCCO-2212 and TBCO-2201 materials. From this observation, we suggest that this latter response might be universal to the HTSC compounds.

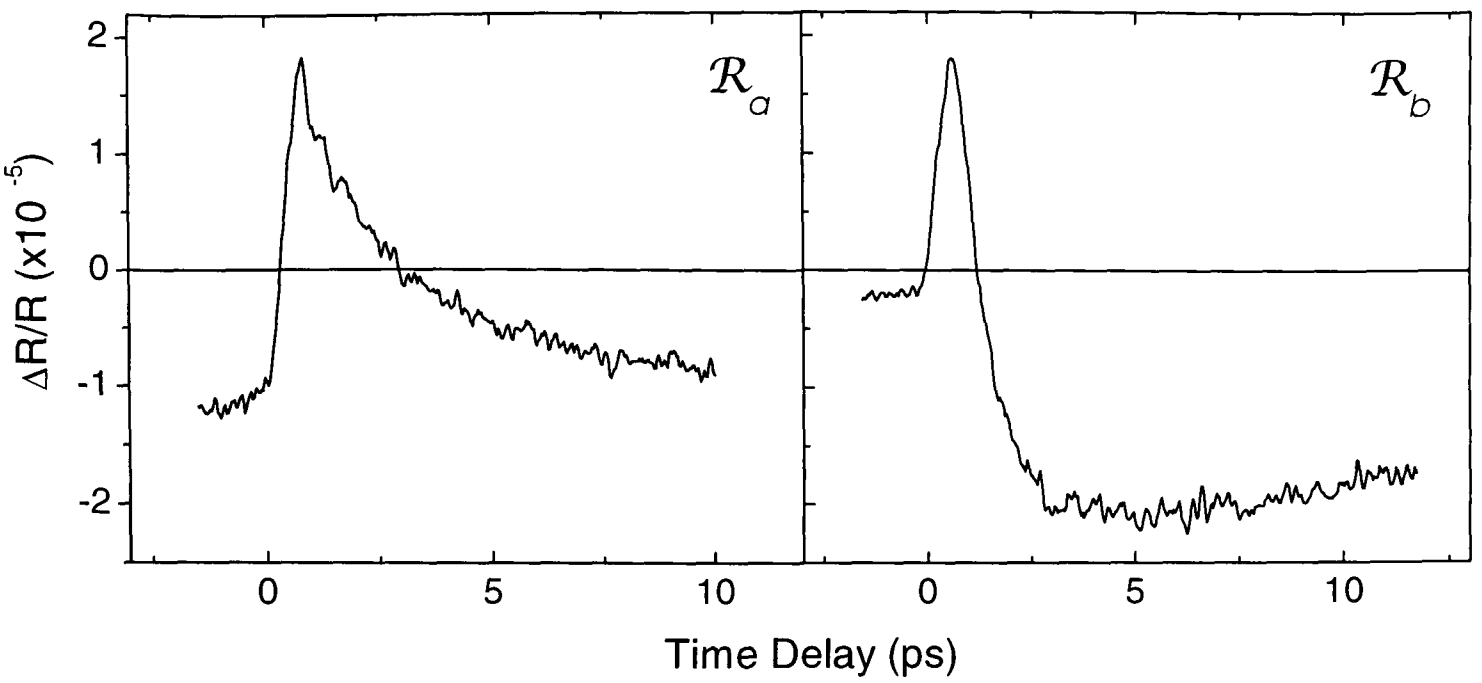

Figure 7.9: Photo-induced reflectivity $\mathcal{R}_a$ and $\mathcal{R}_b$ of detwinned YBCO-123 single crystal with an anisotropy ratio of 7.2:1 at 4K.

7.3 Superconducting State Symmetry in the Long-lived Component

The temperature dependence of the amplitude of the long-lived component is well-fitted by thermally-activated behaviour (cf. section 4.6):

$$\Delta R/R \; \alpha \; e^{-2\Delta/k_B T} \tag{7.1}$$

Therefore, the amplitude of the superconducting gap 2Δ can be determined from the magnitude of the long-lived component. Consequently, it is possible to probe the superconducting symmetry by measuring the angular dependence of the long-lived component.

The sample we used for these measurements presented a larger anisotropy ratio of 7.2:1, instead of 3:1 for the samples measured in the previous section. The photo-induced dynamics $\mathcal{R}_a$ and $\mathcal{R}_b$ at 4K of this sample are shown for comparison in Fig 7.9.

The dynamics are qualitatively the same as that described in the previous section. The magnitudes are about 20 times smaller in this section due to poorer experimental

conditions. The difference from the previous sets of data is that the long-lived signal is negative for both $\mathcal{R}_a$ and $\mathcal{R}_b$ in Fig 7.9, in contradiction with Fig 7.3 presenting for all temperatures, a positive long-lived component for $\mathcal{R}_a$ and a negative one for $\mathcal{R}_b$. The long-lived component has been found to be very dependent on the anisotropy ratio, however further experiments are needed to give a clear conclusion on this point. Nevertheless, the origin of this discrepancy is probably the oxygen concentration in the chains i.e. the doping level, being modified by the detwinning process.

Angular dependences of the photo-induced reflectivity have been made on detwinned single crystals from 4 to 60K. The results obtained at 60K and at a time delay of +10ps are shown in Fig 7.10 in the form of linear and polar plots. At 60K the long-lived signal is composed of four equal amplitude negative peaks at 45°, 135°, 225°and 315°.

Unfortunately, this set of measurements has been made only until a time difference of 10ps, where the presence of the initial transient has still a significant contribution. Consequently, the polarization dependence can be observed only from 60K, where the initial transient has a small magnitude.

The anisotropy of the equilibrium reflectivity, of the photo-induced reflectivity at zero delay and of the long-lived component at 4K can be expressed in terms of the sum of two orthogonal components, for $\underline{E} \parallel \underline{b}$ and $\underline{E} \perp \underline{b}$, i.e. in the form of

$$\alpha \cdot sin^2(\theta) + \beta \cdot cos^2(\theta)$$

θ being the angle between the $\underline{b}$ and $\underline{E}$, as illustrated in Fig 7.1. However, the position of the four peaks in the a-b plane for the long-lived component at 60K cannot be fitted by two independent components. Consequently, in this particular case, the probe mechanism has to be the same for both the a and b-axis i.e. it has to be related to the planes and not to the chains. Moreover, optical effects like birefringence for instance cannot provide a polarization dependence as that observed in Fig 7.10.

In the previous section, we assumed that the photo-induced signal $\mathcal{R}_a$ is due to

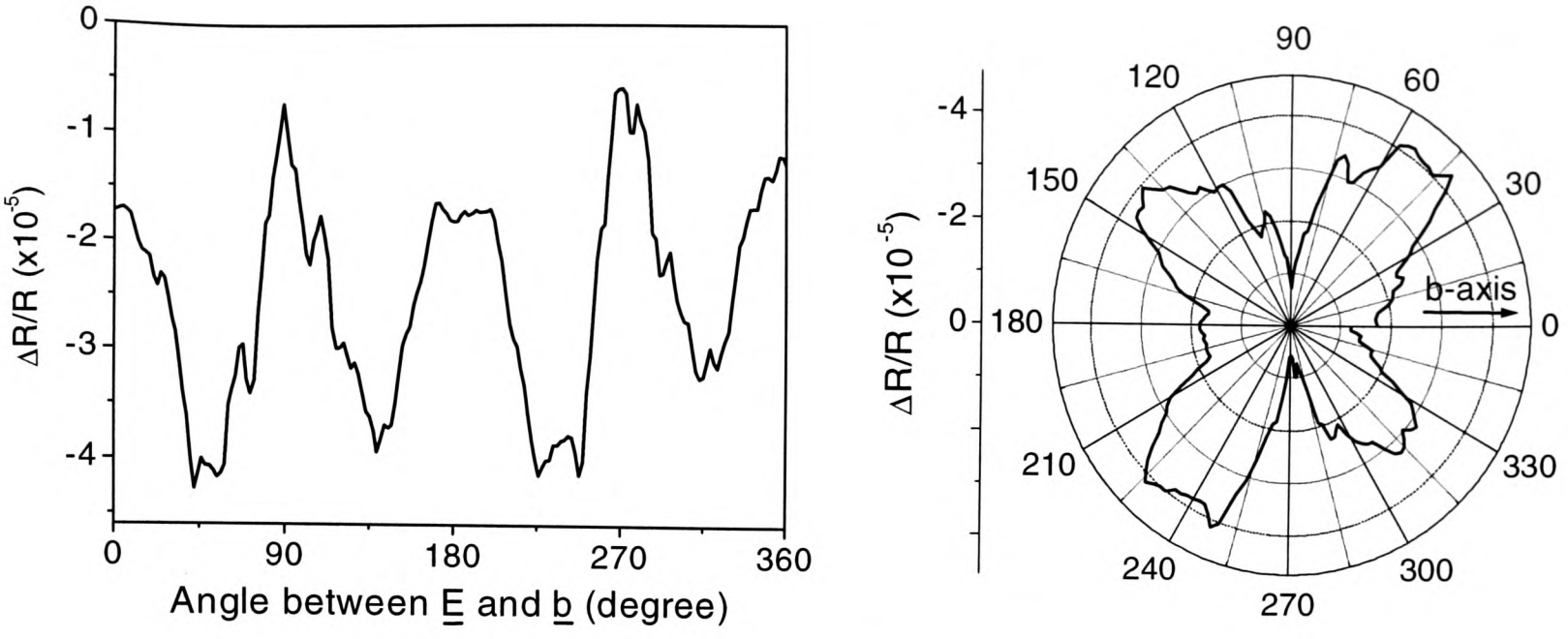

Figure 7.10: Angular dependence (on linear and polar plots) of the anisotropy of the long-lived component (10ps) of the photo-induced reflectivity for a detwinned YBCO-123 single crystal in the superconducting state at 60K.

interband transitions, as the plasma frequency ω_{pa} (for $\underline{\mathrm{E}} \parallel \underline{\mathrm{a}}$) is well below the probe photon energy. In this case, the interband transition probability for the probe light is given by the Fermi golden rule $\Delta R/R \; \alpha \; n_{qp}\rho_f \, |M_{ij}|^2$, where n_{qp} is the photo-excited carrier density, ρ_f is the final density of unoccupied states and M_{ij} is the dipole matrix element [53]. Consequently, we may observe here partly or completely the polarization dependence of ρ_f or M_{ij}.

As seen in detail in section 4.6, the temperature dependence of the long-lived component below T_c is well fitted with a thermally-activated behaviour (equation 7.1). In order to interpret the polarization dependence, we can use the same model, i.e. the symmetry of $\Delta R/R$ is associated with the symmetry of the energy gap. The superconducting energy gap Δ, extracted from the latter expression, is represented in Fig 7.11, together with the d-wave function $\Delta = \Delta_0 |cos(\theta^2) - sin(\theta^2)|$, superimposed for comparison. The d-wave shape fits well the data in the chain direction ($\theta = 0°$), whilst the agreement along the

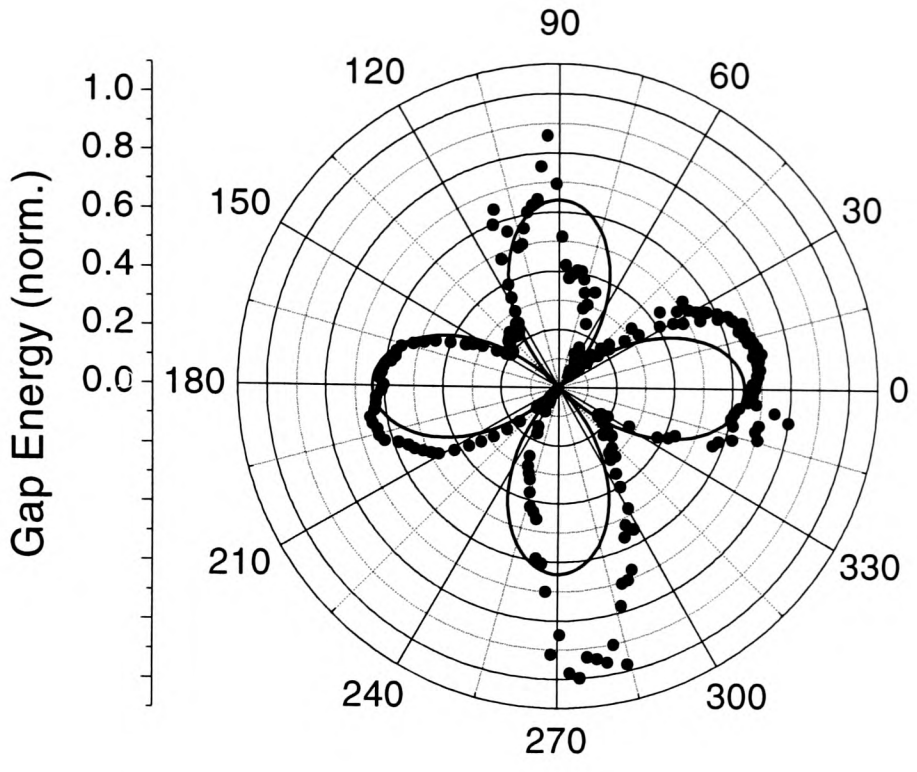

Figure 7.11: Energy gap of detwinned YBCO-123 single crystal at 60K, from the thermally-activated model developed for the long-lived component.

a-axis direction is poorer. However, this discrepancy is due to a stronger contamination at 10ps from the initial transient for $\underline{E} \parallel \underline{a}$.

It is now widely accepted that YBCO-123 has a predominantly d-wave superconducting state symmetry, which is reflected in the energy gap symmetry and hence in the distribution of thermally-excited quasiparticles. With the lack of knowledge about the YBCO band structure, we cannot infer to have another evidence for a d-wave symmetry of the superconducting state. However, it is unlikely that either the final density of unoccupied states ρ_f or the dipole matrix element M_{ij} have a symmetry given by Fig 7.10 i.e. that their symmetry is not the sum of two orthogonal components along the chains and perpendicular to the chains.

7.4 Conclusion

We separately identified for the first time two different dynamical processes in the YBCO-123 single crystal response: $\mathcal{R}_a$ with the probe electric field $\underline{E}$ parallel to the chains and $\mathcal{R}_b$ with $\underline{E}$ perpendicular to the chains. The thin film response is similar to $\mathcal{R}_b$, which means that the previous measurements on YBCO are masked by the dynamics associated with the chains. Therefore, measurements of detwinned samples with $\underline{E} \parallel \underline{a}$ have the advantage of avoiding the component with $\underline{E} \parallel \underline{b}$ and of observing the underlying $\mathcal{R}_a$ response associated with the CuO_2 planes.

We observed that $\mathcal{R}_b$ is related to the pseudogap and that $\mathcal{R}_a$ has several similarities with the BSCCO-2212 and TBCO-2201 response presented in chapter 5. In particular, the negative peak superimposed to the positive signal and related to the pseudogap seems to be also present from T_c to T^*; the relaxation rate is linear in temperature in the superconducting state and the temperature dependence of the signal magnitude is similar to that of BSCCO and TBCO. Consequently, it appears that $\mathcal{R}_a$ is a response due to the superconducting planes and is common to the other HTSC compound measurements presented in this thesis.

The pseudogap response obtained from the Kabanov model fits $\mathcal{R}_b$, whilst the condensate response fits $\mathcal{R}_a$. Our results indicates therefore that the two components of the Kabanov model are due to a probe mechanism related to the chains for the temperature independent gap and to the planes for the BCS-like temperature dependent gap.

As the plasma frequency ω_{pb} associated with the chains is very close to the probe photon energy, we argue that the probe mechanism of $\mathcal{R}_b$ is composed of intraband transitions. In other words, for $\underline{E} \parallel \underline{b}$, it would be the Drude reflectivity which is sensitive to the number of the pre-formed pairs in the pseudogap state. On the other hand, the difference between the plasma frequency ω_{pa} associated with the CuO_2 planes and the probe photon energy favors interband transitions as the probe mechanism.

The pseudogap component observed along the b-axis ($\mathcal{R}_b$) has a different relaxation time from the negative component between T_c and T^* in $\mathcal{R}_a$ and in the BSCCO-2212 and TBCO-2201 response. This observation is another indication that we are probing excitations of the pseudogap correlations, as assumed in section 5.6, instead of quasiparticle dynamics.

In the long-lived component at 60K, the a-b plane polarization anisotropy exhibits a dependence which is not possible to fit with two orthogonal components along the chains and perpendicular to the chains. Using the thermally-activated behaviour, which explains the temperature dependence of the long-lived component below T_c, we can interpret the anisotropy as being due to a predominantly d-wave superconducting gap. Unfortunately, because the anisotropy of the final density of states and of the dipole matrix are unknown, we cannot be certain to probe the superconducting state symmetry.

Chapter 8

Conclusion

Using time-resolved photo-induced reflectivity we measured the dynamics of low-energy electronic excitations in $YBa_2Cu_3O_{7-\delta}$ (YBCO-123), $Bi_2Sr_2CaCu_2O_{8+\delta}$ (BSCCO-2212) and $Tl_2Ba_2CuO_{6+\delta}$ (TBCO-2201). For the first time we reported a systematic work on the ultrafast response of BSCCO-2212 and TBCO-2201, measurements of detwinned YBCO-123 single crystal with $\underline{E}$ parallel to the a- and b-axis and high-resolution measurements of the rising edge dynamics of YBCO-123 thin films. We proved that the excitation pulse is only weakly perturbing the superconducting ground state and therefore that we are in a near-equilibrium state. We obtained very reproducible data for both BSCCO-2212 and TBCO-2201 with a high signal-to-noise ratio. The YBCO-123 single crystal data were more difficult to obtain as the detwinned areas are not stable.

We identified similar photo-induced responses for both BSCCO-2212 and TBCO-2201. Moreover, the YBCO-123 response for $\underline{E} \parallel \underline{a}$ exhibits common features with the BSCCO-2212 and TBCO-2201 responses, which indicates that we observed a universal response in HTSC coming from the CuO_2 planes. This latter response is composed of three different parts corresponding to the superconducting, pseudogap and normal ground states. We argued that the probe mechanism is composed of interband transitions in the

superconducting state and that the signal is proportional to the number of broken pairs. A bimolecular model has been proposed to explain the linear temperature dependence of the decay rate. This model implies that the re-formation of the condensate is limited by the rate at which quasiparticles interact at low temperature ($T < 20K$ for BSCCO-2212) and by the high-energy phonon lifetime at higher temperature. Moreover, we observed superconducting fluctuations up to 13K above T_c and a divergence of the long-lived component ($> 12ns$) for $T < 20K$ which can be explained by a cw heating model.

In the pseudogap state we have several indications that the origin of the negative peak observed between T_c and T^* is different from that of the superconducting signal below T_c. We argued that the probe mechanism in the pseudogap state is electronic correlations associated with the pseudogap, i.e. modulations of the number of pre-formed pairs, according to the pre-formed pair scenario. In the normal state we observed a very similar dynamics to that of elementary metals.

A new response has been observed in detwinned YBCO-123 with $\underline{E} \parallel \underline{b}$, which is different from that reported for BSCCO-2212 and TBCO-2201. We argued that this component is solely responsive to the pseudogap and that its origin is intraband transitions, i.e. from the difference in scattering rate between pre-formed pairs and single quasiparticles in the Drude reflectivity.

We found that the responses of YBCO-123 twinned thin films and twinned single crystals measured up to date are similar to that of detwinned single crystals with $\underline{E} \parallel \underline{b}$. Moreover, the two responses $\mathcal{R}_a$ ($\underline{E} \parallel \underline{a}$) and $\mathcal{R}_b$ ($\underline{E} \parallel \underline{b}$) can be well fitted by the two components of the Kabanov model [53] ("collective" component for $\mathcal{R}_a$ and pseudogap component for $\mathcal{R}_b$).

The photo-induced reflectivity exhibits a strong a-b plane anisotropy in the long-lived signal ($> 12ns$), which can be interpreted via the thermally-activated model as coming from a predominantly d-wave symmetry of the superconducting state.

The rising edge dynamics of YBCO-123 has been resolved in time for the first time. The model developed to interpret the results implies that the relaxation time of the high-energy photo-excited quasiparticles down to the Fermi energy is ~55fs. This time is also an upper limit for the time constant of the pair breaking by ultrafast pulses. With the knowledge of the rise time in the initial dynamics, we proved that the Mazin model [13] cannot explain both the oscillatory and the non-oscillatory parts of the dynamics, which are observed with the 35fs resolution experiment.

Although we concluded from our interpretation that the responses of BSCCO-2212, TBCO-2201 and $\mathcal{R}_a$ are due to interband transition, a more systematic wavelength dependence of the probe beam would be helpful to provide clear information about the nature of probe mechanism and hence to interpret the time-resolved data. Moreover, measurements of thin films with variable thicknesses and with a variable pulse repetition rate would definitively elucidate the origin of the dynamics on a nanosecond timescale.

The next experiment planed in our laboratory is time-resolved measurements of the mid-infrared reflectivity of HTSC. Excitations at 1.5eV will be probed by mid-infrared, 150fs pulses tunable from 60 to 180meV. At these energies well below the plasma frequency, the electronic response is determined by intraband processes. The work of Carbotte et al. [140] strongly suggests that the 41meV antiferromagnetic spin fluctuation dominates the response and preliminary time-resolved measurements support this scenario. This experiment will probe the excitations at energies comparable with the superconducting gap energy.

Another interesting experiment would be the measurements of the frequency-dependent electrical conductivity $\sigma(\omega)$ by terahertz reflectivity. This experiment would measure the phase stiffness and the phase correlation time in order to investigate the role of phase coherence.

Considerable theoretical study still needs to be done on the new data we presented in

this thesis and we strongly believe that ultrafast spectroscopy will give further important insights into the nature of the pseudogap and the superconducting state.

Bibliography

[1] Bednorz J.G. and Muller K.A., *Possible High-T_c Superconductivity in the Ba-La-Cu-O system*, Zeitschrift fur Physik B **64**, p. 189 (1986).

[2] Deutcher G., *Present status of High-T_c Research* in *The Gap Symmetry and Fluctuations in High-T_c Superconductors*, NATO ASI Series B **1371**, Plenum, p. 15, New York (1998).

[3] A., Erb A. and Renner C., *Specific heat of high temperature superconductors in high fields at T_c: from BCS to Bose-Einstein condensation*, Physica C **317**, p. 333 (1999).

[4] Timusk T. and Statt B., *The pseudogap in high-temperature superconductors: an experimental survey*, Rep. Prog. Phys. **62**, p. 61 (1999).

[5] Loram J.W., Mirza K.A., Wade J.M., Cooper J.R. and Liang W.Y., *The Electronic Specific Heat of Cuprate Superconductors*, Physica C **235-240**, p. 134 (1994).

[6] Del Fatti N., Bouffanais R., Vallée F. and Flytzanis C., *Nonequilibrium Electron Interactions in Metal Films*, Phys. Rev. Lett. **81**, p. 922 (1998).

[7] Beaurepaire E., Merle J.C., Daunois A. and Bigot J.Y., *Ultrafast spin dynamics in ferromagnetic nickel*, Phys. Rev. Lett. **76**, p. 4250 (1996).

[8] Thomas T.N., Stevens C.J., Choudray A.J.S., Ryan J.F., Mihailovic D., Mertelj T., Forro L., Wagner G. and Evetts J.E., *Photoexcited carrier relaxation and localization in $Bi_2Sr_2Ca_{1-y}Y_yCu_20_8$ and $YBa_2Cu_3O_{7-\delta}$: A study of femtosecond time-resolved spectroscopy*, Phys. Rev. B **53**, p. 12436-12440 (1996).

[9] Eesley G.L., Heremans J., Meyer M.S., Doll G.L. and Liou S.H., *Relaxation Time of the Order Parameter in a High-Temperature Superconductor*, Phys. Rev. Lett. **65**, p. 3445-3447 (1990).

[10] Gay P., Smith D., Stevens C.J., Chen C., Yang G., Abell S.J., Wang D.Z., Wang J.H., Ren Z.F. and Ryan J.F, *Femtosecond Dynamics of BSCCO-2212*, J. of Low Temp. Phys. **117**, p. 1025 (1999).

[11] Smith D.C., Gay P., Stevens C.J., Wang D.Z., Wang J.H., Ren Z.F. and Ryan J.F., *Ultrafast Optical Response of $Tl_2Ba_2CuO_{6+\delta}$*, J. of Low Temp. Phys. **117**, p. 1059 (1999).

[12] Stevens C.J., Gay P., Smith D.C., Chen C. and Ryan J.F., *Anisotropy of the non-equilibrium quasiparticle dynamics in single crystals of $YBa_2Cu_3O_{7-\delta}$*, J. of Low Temp. Phys. **117**, p. 1031 (1999).

[13] Mazin I.I., Liechtenstein A.I., Jepsen O., Andersen O.K. and Rodriguez C.O., *Displacive excitation of coherent phonons in $YBa_2Cu_3O_7$*, Phys. Rev. B **49**, p. 9210-9213 (1994).

[14] Giaver I. and Mergerle K., *Study of Superconductors by Electron Tunneling*, Phys. Rev. **122**, p. 1101 (1961).

[15] Tinkham M., *Introduction to Superconductivity*, McGraw-Hill, New York (1975).

[16] Eliashberg G.M., Sov. Phys. JETP **11**, p. 696 (1960).

[17] Plakida N., *High-Temperature Superconductivity: Experiment and Theory*, Springer (1995).

[18] Ren Z.F., Wang J.H. and Miller D.J., *Continuous control of the superconducting transition temperature from overdoped to underdoped regimes in tetragonal $Tl_2Ba_2CuO_{6+\delta}$ thin films*, Appl. Phys. Lett. **71**, p. 1706 (1997).

[19] Ginsberg D., *Physical Properties of High Temperature Superconductor II*, World Scientific (1990).

[20] Ruggiero S.T. and Rudman D.A., *Superconducting Devices*, Academic Press (1990).

[21] Kleiner R., Steinmeyer F., Kunkel G. and Müller P., *Intrinsic Josephson Effects in $Bi_2Sr_2CaCu_2O_8$ Single Crystals*, Phys. Rev. Lett. **68**, p. 2394 (1992).

[22] Obertelli S.D., Cooper J.R. and Tallon J.L., *Systematics in the thermoelectric power of high-T_c oxides*, Phys. Rev. B **46**, p. 14928 (1992).

[23] Ginsberg D., *Physical Properties of High Temperature Superconductor III*, World Scientific (1990).

[24] Pickett W.E., *Electronic structure of the high-temperature oxide superconductors*, Rev. Mod. Phys. **61**, p. 433 (1989).

[25] Madelung O., *Introduction to Solid State Theory*, Springer Verlag, Berlin (1978).

[26] Yu G., Lee C.H., Mihailovic D., Fincher C., Herron N., McCarron E.M. and Heeger A.J., *Electronic structure of insulating $YBa_2Cu_3O_{6+x}$: from Mott-Hubbard insulator to Fermi glass via oxygen doping*, J. Phys. Chem. Sol. **54**, p. 1161 (1993).

[27] Mott N.F. and Davis E.A., *Electronic Processes in Non-crystalline Materials*, Clarendon Press, Oxford (1979).

[28] Mott N., *Superconducting Ceramics - Is There an Explanation*, Nature **327**, p. 185 (1987).

[29] Mihailovic D., Foster C.M., Voss K.F., Mertelj T., Poberaj I. and Herron N., *Anomalous shifts of oxygen-mode frequencies in $La_{2-x}Sr_xCuO_4$, $YBa_2Cu_30_{7-\delta}$ and $Tl_2Ba_2Ca_{1-x}Gd_xCu_20_8$ studied by photoinduced infrared absorption and Raman spectroscopy* , Phys. Rev. B **44**, p. 237 (1991).

[30] Esteve D., Martinis J.M., Urbina C., Devoret M.H., Colin G., Munod P., Ribault M. and Revcolevschi A., *Observation of the AC Josephson effect inside copper-oxide-based superconductors*, Europhys. Lett. **3**, p. 1237 (1987).

[31] Gough C.E., Colclough M.S., Forgan E.M., Jordan R.M., Keene M., Muirhead C.M., Rae A.I.M., Thomas T., Abell J.S. and Sutton S., *Flux quantization in a high-T_c superconductor*, Nature **326**, p. 855 (1987).

[32] Barrett S.E., Durand D.J., Pennington C.H., Slichter C.P., Friedmann T.A., Rice J.P. and Ginsberg D.M., *^{63}Cu Knight shifts in the superconducting state of $YBa_2Cu_3O_{7-\delta}$ (T_c=90 K)*, Phys. Rev. B **41**, p. 6283 (1990).

[33] Alexandrov A.S. and Ranninger J., *Charged bose-liquid characteristics in high-T_c superconductors*, Sol. State Comm. **81**, p. 403 (1992).

[34] Thomsen C., *Light Scattering in High-T_c Superconductors,* in Cardona M. and Güntherodt G., *Light Scattering in Solids VI*, Springer-Verlag (1991).

[35] Warren W.W., Walstead R.E., Brennert J.F., Cava R.J., Tycko R., Bell R.F. and Dabbah G., *Cu spin dynamics and superconducting precursor effects in planes above T_c in $YBa_2Cu_3O_{6.7}$*, Phys. Rev. Lett. **62**, p. 1193 (1989).

[36] Tallon J.L., Cooper J.R., Desilva P.S.I.P.N., Williams G.V.M., Loram J.W., *Thermoelectric-Power - A Simple, Instructive Probe of High-T_c Superconductors*, Phys. Rev. Lett. **75**, p. 4114 (1995).

[37] Basov D.N., Timusk T., Dabrowski B. and Jorgensen J.D., *C-axis Response of $YBa_2Cu_4O_8$ - A Pseudogap and Possibility of Josephson Coupling of CuO_2 Planes*, Phys. Rev. B **50**, p. 3511 (1994).

[38] Loeser A.G., Shen Z.X., Dessau D.S., Marshall D.S., Park C.H., Fournier P. and Kapitulnik A., *Excitation gap in the normal state of underdoped $Bi_2Sr_2CaCu_2O_{8+\delta}$*, Science **273**, p. 325 (1996).

[39] Ding H., Yokoya T., Campuzano J.C., Takahashi T., Randeria M., Norman M.R., Mochiku T., Kadowaki K. and Giapintzakis J., *Spectroscopic evidence for a pseudogap in the normal state of underdoped high-T_c superconductors*, Nature **382**, p. 51 (1996).

[40] Nemetschek R., Opel M., Hoffmann C., Muller P.F., Hackl R., Berger H., Forro L., Erb A. and Walker E., *Pseudogap and superconducting gap in the electronic Raman spectra of underdoped cuprates*, Phys. Rev. Lett. **78**, p. 4837 (1997).

[41] Renner C., Revaz B., Genoud J.Y., Kadowaki K. and Fischer O., *Pseudogap precursor of the superconducting gap in under- and overdoped* $Bi_2Sr_2CaCu_2O_{8+\delta}$, Phys. Rev. Lett. **80**, p. 149 (1998).

[42] Kivelson S.A., Fradkin E. and Emery V.J., *Electronic liquid-crystal phases of a doped Mott insulator*, Nature **393**, p. 550 (1998).

[43] Lee P.A. and Wen X.G., *Unusual superconducting state of underdoped cuprates*, Phys. Rev. Lett **78**, p. 4111 (1997).

[44] Schmalian J., Pines D. and Stojkovic B., *Weak pseudogap behavior in the underdoped cuprate superconductors*, Phys. Rev. Lett. **80**, p. 3839 (1998).

[45] Campuzano J.C., Jennings G., Faiz M., Beaulaigue L., Veal B.W., Liu J.Z., Paulikas A.P., Vandervoort K., Claus H., List R.S., Arko A.J. and Bartlett R.J., *Fermi surfaces of* $YBa_2Cu_3O_{6.9}$ *as seen by angle-resolved photoemission*, Phys. Rev. Lett. **64**, p. 2308 (1990).

[46] King D.M., Shen Z.X., Dessau D.S., Wells B.O., Spicer W.E., Arko A.J., Marshall D.S., DiCarlo J., Loeser A.G., Park C.H., Ratner E.R., Peng J.L., Li Z.Y. and Greene R.L., *Fermi surface and electronic structure of* $Nd_{2-z}Ce_zCuO_{4-\delta}$, Phys. Rev. Lett. **70**, p. 3159 (1993).

[47] Batlogg B., Hwang H.Y., Takagi H., Cava R.J., Kao H.L. and Kwo J., *Normal State Phase Diagram of* $(La,Sr)_2CuO_4$ *from Charge and Spin Dynamics*, Physica C **235-240**, p. 130 (1994).

[48] Ding H., Campuzano J.C., Bellman A.F., Yokoya T., Norman M.R., Randeria M., Takahashi T., Katayama-Yoshida H., Mochiku T., Kadowaki K. and Jennings G., *Momentum Dependence of the Superconducting Gap in* $Bi_2Sr_2CaCu_2O_8$, Phys. Rev. Lett. **74**, p. 2784 (1995).

[49] Norman M.R., Randeria M., Ding H., Campuzano J.C. and Bellman A.F., *Polarization selection rules and superconducting gap anisotropy in* $Bi_2Sr_2CaCu_2O_8$, Phys. Rev. B **52**, p. 15107 (1995).

[50] Tsuei C.C. and Kirtley J.R., *Phase-sensitive tests of pairing symmetery in cuprate superconductors*, Physica C **282**, p. 4 (1997).

[51] Hardy W.N., Bonn D.A., Morgan D.C., Liang R. and Zhang K., *Precision measurments of the Temperature Dependence of λ in $YBa_2Cu_3O_{6.95}$: Strong evidence for nodes in the gap function*, Phys. Rev. Lett. **70**, p. 3999 (1993).

[52] Feenstra B.J., Schützmann J., van der Marel D., Pinaya R.P. and Decroux M., *Nonequilibrium Superconductivity and Quasiparticle Dynamics Studied by Photoinduced Activation of mm-Wave Absorption*, Phys. Rev. Lett. **79**, p. 4890 (1997).

[53] Kabanov V.V., Demsar J., Podobnik B. and Mihailovic D., *Quasiparticle relaxation dynamics in superconductors with different gap structures: theory and experiments on $YBa_2Cu_3O_{7-\delta}$*, Phys. Rev. B **59**, p. 1497 (1999).

[54] Chakravarty S., Sudbo A. Anderson P.W. and Strong S., *Interlayer Tunneling and Gap Anisotropy in High-Temperature Superconductors*, Science **261**, p. 337 (1993).

[55] Anderson P.W., *The Resonating Valence Bond State in La_2CuO_4 and Superconductivity*, Science **235**, p. 1196 (1987).

[56] Clarke D.G., Strong S.P. and Anderson P.W., *Incoherence of Single-Particle Hopping Between Luttinger Liquids*, Phys. Rev. Lett. **72**, p. 3218 (1994).

[57] Tamasaku K., Nakamura Y. and Uchida S., *Charge Dynamics Across the CuO_2 Planes in $La_{2-x}Sr_xCuO_4$*, Phys. Rev. Lett. **69**, p. 1455 (1992).

[58] Schützmann J., Somal H.S., Tsvetkov A.A., vanderMarel D., Koops G.E.J., Koleshnikov N., Ren Z.F., Wang J.H., Bruck E. and Menovsky A.A., *Experimental test of the interlayer pairing models for high-T_c superconductivity using grazing-incidence infrared reflectometry*, Phys. Rev. B **55**, p. 11118 (1997).

[59] Mook H.A., Dai P.C., Dogan F. and Hunt R.D., *One-dimensional nature of the magnetic fluctuations in $YBa_2Cu_3O_{6.6}$*, Nature **404**, p. 729 (2000).

[60] Sharma R.P., Ogale S.B., Zhang Z.H., Liu J.R., Chu W.K., Veal B., Paulikas A., Zheng H. and Venkatesan T., *Phase transitions in the incoherent lattice fluctuations in* $YBa_2Cu_3O_{7-\delta}$, Nature **404**, p. 736 (2000).

[61] Bianconi A., Saini N.L., Lanzara A., Missori M., Rosseti R.T., Oyanagi H., Yamaguchi H., Oka K. and Ito T., *Determination of the local lattice distortions in the* CuO_2 *plane of* $La_{1.85}Sr_{0.15}CuO_4$, Phys. Rev. Lett. **76**, p. 3412 (1996).

[62] Egami T. and Billinge S., *Lattice Effects in High-*T_c *Superconductors* in *Physical Properties of High Temperature Superconductors VI*, Ginsberg D., p. 265, World Scientific (1996).

[63] Tranquada J., Sternlieb B.J., Axe J.D., Nakamura Y. and Uchida S., *Evidence for stripe correlations of spins and holes in copper oxide superconductors*, Nature **375**, p. 561 (1995).

[64] Scalapino D.J., *Significance of* $d_{x^2-y^2}$ *Pairing in the Cuprates*, Science **266**, p. 1626 (1994).

[65] Bulut N. and Scalapino D.J., *Analysis of NMR Data in the Superconducting State of* $YBa_2Cu_3O_7$, Phys. Rev. Lett. **68**, p. 706 (1992).

[66] Hirschfeld P.J., Quinlan S.M. and Scalapino D.J., *c-axis infrared conductivity of a* $d_{x^2-y^2}$*-wave superconductor with impurity and spin-fluctuation scattering*, Phys. Rev. B **55**, p. 12742 (1997).

[67] Millis A.J., Monien H. and Pines D., *Phenomenological model of nuclear relaxation in the normal state of* $YBa_2Cu_3O_7$, Phys. Rev. B **42**, p. 167 (1990).

[68] Holcomb M.J., Perry C.L., Collman J.P. and Little W.A., *Thermal Difference Reflectance Spectroscopy of the High Temperature Cuprate Superconductors*, Phys. Rev. B **53**, p. 6734 (1996).

[69] Corson J., Mallozzi R., Orenstein J., Eckstein J.N. and Bozovic I., *Vanishing of phase coherence in underdoped* $Bi_2Sr_2CaCu_2O_{8+\delta}$, Nature **398**, p. 221 (1999).

[70] Berezinskii V.L., *Destruction of long-range order in one-dimensional and two-dimensional systems having a continuous symmetry group I. Classical systems*, Sov. Phys. JETP **32**, p. 493 (1970).

[71] Kosterlitz J.M. and Thouless D.J., *Ordering, metastastability and phase transitions in two-dimensional systems*, J. Phys. C **6**, p. 1181 (1973).

[72] Gofron K., Campuzano J.C., Abrikosov A.A., Lindroos M., Bansil A., Ding H., Koelling D. and Dabrowski B., *Observation of an "Extended" Van Hove Singularity in $YBa_2Cu_4O_8$ by Ultrahigh Energy Resolution Angle-Resolved Photoemission*, Phys. Rev. Lett **73**, p. 3302 (1994).

[73] Mattheiss L.F. and Hamann D.R., *Electronic Band Properties of $CaSr_2Bi_2Cu_2O_8$*, Phys. Rev. B **39**, p. 5012 (1988).

[74] Aspnes D.E. and Kelly M.K., *Optical Properties of High-T_c Superconductors*, IEEE J. of Quant. Elec. **25**, p. 2378 (1989).

[75] Heyen E.T., Kircher J. and Cardona M., *Resonant Raman scattering in insulating $YBa_2Cu_3O_6$ as a probe of its electronic structure*, Phys. Rev. B **45**, p. 3037 (1992).

[76] Zibold A., Widder L., Geserich H.P., Brauchle G., Claus H., Vonlohneysen H., Nucker N., Erb A. and Mullervogt G., *Optical Investigation of the Metal-Insulator-Transition Regime in Single-Domain Crystals of $YBa_2Cu_3O_x$*, Physica C **212**, p. 365-371 (1993).

[77] Klingshirn C.F., *Semiconductor Optics*, Springler (1997).

[78] Svelto O., *Principles of Lasers*, Plenum (1989).

[79] Stevens C.J., *Time-Resolved Spectroscopy of Excitons in II-VI Heterostructures*, D.Phil Thesis, University of Oxford (1994).

[80] Agrawal G.P. and Boyd R., *Contemporary Nonlinear Optics*, Academic Press (1992).

[81] Duarte F.J., *Tunable Lasers Handbook, Optics and Photonics*. Academic Press (1995).

[82] Brabec T., Spielmann C., Curley P.F and Krausz F., *Kerr Lens mode locking*. Optics Lett. **17**, p. 1292 (1992).

[83] Stingl A., Lenzner M., Spielmann C. and Krausz F., *Sub-10-fs mirror-dispersion-controlled Ti:sapphire laser*, Opt. Lett. **20**, p. 603 (1995).

[84] Diels J.C.M., Fontaine J.J., McMichael I.C. and Simoni F., *Control and measurement of ultrashort pulse shapes (in amplitude and phase) with femtosecond accuracy*, Appl. Optics **24**, p. 1270 (1985).

[85] Bdikin I.K., Mashtakov A.D., Mozhaev P.B. and Ovsyannikov G.A., *Orientation relations and twinning in heterostructures* $YBa_2Cu_3O_x//NdGaO_3$ *and* $YBa_2Cu_3O_x//CeO_2//Al_2O_3$, Physica C **334**, p. 168 (2000).

[86] Chen W.M., Yao X.X., Guo Y.C., Liu H.K. and Dou S.X., *A model of twin domains in* $YBa_2(Cu_{1-x}Co_x)_3O_y$, J. of Super. **13**, p. 129 (2000).

[87] Voronkova V.I. and Wolf T., *Thermomechanical Detwinning of* $YBa_2Cu_3O_{7-x}$ *Single-Crystals under Reduced Oxygen Partial-Pressure*, Physica C **218**, p. 175 (1993).

[88] Allen P.B., *Theory of Thermal Relaxation of Electrons in Metals*, Phys. Rev. Lett. **59**, p. 1460 (1987).

[89] Eesley G.L., *Observation of non-equilibrium heating in copper*, Phys. Rev. Lett. **51**, p. 2140 (1983).

[90] Schoenlein R.W., Lin W.Z., Fujimoto J.G. and Eesley G.L., *Femtosecond studies of nonequilibrium electronic processes in metals*, Phys. Rev. Lett. **58**, p. 1680 (1987).

[91] Brorson S.D., Fujimoto J.G. and Ippen E.P., *Femtosecond electronic heat-transport dynamics in thin gold films*, Phys. Rev Lett. **59**, p. 1962 (1987).

[92] Allen P.B., *Empirical electron-phonon λ values from resistivity of cubic metallic elements*, Phys. Rev. B **36**, p. 2920 (1987).

[93] Allen P.B., *Neutron spectroscopy of superconductors*, Phys. Rev. B **6**, p. 2577 (1972).

[94] Brorson S.D., Kazeroonian A., Moodera J.S., Face D.W., Cheng T.K., Ippen E.P., Dresselhaus M.S. and Dresselhaus G., *Femtosecond room-temperature measurement of the electron-phonon coupling constant gamma in metallic superconductors*, Phys. Rev. Lett. **64**, p. 2172 (1990).

[95] Brorson S.D., *Femtosecond Thermomodulation Measurements of Transport and Relaxation in Metals and Superconductors*, Thesis, Research Laboratory of Electronics, Massachusetts Institute of Technology, Cambridge, USA (1990).

[96] Brorson S.D., Kazeroonian A., Face D.W., Cheng T.K., Doll G.L., Dresselhaus M.S., Dresselhaus G., Ippen E.P., Venkatesan T., Wu X.D. and Inam A., *Femtosecond Thermomodulation Study of High-T_c Superconductors*, Solid State Comm. **74**, p. 1305-1308 (1990).

[97] Chwalek J.M., Uher C., Whitaker J.F., Morou G.A., Agostinelli J. and Lelental M., *Femtosecond optical absorption studies of nonequilibrium processes in high T_c superconductors,* Appl. Phys. Lett. **57**, p. 1696-1698 (1990).

[98] Han S.G., Vardeny Z.V., Wong K.S., Symko O.G. and Koren G., *Femtosecond Optical Detection of Quasiparticle Dynamics in High-T_c $YBa_2Cu_3O_{7-\delta}$ Superconducting Thin Films*, Phys. Rev. Lett. **65**, p. 2708-2711 (1990).

[99] Muhlschlegel B., Z. Phys. **155**, p. 313 (1959).

[100] Eesley G.L., *Generation of nonequilibrium electron and lattice temperatures in copper by picosecond laser pulses*, Phys. Rev. B **33**, p. 2144 (1986).

[101] Rothwarf A. and Taylor B.N., *Measurement of Recombination Lifetimes in Superconductors*, Phys. Rev. Lett. **19**, p. 27-30 (1967).

[102] Bechtel J.H., *Heating of solid targets with laser pulses*, J. Appl. Phys. **46**, p. 1585 (1975).

[103] Kazeroonian A.S., Cheng T.K., Brorson S.D., Li Q., Ippen E.P.. Wu X.D.. Venkatesan T., Etemad S., Dresselhaus M.S. and Dresselhaus G., *Probing the Fermi level of* $Y_{1-x}Pr_xBa_2Cu_3O_{7-\delta}$ *by femtosecond spectroscopy*, Solid State Comm. **78**, p. 95-98 (1991).

[104] Zhou Z., Ye J., Oka K. and Nishihara Y., *Superconducting* $PrBa_2Cu_3O_x$, Phys. Rev. Lett. **80**, p. 1074-1077 (1998).

[105] Reitze D.H., Wiener A.M., Inam A. and Etemad S., *Fermi-level dependence of femtosecond response in non-equilibrium high-*T_c *superconductors*, Phys. Rev. B **46**, p. 14309-14312 (1992).

[106] Chekalin S.V., Farztdinov V.M., Golovlyov V.V., Letokhov V.S., Lozovik Y.E., Matveets Y.A. and Stepanov A.G., *Femtosecond Spectroscopy of* $YBa_2Cu_3O_{7-\delta}$*: Electron-Phonon-Interaction Measurement and Energy-Gap Observation*, Phys. Rev. Lett. **67**, p. 3860 (1991).

[107] Lozovik Y.E., Dobryaknov A.L., Ernsting N.P. and Kovalenko S.A., *New Method of non-Fermi liquid study by pump-supercontinuum probe femtosecond spectroscopy*, Phys. Lett. A **223**, p. 303-307 (1996).

[108] Hegmann F.A. and Preston J.S., *Origin of the fast photoresponse of epitaxial* $YBa_2Cu_3O_{7-\delta}$ *thin films*, Phys. Rev. B **48**, p. 16023 (1993).

[109] Williams C., Adam R., Xie Q., Sobolewski R. and Harnack O., *Nonequilibrium kinetic inductive response of Y-Ba-Cu-O photodetectors*, Supercond. Sci. Tech. **12**, p. 843-846 (1999).

[110] Han S.G., Vardeney Z.V., Symko O.G. and Koren G., *Quasiparticle Relaxation in a High-*T_c *Superconductor*, Phys. Rev. Lett. **67**, p. 1053 (1991) and Eesley G.L., Heremans J., Meyer M.S. and Doll G.L., *Reply to Quasiparticle Relaxation in a High-*T_c *Superconductor*, Phys. Rev. Lett. **67**, p. 1053 (1991).

[111] Eesley G.L., Heremans J., Meyer M.S., Doll G.L. and Liou S.H., *Reply to Quasiparticle Relaxation in a High-*T_c *Superconductor*, Phys. Rev. Lett. **67**, p. 1054 (1991).

[112] Chwalek J.M., Uher C., Whitaker J.F., Morou G.A. and Agostinelli J.. *Sub-picosecond time-resolved studies of coherent phonon oscillations in thin-film* $YBa_2Cu_3O_{6+x}$, Appl. Phys. Lett. **58**, p. 980 (1991).

[113] Albrecht W., Kruse T. and Kurz H., *Time-Resolved Observation of Coherent Phonons in Superconducting* $YBa_2Cu_3O_{7-\delta}$, Phys. Rev. Lett. **69**, p. 1451 (1992).

[114] Zeiger H.J., Vidal J., Cheng T.K., Ippen E.P., Dresselhaus G. and Dresselhaus M.S., *Theory for displacive excitation of coherent phonons*, Phys. Rev. B **45**, p. 768 (1992).

[115] Cheng T.K., Vidal J., Zeiger H.J., Dresselhaus G., Dresselhaus M.S. and Ippen E.P., *Mechanism for displacive excitation of coherent phonons in Sb, Bi, Te, and* Ti_2O_3, Appl. Phys. Lett. **59**, p. 1923 (1991).

[116] Stevens C.J., Smith D., Chen C., Ryan J.F., Podobnik B., Mihailovic D., Wagner G.A. and Evetts J.E., *Evidence for Two-Component High-Temperature Superconductivity in the Femtosecond Optical Response of* $YBa_2Cu_3O_{7-\delta}$, Phys. Rev. Lett. **78**, p. 2212-2215 (1997).

[117] Kabanov V.V., Demsar J. and Mihailovic D., *Carrier-relaxation dynamics in intra-gap states: The case of the superconductor* $YBa_2Cu_3O_{7-\delta}$ *and the charge-density-wave semiconductor* $K_{0.3}MoO_3$, Phys. Rev. B **61**, p. 1477 (2000).

[118] Smith D.C., *Measurements of Ultrafast Dynamics in a Superconductor* $YBa_2Cu_3O_{7-\delta}$, *and a Semiconductor, GaSb*, D.Phil Thesis, University of Oxford (1998).

[119] Schnelle W., Braun E., Broicher H., Dömel R., Braunisch W., Harnischmacher J. and Wohlleben D., *Fluctuation Specific Heat and Thermal Expansion of YBaCuO and DyBaCuO*, Physica C **168**, p. 465-474 (1990).

[120] Mihailovic D., Podobnik B., Demsar J., Wagner G. and Evetts J., *Divergence of the quasiparticle lifetime with doping and evidence for pre-formed pairs below* T^* *in* $YBa_2Cu_3O_{7-\delta}$ *direct measurements by femtosecond time-resolved spectroscopy.* J. Phys. Chem. Solids **59**, p. 1937 (1998).

[121] Albrecht W., Kruse T., Leo K. and Kurz H., *Dynamics of Optimally Excited Quasi-particles in $YBa_2Cu_3O_x$*, Appl. Phys. A **57**, p. 203 (1993).

[122] Mihailovic D., Stevens C.J., Podobnik B., Demsar J., Zavrtanik M., Smith D. and Ryan J.F., *Evidence for Two-component Superconductivity in the Femtosecond Optical and Transient Photoconducting Response of $YBa_2Cu_3O_{7-\delta}$*, Physica C **282-287**, p. 186 (1997).

[123] Hoffmann A., Schuller I.K., Ren Z.F., Lao J.Y. and Wang J.H., *Persistent photoconductivity in overdoped high-T_c thin films,* Phys. Rev. B **56**, p. 13742 (1997).

[124] Loram J.W., Mirza K.A., Cooper J.R. and Liang W.Y., *Electronic Specific Heat of $YBa_2Cu_2O_{6+x}$ from 1.8 to 300K*, Phys. Rev. Lett. **71**, p. 1740 (1993).

[125] Ishida K., Yoshida K., Mito T., Tokunaga Y., Kitaoka Y., Asayama K., Nakayama Y., Shimoyama J. and Kishio K., *Pseudogap behavior in single-crystal $Bi_2Sr_2CaCu_2O_{8+\delta}$ probed by Cu NMR*, Phys. Rev. B **58**, p. R5960 (1998).

[126] Oda K., Hoya K., Kubota R., Manabe C., Momono N., Nakano T. and Ido M., *Strong pairing interactions in the underdoped region of $Bi_2Sr_2CaCu_2O_{8+\delta}$*, Physica C **281**, p. 135 (1997).

[127] Broun D.M., Morgan D.C., Ormeno R.J., Lee S.F., Tyler A.W., Mackenzie A.P. and Waldram J.R., *In-plane microwave conductivity of the single-layer cuprate $Tl_2Ba_2CuO_{6+\delta}$*, Phys. Rev. B **56**, p. R11443 (1997).

[128] Waldmann O., Steinmeyer F., Muller P., Neumeier J.J., Regi F.X., Savary H. and Schneck J., *Temperature and doping dependence of the penetration depth in $Bi_2Sr_2CaCu_2O_{8+\delta}$*, Phys. Rev. B **53**, p. 11825 (1996).

[129] Eelsey G.L., Heremans J., Meyer M.S. and Doll G.L., *Quasi-particle Relaxation in a High-T_c Superconductor - Reply*, Phys. Rev. Lett. **67**, p. 1054 (1991).

[130] Elsayed-Ali H.E., Norris T.B., Pessot M.A. and Mourou G.A., *Time-Resolved Observation of Electron-Phonon Relaxation in Copper*, Phys. Rev. Lett. **58**, p. 1212 (1987).

[131] Gonnelli R.S., Ummarino G.A. and Stepanov V.A., *Reproducible tunneling determination of the electron-phonon spectral function in optimally-doped Bi-2212 single-crystal break junctions*, J. Phys. Chem. of Solids **59**, p. 2058 (1998).

[132] Ryan J.F., Taylor R.A., Turberfield A.J., Maciel A., Worlock J.M., Gossard A.C. and Wiegmann W., *Time-Resolved Photoluminescence of Two-Dimentional Hot Carriers in GaAs-AlGaAs Heterostructures*, Phys. Rev. Lett. **53**, p. 1841 (1984).

[133] Stevenson R.W.H., *Phonons in perfect lattices and in lattices with point imperfections*, Oliver & Boyd (1966).

[134] Ioffe L.B. and Millis A.J., *Resistance of Josephson-junction arrays at low temperatures*, Phys. Rev. B **58**, p. 11631 (1998).

[135] Demsar J., Hudej R., Karpinski J., Kabanov V.V. and Mihailovic D., *Quasiparticle dynamics and gap structure in $Hg_1Ba_2Ca_2Cu_3O_{8+\delta}$ investigated with femtosecond spectroscopy*, submitted to Phys. Rev. B, May (2000).

[136] Lozovik Y.E. and Poushnov A.V., *Manifestation of superconducting gap symmetry in the optical spectrum*, Phys. Lett. A **194**, p. 405-412 (1994).

[137] Puchkov A.V., Fournier P., Basov D.N., Timusk T., Kapitulnik A. and Kolesnikov N.N., *Evolution of the pseudogap state of high-T_c superconductors with doping*, Phys. Rev. Lett. **77**, p. 3212 (1996).

[138] Bourges P., Sidis Y., Regnault L.P., Hennion B., Villeneuve R., Collin G., Vettier C., Henry J.Y. and Marucco J.F., *Comparison of antiferromagnetic fluctuations in zinc-free and zinc-doped YBCO in fully oxidized samples. Studies by inelastic neutron scattering*, J. Phys. Chem. Solids **56**, p. 1937 (1995).

[139] Nessler W., Ogawa S., Nagano H., Petek H., Shimoyama J., Nakayama Y. and Kishio K., *Femtosecond time-resolved study of the energy and temperature dependence of hot-electron lifetimes in $Bi_2Sr_2CaCu_2O_{8+\delta}$*, Phys. Rev. Lett **81**, p. 4480 (1998).

[140] Carbotte J.P., Schachinger E. and Basov D.N., *Coupling strength of charge carriers to spin fluctuations in high-temperature superconductors*, Nature **401**, p. 354 (1999).